Spring 1-1-2015

Lidar Observations and Modeling Studies of Antarctic Temperature Tides at McMurdo & Establishment of Temperature Climatology with Calibrated Fe Boltzmann and Na Doppler Lidars

Weichun Fong
University of Colorado at Boulder, weichun.fong@colorado.edu

LIDAR OBSERVATIONS AND MODELING STUDIES OF ANTARCTIC TEMPERATURE TIDES AT MCMURDO

&

ESTABLISHMENT OF TEMPERATURE CLIMATOLOGY WITH CALIBRATED FE BOLTZMANN AND NA DOPPLER LIDARS

by

WEICHUN FONG
B.Sc., National Taiwan University, 2007

A thesis submitted to the

Faculty of the Graduate School of the
University of Colorado in partial fulfillment
of the requirement for the degree of
Doctor of Philosophy
Department of Aerospace Engineering Sciences
2015

This thesis entitled:

LIDAR OBSERVATIONS AND MODELING STUDIES OF
ANTARCTIC TEMPERATURE TIDES AT MCMURDO
&
ESTABLISHMENT OF TEMPERATURE CLIMATOLOGY WITH
CALIBRATED FE BOLTZMANN AND NA DOPPLER LIDARS

written by Weichun Fong
has been approved for the Department of Aerospace Engineering Sciences

_____
Dr. Xinzhao Chu (Chair)

_____
Dr. Timothy Fuller-Rowell

_____
Dr. Anne Smith

Date: _____

The final copy of this thesis has been examined by the signatories, and we find that both the content and the form meet acceptable presentation standards of scholarly work in the above mentioned discipline.

Fong, Weichun (Ph.D., Aerospace Engineering Sciences)

Lidar Observations and Modeling Studies of Antarctic Temperature Tides at McMurdo & Establishment of Temperature Climatology with Calibrated Fe Boltzmann and Na Doppler Lidars

Thesis directed by Professor Xinzhao Chu

Abstract

McMurdo lidar campaign provides invaluable data for studies of the polar middle and upper atmosphere. The science topics to be addressed in this dissertation are the temperature tides (30–110 km) and temperature climatology (0–110 km). Tides are important to the dynamic and chemical processes in the middle and upper atmosphere. Tides, for examples, can obtain large amplitudes in the middle and upper atmosphere, where they modulate ionospheric variability via the E-region dynamo effect, enhance vertical atmosphere coupling and cause instabilities by inducing significant temperature gradients and wind shears. However, observations of tides in the Antarctic region are rare, especially for temperature tides. In this dissertation, we present lidar measurements of winter tides from 30 to 110 km at McMurdo (77.8°S, 166.7°E). The observed diurnal and semidiurnal tides indicate small amplitudes (less than 3 K) below 100 km, but above 100 km, we observed fast growth of tidal amplitudes to at least 15 K near 110 km, exceeding that of the freely propagating tides originating from the lower atmosphere. Such fast growth of tidal amplitude raises questions regarding the identification of sources of the tides above 100 km and how these sources are related to geomagnetic activities or other factors.

We utilized the Coupled Thermosphere Ionosphere Plasmasphere Electrodynamics (CTIPe) model to further investigate the questions raised. Simulations with the CTIPe model

reproduce the lidar observations and exhibit a concentric ring structures of diurnal amplitudes encircling the south geomagnetic pole and overlapping the auroral zone. These findings point to a magnetospheric source origin. Mechanistic studies using CTIPe show that the adiabatic cooling/heating associated with Hall ion drag is the dominant source of this feature, while Joule heating is a minor contributor due to the counteraction by Joule-heating-induced adiabatic cooling. The sum of total dynamical effects and Joule heating explains ~80% of the diurnal amplitudes. The auroral particle heating, lower atmosphere tides, and direct solar heating have minor contributions, according to the CTIPe model.

In the polar region, temperature controls numerous geophysical phenomena and is also a key variable in climate change studies. We derived the temperature climatology from the ground to 110 km at McMurdo based on the 4 years of lidar and radiosonde observations, and applied the backward differtiation method to fill in the data gaps. The climatology is compared with model outputs and satellite measurements. The latitudinal dependences of stratopause and mesopause temperature were found between different Antarctica stations. The McMurdo lidar campaign also demonstrated the potential to push the temperature climatology lid altitude to 120 km during winter, where measurements are extremely rare.

Finally, we utilize the forward model method to assess how PMT non-linear response and laser pulse spectrum affect the temperature and radial wind measurements of a 3-frequency Na Doppler lidar. As the polar region from 100 to 200 km is the least understood and most sparsely observed region, the tidal study presented here will help improve the current understanding of how the wave coupling between the ionosphere plasma and the neutral thermosphere. Also, the establishments of the temperature climatology and temperature calibration not only reveal the thermal structure at McMurdo, but also provide references for the future studies. The calibrated

temperature data will serve as the baseline for comparison with measurements made decades in the future, and the calibration methods we developed will be a guideline for the lidar field.

Dedication

This thesis is dedicated to my beloved parents and sister.

Acknowledgments

I sincerely appreciate my advisor Dr. Xinzhao Chu for providing the opportunity for me to enter the lidar field for my PhD study, and also a trip to Antarctica, of which I never would have thought about when I first came to Boulder, and of course the guidance she gave on both science studies and lidar technology. I wish to sincerely acknowledge the valuable discussions and comments from my committee Drs. Jeff Forbes, Tim Fuller-Rowell, Chester Gardner, Hanli Liu, Peter Pilewskie, and Anne Smith. I also want to acknowledge Drs. Art Richmond, Wenbin Wang, Mihail Codrescu, and Elsayed Talaat for the valuable discussions and suggestions on the tidal studies and the CTIPe model. Last but not least, I would like to acknowledge those valuable discussions and supports from my colleagues Wentao Huang, Xian Lu, Zhangjun Wang, John Smith, Zhibin Yu, Cao Chen, Jian Zhao, Cyrus Abari, Brendan Roberts, Ian Barry, and Bo Tan. This dissertation is supported by the NSF grants ANT-0839091, PLR-1246405, and AGS-1136272.

CONTENTS

List of Figures

List of Tables

CHAPTER 1

Introduction

Climate change and the space-atmosphere interaction are two of the highest priority objectives for the atmosphere and space sciences in the 21st century. This dissertation is motivated by the compelling needs of advancing our understanding of Earth's climate, neutral atmosphere and space-atmosphere interaction. Human-induced changes in the Earth climate system are one of the most challenging issues in this century. In the meantime, the atmosphere-ionosphere-magnetosphere (AIM) system is a complex and active element of space weather, and also a region of geospace where exploration of its fundamental processes helps reveal universal physical processes through our galaxy [*CEDAR: The New Dimension*, 2011; *NRC 2013-2022 Decadal Strategy for Solar and Space Physics*, 2013].

Firstly, human beings have been trying numerous approaches to monitor and investigate the impacts that have been made or will occur in the future to our environment from climate change since the last century. For example, increasing concentrations of greenhouse gases such as CO_2 and CH_4 have begun to show environmental impacts [*IPCC report*, 2001, 2007; *ACIA*, 2004]. There is also observational evidence of global long-term stratospheric cooling of annual mean temperatures of ~0.5℃ per decade between 1979 and 2007 from satellite and radiosonde data [*Randel et al.*, 2009]. Besides observations, numerous models have also been built up to assess the global climate change and its impacts in the near and far future [e.g., *Taylor et al.*, 2012]. Nevertheless, it is still essential to keep establishing the long-term, stable, and well-calibrated observations across a spectrum of human and environmental systems for diagnosing and understanding climate change and its impacts [*Matson et al.*, 2010].

Secondly, the space-atmosphere interaction region (SAIR) is a highly dynamic and complex system. All the interactions between the neutral particles and plasma happen here, under the presence of the magnetic field, electric field, and the momentum and energy deposition from both the magnetosphere and the lower atmosphere [*NRC 2013-2022 Decadal Strategy for Solar and Space Physics*, 2013]. The SAIR is known to be essential for sustaining life on Earth by absorbing and attenuating the harmful solar radiation. The extreme ultraviolet (EUV) radiation is significantly damped in the thermosphere through the reaction with oxygen and atomic oxygen, and the ultraviolet (UV) radiation is mainly absorbed by the ozone layer in the stratosphere. The SAIR of Earth also plays an essential role of regulating gaseous escape, ablating meteoric materials, dissipating energetic particles and fields from space to protect all living things on Earth. In addition, waves from the lower atmosphere usually deposit momentum and energy in SAIR through dissipation and other dynamical processes. However, SAIR is still one of the least understood regions of the Earth atmosphere, especially in the polar areas.

From above, to advance the understanding of the climate change and explore the SAIR, the measurements of the neutral atmosphere is crucial. To help address these issues, the Chu lidar group from the University of Colorado has deployed an Fe Boltzmann temperature lidar system at McMurdo, Antarctica since 2010 to make long-term observations of polar atmosphere from 30 to over 110 km. This McMurdo lidar campaign provides invaluable temperature measurements for studying climate change and SAIR. At the same time, the lidar group also made an efforts to calibrate the lidar measurements via assessing the system uncertainties and their physical causes by any possible methods in order to establish not only the trustable and stable baseline for the measurements decades from now on but also to provide a guidelines for the lidar field.

1.1 Temperature Measurements in the Polar Regions

Atmospheric temperature is one of the indicators for researchers to monitor climate change and is also one of the fundamental parameters for atmospheric science studies. Many phenomena, such as polar mesospheric cloud (PMC), polar stratospheric cloud (PSC), and chemical reactions in the mesosphere and lower thermosphere (MLT) region, are dominated by temperature [e.g., *DeLand et al.*, 2006; *Lowe and MacKenzie, 2008*; *Plane*, 2003]. Studies have shown that the polar region of the middle and upper atmosphere is more sensitive to global climate change than other latitude regions [*IPCC report*, 2001; *Turner et al.*, 2013], thus it makes middle and upper atmosphere temperature measurements at polar region crucial and an excellent candidate to monitor climate change.

Model studies have shown that increasing CO_2 concentration in the atmosphere might result in cooling of the temperature at both stratopause and mesopause by several K [e.g., *Roble and Dickinson*, 1989; *Akmaev and Fomichev*, 2000; *Portmann et al.*, 2005]. Also, some long-term observation results have shown the sign of a negative temperature trends in the middle and upper atmosphere during the last few decades [e.g., *Aikin et al.*, 1991; *Angell*, 1991; *Golitsyn et al.*, 1996], though more data are needed to verify that the claim that observed negative temperature trends are resulted from anthropogenic activity. It is noteworthy as well that some results claim no discernable trend in the summer polar mesosphere [e.g., *Lubken*, 2000, 2001]. Furthermore, PMC, a unique phenomenon at high-latitude summer mesopause region, has been shown to have a trend of increasing brightness and occurrence due to the long-term change of mesospheric temperature (and also water vapor) [*Thomas*, 1996a,b]; this is an additional indicator of global climate change other to that provided by direct temperature measurements.

The temperature structure of the middle and upper atmosphere in the polar region is an interesting topic in our atmosphere. This is not only because in this region there are

large-amplitude dynamical variations associated with tides, planetary waves, and gravity waves, but also because some characteristics of atmosphere constituents and chemical processes are different than those at the low- and mid-latitude regions. For example, during polar winter night, without direct sunlit, the stratopause would not exist if it were due only to solar radiation. Measurements have shown that the real stratopause is at about the same altitude as in the sunlit region, which indicates that dynamical processes are necessary for the explanation [e.g., *Hitchman et al.*, 1989; *Kanzawa*, 1989]. Furthermore, polar region is the location of aurora activity, such that, for example, NO concentration is enhanced through auroral processes during geomagnetic storms, and can be transported downward from the thermosphere to the stratosphere and then react with ozone [*Solomon et al.*, 1982; *Siskind et al.*, 1989]. These two examples reflect the crucial roles that dynamical and chemical processes can play when we are trying to study the temperature structures at the polar region.

Today, methods for temperature profiling in the middle and upper atmosphere at polar region are diverse. There are rocket temperature soundings, rocketborne mass spectrometer, falling sphere, satellite observations, ground-based lidars, all-sky imagers, and interferometers. The first two methods are based on in-situ measurement results of temperature or air density profiles from which temperature profile can be calculated by seeding the upper boundary temperature. For examples, *Golitsyn et al*. [1996] used rocket soundings temperature data at Heiss Island (80.6°N) and Molodezhnaya (67.7°S) to study the long-term trend in the middle and upper atmosphere from 1970s to 1990s. They showed a cooling of 1–3 K/decade between 30 and 70 km. *Lübken and von Zahn* [1991] utilized temperature profiles derived from both rocketborne mass spectrometer and falling sphere measurements from 60 to 110 km in 1980s to investigate the annual variation of polar MLT region thermal structure near Andenes, Norway (69.2°N). The main merits of the in situ measuring rocket techniques are that they are cost-effective and can be

completed within relative short time frame, compared with satellite missions, therefore these techniques are still used for studying the middle and upper atmosphere.

Nowadays, the remaining temperature profiling methods, satellite observations, ground-based lidars, all-sky imagers, and interferometers, are probably the most common methods that one can find when looking for temperature measurements in the middle and upper atmosphere in polar regions. Satellite observations, such as SABER, the Sounding of the Atmosphere using Broadband Emission Radiometry experiment on the Thermosphere Ionosphere Mesosphere Energetics and Dynamics (TIMED) satellite launched in 2001 [*Russell et al.*, 1999], and MLS, the Microwave Limb Sounder on the EOS (Earth Observing System) Aura satellite launched in 2004, are two of the well-known satellite instruments that provide global temperature measurements. SABER kinetic temperature is retrieved from CO_2 15 μm limb emission during nighttime and both CO_2 15 μm and CO_2 4.3 μm during daytime [e.g., *Mertens et al.*, 2004]. MLS measures temperature primarily from the thermal emission of oxygen [*Day et al.*, 2011]. Ground-based lidars, such as Rayleigh lidar and resonance fluorescence lidar, are widely used for temperature profiling in the polar region. We will give detailed introduction in Section 3 of this chapter. Ground-based all-sky imagers and interferometers, typically utilize the airglow in the MLT region, such as the emission from OH, O_2(0,1) band, Na doublet, and atomic OI, to derive temperature (and wind for Fabry-Perot interferometer) [e.g., *Hernandez et al.*, 1993; *Azeem and Sivjee*, 2009; *Nielson et al.*, 2006].

In a general sense, we know that the temperature measurements at the polar middle and upper atmosphere help researchers to monitor climate change. However, in comparison with the existing temperature data and published papers for the low- and mid- latitude regions, long-term, year-round, and range-resolved temperature measurements at high-southern latitudes are rare. Ground-based passive remote sensing instruments, such as temperature mapper, Michelson

interferometers, and Fabry-Perot interferometers, usually are limited to solar background and have to operate during nighttime. Moreover, the lack of vertical range-resolving ability also prevents users from investigating the vertical structure of the atmosphere. Satellite measurements, such as SABER and MLS, are free from the limits that ground-based passive instruments have, and can provide year-round measurements and usually have wide coverage in longitude and latitude. However, the temporal and spatial resolutions of the satellite data are usually poor, and limit data users from studying high frequency features. Some satellites do not have coverage at high-latitude regions due to their orbital geometries.

In contrast to ground-based passive instruments and space-based instruments, ground-based lidar can provide range-resolved, high-resolution, long-term, and year-round temperature measurements with full-diurnal coverage at polar regions. Due to the remote and harsh environment, it is challenging to deploy a complicated system to Antarctica, such as resonance fluorescence lidar. However, a successful deployment of an Fe Boltzmann lidar system to McMurdo station (77.8°S) in 2010 started the unprecedented McMurdo lidar campaign. Not only does it fill in the lidar temperature measurement gap in latitudes between South Pole (90°S) and Rothera (67.5°S) stations, but the ability of measuring temperature up to 170 km also opens new views for our understanding about the polar region middle and upper atmosphere [*Chu et al.*, 2011b; *Yu and Chu*, 2015].

1.2 Tidal Study in Antarctica

Atmospheric tides are global-scale periodic forced oscillations of the atmosphere, for which the periods are harmonics of a solar day. Tides can be further divided into two categories, migrating (Sun-synchronous) and nonmigrating (non-Sun-synchronous) tides according to their

horizontal phase velocities. In the low-latitude region, the migrating tides tend to dominate, with the largest diurnal tide perturbations in the horizontal wind fields. In the mid-latitude region, the migrating semidiurnal tide is the largest in horizontal wind fields. The driving forces of migrating and nonmigrating tides are various. Migrating tides are mainly driven by periodic absorption of solar radiation in the atmosphere, and nonmigrating tides can be driven by latent heat release in the tropical region [*Hagan and Forbes*, 2002; *Zhang et al.*, 2010a,b] and by nonlinear interactions between stationary planetary waves and the dominant migrating tides [*Angelats i Coll and Forbes*, 2002; *Hagan and Roble*, 2001; *Murphy et al.*, 2009].

The systematic tidal study can be traced back to the tidal theory developed by *Chapman and Lindzen* [1970]. Most of the early research on tides is focused on the computational model due to the lack of observations of the atmospheric tides [e.g., *Forbes and Garrett*, 1979; *Forbes*, 1982a, 1982b; *Vial and Forbes*, 1989]. One of the well-known tidal models is the Global Scale Wave Model (GSWM) developed in 1990s [*Hagan et al.*, 1993, 1995]. The GSWM is a steady-state two-dimensional linearized numerical model which calculates the height-latitude distribution of the atmospheric response from the ground to the thermosphere (>250 km) by giving the frequency, zonal wave number and excitation of a particular oscillation, with a specified zonally averaged atmospheric state. It has also been continuously updated during the last two decades [*Hagan and Forbes*, 2002; *Zhang et al.*, 2010a]. Some other tidal model work can also be found in many published papers [e.g., *Kato et al.*, 1982; *Lieberman and Leovy*, 1995]. Later on, with the appearance of spaceborne instruments, people can derive temperature and wind tides based on the global observational data. Some of the widely used instruments are, for instance, the SABER and TIMED Doppler Interferometer (TIDI) on board of the TIMED satellite [*Russell et al.*, 1999; *Killeen et al.*, 2006], MLS instrument, High Resolution Doppler Imager (HRDI), and Wind Imaging Interferometer (WINDII) on the Upper Atmosphere

Research Satellite (UARS), and MLS on the EOS Aura satellite. Some papers, for example, *Forbes and Wu* [2006], *Zhang et al.* [2006], and *Oberheide et al.* [2006] utilize these satellite observations of temperature and wind fields to delineate the global temperature and wind tidal structures in the middle and upper atmosphere. The advantage of the satellite observations is the full longitudinal coverage, which allows data users to separate the tidal components, as compared with the tides observed at a single ground-based station, which are the superposition of the migrating and nonmigrating tides [*Oberheide et al.* 2006; *Lu et al.*, 2011].

However, in fact, most of the satellite-data based results are confined to the low- and mid-latitude regions due to the orbit geometry. For example, SABER has year-round coverage only between ±50° latitudes due to the 180° yaw maneuvers every 60 days. Most of the temperature and wind tidal measurements in the Antarctica region are still provided by the ground-based instruments. The common instruments can be separated into two categories, the passive remote sensing instruments, such as all-sky imagers and interferometers, and the active remote sensing instruments, such as radars and lidars. The passive instruments, as mentioned in the previous section, are limited to operating during nighttime and are incapable of resolving range. But there are still valuable observations of tides, for example, *Azeem and Sivjee* [2009] reports 24, 12, and 8 h tidal signatures at South Pole station from the OH temperatures made by Michelson interferometer. As for the radar measurements, several wind tides observations are made by meteor and MF radars [e.g., *Avery et al.*, 1987; *Forbes et al.*, 1995; *Murphy et al.*, 2003, 2006]. It is worth mentioning that *Avery et al.* [1987] reports measurement of wind tides from 80 to 110 km at Manson station (78°S). Also, *Murphy et al.*, [2003] and *Murphy et al.* [2006] separate the tidal components between 80 and 96 km by using radar measurements at multiple longitudes but similar latitudes, which therefore share a common tidal component. As for the lidar measurements, so far, very few lidar observations of tides can be found. One is *Lubken et*

al., [2011], which reports summer temperature tides at Davis station (69°S) between 84 and 96 km by an Fe Doppler resonance lidar, and the other is *Fong et al.*, [2014], which reports winter temperature tides from 30 to 110 km at McMurdo station and is also a part of this dissertation (Chapter 2).

Since currently there are no satellite measurements available for temperature tides in Antarctica, the importance of the lidar measurement of temperature tides speak for itself. It can provide not only the measurements of the temperature tides in the middle and upper atmosphere, but it can also help verify models at high latitude region. For example, *Lubken et al.* [2011] shows greater amplitudes of temperature tides than those predicted by GSWM in the MLT region.

1.3 Brief Review of Resonance Fluorescence Temperature Lidar

Resonance fluorescence lidar is now one of the common methods for people to measure temperature, wind, and constituent in the middle and upper atmosphere by tracing the metallic neutral atoms, such as Fe, Na, K, and etc, that are distributed in the MLT region. These metallic neutral atoms are believed to originate from meteor ablation. Because the backscatter cross-section area of resonance fluorescence is about 10^{14} times higher than Rayleigh backscatter cross-section, even though the density of tracer atoms is about 10^{10} times less than the atmosphere molecular density in the MLT region, the overall resonance fluorescence signal is still a few order of magnitudes higher than the Rayleigh signal in this region. Therefore, resonance fluorescence lidars can generate useful photon signals to derive atmospheric parameters in the MLT region. The resonance fluorescence lidar can be roughly separated into three categories, broadband resonance fluorescence lidar, Doppler lidar, and Boltzmann lidar. A

detailed introduction to the resonance fluorescence lidar can be found in *Chu and Papen* [2005]; here we just give a brief review of the development of these resonance fluorescence lidars.

Following the progress of the development of the resonance fluorescence lidar, the first lidar was made to observe the mesospheric Na layer in 1960s [*Bowman et al.*, 1969]. Later on, other metal species, such as K, Li, Ca, Ca^+, and Fe, were also measured by the broadband resonance fluorescence lidars [e.g., *Felix et al.*, 1973, *Jegou et al.*, 1980, *Qian and Gardner*, 1995, *Bills and Gardner*, 1990]. Even more, *Collins et al.* [2015] report the first lidar measurement of mesospheric Ni layer recently. Except for the newly reported Ni lidar, the broadband lidars are not to be suitable for temperature or wind measurement since the spectral width of the laser pulse are much larger than the absorption of the resonance lines. However, these lidars still provide valuable measurements of atmospheric constituents and also trigger the study of wave activity in MLT region.

The first narrowband Na lidar to observe the mesospheric Na ground-state hyperfine structure was demonstrated by *Gibson et al.* [1979], which inspired the temperature and wind measurements by lidar in the MLT region later. *Fricke and von Zahn* [1985] made the first lidar campaign at Andøya, Norway (69°N) which was able to retrieve the MLT region temperature profiles routinely. Later on, *She et al.* [1990] and *Bills et al.* [1991] achieved more precise temperature measurements via two-frequency technique for which the lidar system became the prototype of the modern Na Doppler lidar system. The introduction of the remarkable dual-channel acoustic-optic modulator (AOM) idea by *She and Yu* [1994] enabled the simultaneous temperature, wind, and Na density measurements. This dual-channel AOM module allows rapid switching between three laser pulse frequencies and is common in Na Doppler lidar system nowadays (see Section 1.4.2).

When the Na Doppler lidar system gradually matured in 1990s, *Gelbwachs* [1994] proposed the idea of Fe Boltzmann lidar. This lidar excites two absorption lines of neutral Fe atoms at 372 and 374 nm, and then the temperature can be derived from Maxwell-Boltzmann distribution law. A Boltzmann lidar was built few years later and was able to perform temperature and Fe density measurements [*Chu et al.*, 2002]. Furthermore, this Boltzmann lidar system demonstrated excellent tolerance to the environment compared to most of the Doppler lidar systems and could still provide robust temperature measurements under harsh environments, such as on the aircraft or at remote sites like South Pole [e.g., *Gardner, et al.*, 2001; *Chu, et al.*, 2000, 2003]. The Fe Boltzmann lidar has relatively broad laser spectral bandwidth comparing with the Doppler lidar, but it does not affect the temperature retrieving since the concepts of the two kinds of the lidar are different. Currently, this Fe Boltzmann lidar system is still providing measurements in the McMurdo lidar campaign (see section 1.3.1).

Nowadays, with the compelling needs of advancing our understandings of the middle and upper atmosphere, the robust measurements of the neutral wind in the MLT region along with the temperature are necessary. In the past few years, the University of Colorado Boulder lidar group has been developing a 3-frequencies mobile Fe resonance/Rayleigh/Mie Doppler lidar, ambitiously aiming to improve the temperature and wind measurement accuracy of resonance Doppler lidar to an unprecedented level (~0.1 K and 1 cm/s) for new science endeavors [*Chu and Huang*, 2010]. The choice of Fe Doppler lidar is coming from the combination of high Fe abundance, thus stronger Rayleigh scattering for larger Rayleigh temperature range, high temperature and wind sensitivity, and deep Fraunhofer line in solar spectrum (low daytime solar background) [*Chu and Huang*, 2010]. This lidar is based on the injection-seeded frequency-doubled Pulsed Alexandrite Ring Laser (PARL) with master oscillator operated at 744 nm [*Chu*

et al., 2010], which is one of the state-of-the-art lidars in the world. Currently, the lidar system is installed in the Table Mountain lidar facility in Boulder.

Furthermore, this Fe Doppler lidar has also inspired the newly installed 3-frequency K (potassium) Doppler lidar system at Arecibo Observatory, Puerto Rico in the summer of 2014. With the similar PARL technology but operating at 770 nm for K absorption peak, it can also be altered to an Fe Doppler system by tuning the operating wavelength to 772 nm and adding frequency-doubling stage to obtain 386 nm lidar pulses. In fact, *Lautenbach and Höffner* [2004] demonstrated a method of measuring temperature in the MLT region by using a frequency-doubled alexandrite laser to scan Fe absorption line at 386 nm. *Höffner and Lautenbach* [2009] also reported the daytime measurements of temperature and vertical wind with the same scanning lidar.

1.3.1 McMurdo Campaign and Fe Boltzmann Lidar

Long-term and range-resolved temperature measurements with full-year and full-diurnal coverage are very rare at southern high latitudes. To fill a critical data gap in observations of the middle and upper atmosphere between the South Pole and the Antarctic Circle [*Chu et al.*, 2003, 2004; *Gardner et al.*, 2005, 2011; *Pan et al.*, 2002; *Pan and Gardner*, 2003], the University of Colorado lidar group deployed an Fe Boltzmann lidar to McMurdo Station (77.83°S, 166.67°E) in December 2010 and has collected over 5000 hour lidar data since then [*Chu et al.*, 2011a, 2011b]. McMurdo station is located on the southern tip of Ross Island, near the continent of Antarctica (see Figure 1.1). The McMurdo lidar campaign is a collaboration between the United States Antarctic Program (USAP) and Antarctica New Zealand (AntNZ). Our lidar group

successfully installed the lidar system in the AntNZ facility at Arrival Heights near McMurdo, and the first Fe signals were obtained on 16 December 2010.

Originally developed at the University of Illinois over a decade ago [*Chu et al.*, 2002], the Fe Boltzmann lidar consists of two independent, zenith-pointing channels probing the absorption lines of neutral Fe atoms at 372 and 374 nm in the MLT region. The ratios between these two channels are used to derive the Fe temperature by employing the Boltzmann technique [*Gelbwachs*, 1994; *Chu et al.*, 2002]. Below the Fe layers (≤75 km) and above aerosol layers in the lower atmosphere (≥30 km), the lidar can be used as a Rayleigh scattering lidar and thus the temperature is also derived in this altitude range [*Hauchecorne and Chanin*, 1980]. The Fe Boltzmann lidar system is capable of full-diurnal measurements of Fe density and temperature owing to the narrowband interference filters and Fabry-Perot etalons employed in the lidar receivers and the high-power pulsed alexandrite lasers employed in the lidar transmitters.

Figure 1.1. The map of Antarctica.

Over the last two decades, this lidar was deployed to the Pacific Ocean, the North Pole, the South Pole, and Rothera station, Antarctica, all of which are harsh environments [*Chu et al.*, 2000; *Gardner et al.*, 2001, 2005, 2011]. Refurbishment and upgrade of the lidar system were necessary before deploying it to McMurdo station. More importantly, new technologies, including optical and electronic, have been invented in the last decade. Implementation of these new technologies into the existing lidar system significantly improved its performance and enhanced its ability to conduct the polar observations. Such refurbishment and upgrade along with extensive sky tests were conducted at the University of Colorado [*Wang et al.*, 2012]. It also led to the Boulder campaign of simultaneous and common-volume observations with a Na Doppler lidar (see 1.4.2) in August and September of 2010. Such simultaneous Fe and Na lidar observations have resulted in a few rare science investigations [*Huang et al.*, 2013].

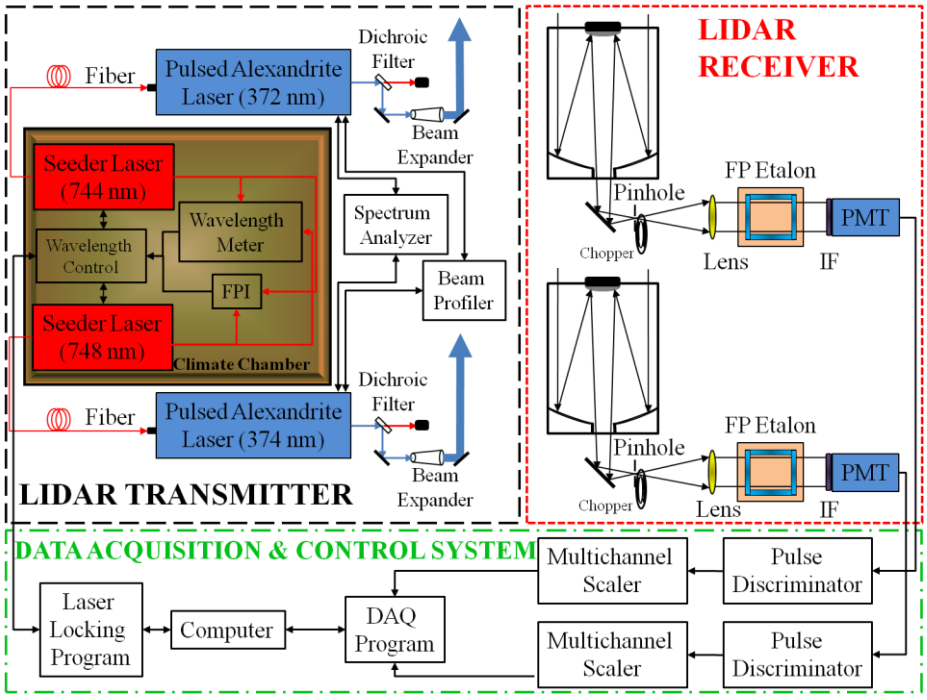

Figure 1.2. Schematic diagram of the upgraded Fe Boltzmann and Rayleigh temperature lidar system at McMurdo Antarctica [*Wang et al.*, 2012].

The schematic diagram of the upgraded lidar system is illustrated in Figure 1.2. The upgrades of the lidar system were mainly focused on the laser injection seeding, data acquisition (DAQ) program, and wavelength control system. In the laser injection seeding part, firstly, the original seed lasers, Newport EOSI external cavity diode laser (ECDL) model 2010, were replaced with two new ECDLs, model DL-100 (372 nm channel) and DL-Pro (374 nm channel), manufactured by Toptica. The new ECDL has higher output power and stability which improves spectral purity and also the stability of the Pulsed Alexandrite Laser (PAL). Secondly, to prevent the interferences from the surrounding, such as mechanical vibrations and temperature fluctuations, the two ECDLs and a scanning Fabry-Perot Interferometer (FPI) are setup in a sealed climate chamber, as shown in Figure 1.3.

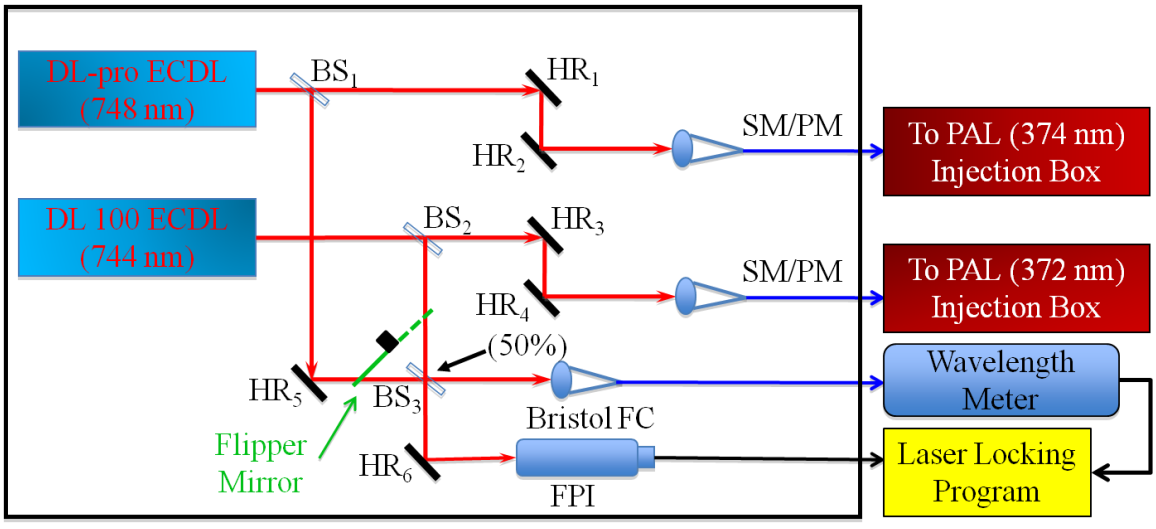

Figure 1.3. Experimental setup for the injection seeding and wavelength control system. Equipments and optics in the black square are setup in a sealed climate chamber.

Both the new DAQ and wavelength control programs are LabVIEW-based programs with more efficient algorithms and programming with several additional software functionalities implemented. The DAQ program works with the multichannel scalar SR430 device via GPIB card to collect the return photon counts, and then accumulates the signals to certain laser shots before writing the raw profiles into the data storage area. Also, the instant signal statistics enable operators to monitor the relative movement of telescope and lidar beam on field overlap and to respond quickly to any sudden change of the returning lidar signals. The wavelength control program includes both seed laser wavelength locking and laser mode monitoring. The wavelength locking is achieved based on the reading given by wavelength meter and the LabVIEW-based PID servo loop, and the mode of seed laser is monitored by a scanning FPI with free spectral range (FSR) of 1.5 GHz. As one can see from Figure 1.3, the wavelength locking and the laser mod monitoring of both channels are achieved at the same time by the computer-controlled motorized flipper mirror (beam blocker). More detailed descriptions of the upgrades and refurbishments of the system can be found in *Wang et al*. [2012].

Currently, the final divergence angles of the two lidar beams are ~0.35 mrad, producing spots of 35 meter in diameter at the altitude of 100 km. The raw lidar data are taken in 48 meter and 1 minute (2000 lidar pulse shots) resolutions. The McMurdo lidar campaign has made lots of valuable observations since the completion of the deployment at McMurdo in 2010, including polar mesospheric clouds (PMCs), neutral Fe layers, temperatures and fast gravity waves in the thermosphere, inertia gravity waves (IGWs), planetary waves (PWs), winter temperature tides, explosive growth of Fe layer density during the PMC season, solar effects on Fe layer bottom side, and many ongoing investigations. Especially the investigation of the thermospheric Fe layer opens a new door for thermospheric sciences study. It is the first time that ground based lidar reported the Fe layer extending up to altitude 155 km [*Chu et al.*, 2011b]. Moreover, during the

lidar run later in the night of 1st June, 2013, the lidar observed that the Fe layer extended up to 170 km.

1.3.2 STAR Lidar at University of Colorado Boulder

The Student Training and Atmospheric Research (STAR) lidar is a Na (sodium) Doppler system built at the University of Colorado Boulder. The lidar system was constructed by Dr. Chu's graduate students in the summer of 2010, and it employs a classical dye-lidar-based transmitter and is similar in design to the Na Doppler lidar systems developed by the Colorado State University (CSU) and the University of Illinois at Urbana-Champaign (UIUC) lidar groups (see summaries by *Arnold and She* [2003] and *Chu and Papen* [2005]). Originally aimed for student training purposes, its scientific research values were soon recognized and demonstrated by *Smith et al.* [2012] and *Huang et al.* [2013]. *Smith et al*. [2012] show the innovative approaches to achieve high optical efficiency in the STAR lidar receiver and demonstrate the capability for high resolution measurements of Na layer in the MLT region, which enables new studies of the middle and upper atmosphere, such as Eddy flux and small scale layer turbulence. Plotted in Figure 1.4 is an example of the STAR lidar observation of the Na layer. The high signal clearly reveals the fine structure of the Na bottom layer. The STAR lidar also participated in the Boulder lidar campaign of simultaneous measurement of Na and Fe layer with the upgraded Fe Boltzmann lidar system in August and September of 2013 [*Huang et al*., 2013].

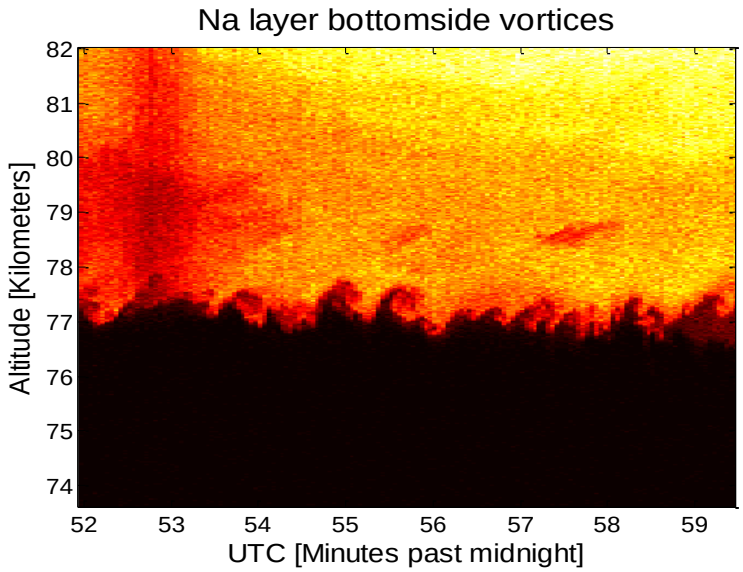

Figure 1.4. High resolution Na density taken by STAR lidar on 8th December, 2011. The lidar power is about 400 mW and the receiver is a 32" Newtonian telescope primary mirror. The raw data resolution is 24 meter and 3 second (30 lidar shot for each frequency). The average Na layer shot count is ~1500 per lidar pulse. Figure is provided by Dr. John Smith.

Figure 1.5 shows the system schematic diagram of the STAR lidar. It combines a classical Na Doppler lidar of dye-laser based master oscillator power amplifier (MOPA) transmitter design with modern data acquisition and control systems. The transmitter consists of master oscillator, Na saturation-absorption spectroscopy for laser frequency locking, acoustic-optic modulators (AOM) path, and the pulsed amplification stage. A slight difference compared to the Na Doppler lidar system at CSU and UIUC is that the frequency shifts by the dual AOMs are ±480MHz, instead of ±630 MHz. In November of 2013, the STAR lidar implemented a new set of AOMs with frequency shift of ±750 MHz for measuring vertical fluxes of heat and constituent. One vertical-pointing lidar beam (switching among three frequencies) of 0.8 mrad divergence was employed for the current study, producing a spot of ~80 meter in diameter at 100 km altitude. By employing the three-frequency technique to probe the Na D_{2a} line, the temperature, line of sight wind, and Na density can be derived simultaneously [*Chu and Papen*,

2005]. The design of Na saturation-absorption for laser frequency locking can also be found in [*Smith et al.*, 2008, 2009].

The STAR lidar receiver has been migrated from a 16" Cassegrain telescope to a 32" Newtonian telescope. For the Newtonian telescope, the lidar utilizes a prime focus setup, that is, the secondary mirror of the Newtonian telescope was removed and the photo detector or fiber is mounted directly at the focus of the primary mirror. The prime focus setup has several advantages compared with the Cassegrain-type or Newtonian with secondary mirror, such as increasing the usable area of the primary mirror, simplifying the alignment procedures of the telescope, and lowering the cost per unit collection area. These advantages can improve not only the optical efficiency of the lidar receiver, but also make it becomes more suitable for a mobile and containerized lidar. Furthermore, the various post-telescope receiver chain configurations had also been tested with the help of optical model software ZEMAX, such as direct PMT couple and fiber/PMT couple configurations [*Smith et al.*, 2012; *Smith and Chu*, 2015]. They were proven to achieve the peak performance, that is, the observation results agree with the lidar simulations. During winter season, usually when peak abundance of Na layer occurs among a year, the STAR lidar can reach 1000-2000 counts per lidar beam shot with transmitting output power of ~0.5 W at 30 Hz repetition rate.

In this dissertation, we investigate how the temperatures and radial winds would be affected by the spectrum of the lidar pulses, including the line shape, linewidth, and central frequency offset to the Na D_{2a} center, using the forward model. These are important factors that play roles in temperature and wind errors and are crucial for study the temperature/wind structure and climatology.

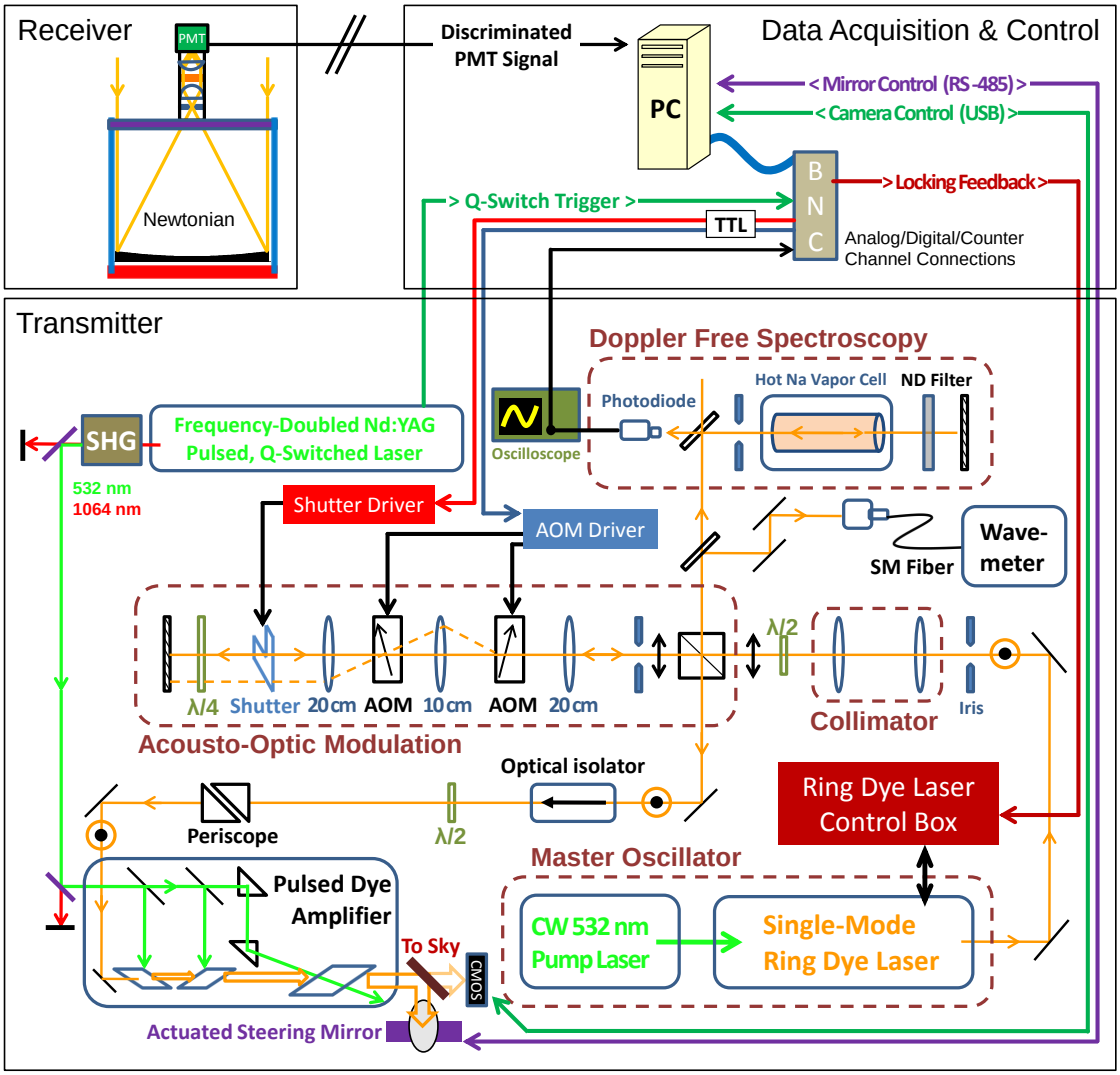

Figure 1.5. Layout of the STAR lidar showing dye laser based MOPA transmitter, Newtonian telescope receiver and PC/LabVIEW control and data acquisition systems [*Smith et al.*, 2012].

1.4 My Winter-Over Lidar Work at McMurdo Station

From August of 2012 to October of 2013, I worked at McMurdo station as the winter-over lidar scientist for the Fe Boltzmann temperature lidar campaign. In fact, prior to the challenging 14-month long journey in Antarctica, I also participated in both the lidar preparation in Boulder in 2010 and the lidar system installation at Arrival Heights during the summer season of 2010−2011. The lidar campaign and system was briefly introduced in the previous section.

The lidar system has been installed in the AntNZ research facility at Arrival Heights, which is a small range of hills about 1.5 km north of McMurdo station and 3 km northwest of Scott Base. The lidar is accompanied by many other scientific project instruments, such as MF radar and VLF radar. Arrival Heights is about 220 m above sea level and is protected as Antarctic Specially Protected Area (Area) for its value in atmospheric and space science studies. It was designated an electromagnetic and natural "quiet zone", which offers ideal conditions for sensitive instruments to record small signal associated with upper atmosphere projects. The other advantage is the close distance to the full logistic support of nearby stations. Also, due to its close proximity to McMurdo station, we usually count Arrival Heights as part of McMurdo station when comparing the lidar system and data with those at the other locations.

Due to the harsh environment and limited supports, the installation work at McMurdo was very challenging. The lidar team encountered many difficulties, such as the corrosion of equipments due to the sea water during shipping and the accidental damage to the aluminum frame structure during transportation. Moreover, the toughest one was the electromagnetic interference (EMI) issue with other scientific projects. After numerous diagnosis and tests, the source of the EMI was found to be the poor isolation of the power grid at Arrival Heights. Fortunately, the lidar team conquered all the obstacles beautifully, and the EMI was solved by installing an extra secondary transformer at Arrival Heights facility and adding line filters in the pulsed alexandrite laser power consoles.

My 14-month stay at McMurdo was successful and an invaluable lifetime experience. The lidar duty transferred from my colleague, Mr. Brendan Roberts, the winter-over lidar scientist in 2012, to me was very smooth. We performed the wavelength scan for both 372 nm and 374 nm channels in August and September 2012 while there were still dark nights, and the 372 nm receiver chain was realigned. In the following summer season, a major upgrade of laser

pump chamber and several maintenance work of the system led by Dr. Xinzhao Chu were also accomplished successfully, which set a solid base for winter operation in 2013. During winter, most of the lidar runs went pretty smoothly even though there were a few times that the weather turned bad soon after the data collection started. The lidar duty turn over from me to my colleague and successor Mr. Cao Chen was very dramatic and almost turned into a disaster due to the government shutdown in October 2013, we still managed to keep the lidar campaign moving with the help of USAP staff and the weather. The continuous bad weather during the government shutdown prevented the flight from coming in to McMurdo, which supposed to fly me out of Antarctica. Fortunately, the government was re-opened one day before the weather turned good, so I was allowed to stay at McMurdo and turned over my duty to Cao after the flight flew him to McMurdo.

Overall, the total of ~1250 hours of data was collected from September 2012 to the end of October 2013. It is worth mentioning that on 1st June 2013, the lidar data showed the first case that thermospheric Fe layer can extend up to ~170 km under strong geomagnetic storm. During this event the temperature can be derived to over 160 km (Figure 1.6). Also, besides the newly observed thermospheric Fe layers events, these lidar data have also contributed to several scientific topics such as inertia gravity waves, temperature tides and temperature structures. In this dissertation, the 2013 winter data is used for diurnal tide derivation in Chapter 3 and the whole 14 months of data were used in the temperature climatology study in Chapter 4. Moreover, in the future, the data will also serve as the baseline for measurements decades from now to compare with to assess/monitor climate changes and many other science topics.

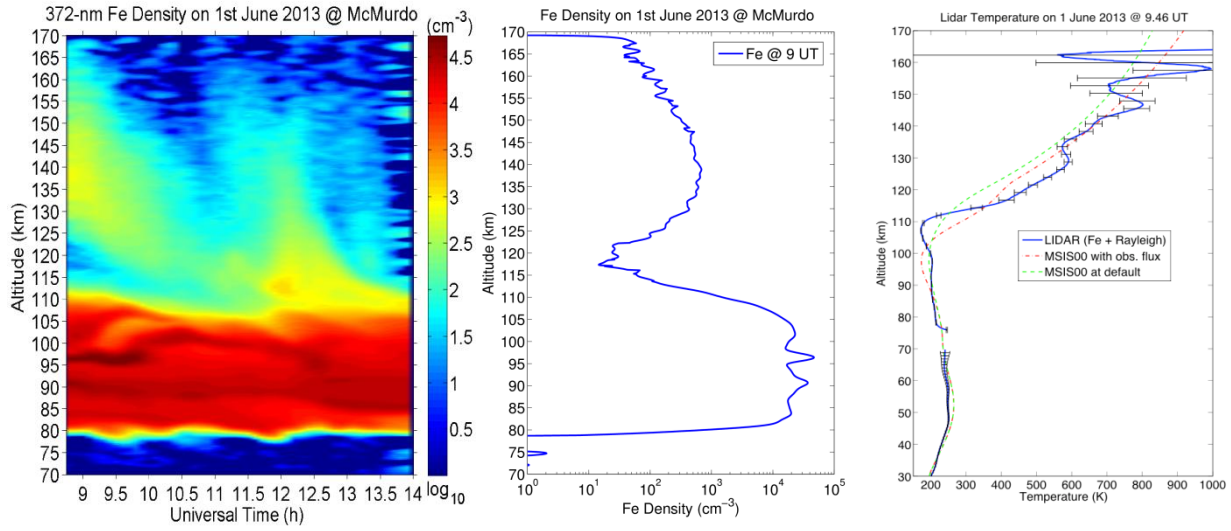

Figure 1.6. Measurements by an Fe Boltzmann temperature lidar at McMurdo, Antarctica have shown (Left and Middle) neutral Fe layers extending as high as 170 km on June 1st, 2013 and (Right) the vertical profile from 30 to ~170 km of temperature at 9.46 UT [*Chu et al.*, AGU, 2013].

1.5 Arrangement of Dissertation

This dissertation involves three parts, the first part is the lidar observations and the modeling studies of winter temperature tides at McMurdo, and the second part is the temperature climatology at McMurdo, and the last part is the evaluation of temperature and wind observation uncertainties of a Na Doppler lidar.

The observation of winter temperature tides using lidar data from 2011 to 2012 will be presented in Chapter 2, which is the journal paper published by *Fong et al.* [2014] in the Journal of Geophysical Research-Atmospheres. Chapter 3, following the lidar observation results in Chapter 2, presents the mechanism study of the fast growth of diurnal temperature tides above 100 km using the Coupled Thermosphere Ionosphere Plasmasphere Electrodynamics (CTIPe) model, and most of the results have been published by *Fong et al.* [2015] in Geophysical Research Letters. Chapter 4 presents the temperature climatology at McMurdo using 4 year of lidar and radiosonde observations from 2011 to 2014, which is a draft of a journal paper in

preparation. In Chapter 5, the forward model method is used to assess the uncertainties of temperature and radial wind measurements of 3-frequency Na Doppler lidar system at CU Boulder caused by possible short-term variability of lidar instruments. Lastly, the conclusions and future outlook is presented in Chapter 6.

CHAPTER 2

Winter Temperature Tides from 30 to 110 km at McMurdo (77.8°S, 166.7°E), Antarctica: Lidar Observations and Comparisons with WAM

2.1 Introduction

Atmospheric tides are global-scale oscillations in pressure, density, temperature, and wind fields, for which the periods are harmonics of a solar day. They can be classified as migrating (Sun-synchronous) and nonmigrating (non-Sun-synchronous) tides according to their horizontal phase velocities, i.e., migrating tides follow the motion of the Sun. The driving forces of migrating tides are mainly periodic absorption of solar radiation in the atmosphere and those for nonmigrating tides are mainly latent heat release in the tropical region [*Hagan and Forbes*, 2002; *Zhang et al.*, 2010a, 2010b] and nonlinear interactions between planetary waves and migrating tides [*Hagan et al.*, 2001; *Angelats i Coll and Forbes*, 2002; *Murphy et al.*, 2009]. Tides can obtain large amplitudes in the middle and upper atmosphere, where they modulate ionospheric variability via the E-region dynamo effect [*Forbes et al.*, 2000, 2008], enhance vertical atmosphere coupling [*Forbes et al.*, 2000; *Immel et al.*, 2006] and cause instabilities by inducing significant temperature gradients and wind shears [*Hecht et al.*, 1997; *Liu et al.*, 2004]. Tides affect the propagation of gravity waves (GWs) [*Walterscheid*, 1981; *Lu et al.*, 2009] and modulate GW momentum fluxes [*Fritts and Vincent*, 1987; *Espy et al.*, 2004; *Liu et al.*, 2013].

Tides also impact the vertical transport of atmospheric constituents and thereby the total solar heating in the upper part of the middle atmosphere [*Smith et al.*, 2003].

Numerous observations have been carried out to characterize tides in the tropical and sub-tropical regions. However, in the polar region observations of temperature tides are rare due to the lack of suitable temperature measurements. For satellite measurements, only observations from precessing satellites have the local time coverage needed for tidal studies, such as the Microwave Limb Sounder (MLS) on the Upper Atmosphere Research Satellite (UARS) and the Sounding of the Atmosphere using Broadband Emission Radiometry (SABER) on the Thermosphere Ionosphere Mesosphere Energetics and Dynamics (TIMED) satellite. Even so, they are constrained by the orbital geometry and have limited coverage for high latitudes. For instance, SABER can only cover latitudes from 52°S to 83°N during most of the wintertime in the Southern Hemisphere [*Russell et al.*, 1999] and the MLS on UARS only covers from 34°S to 80°N in May and July [*Forbes and Wu*, 2006]. There have been several studies of wind tides in the Antarctic region using ground-based radar observations, and particularly nonmigrating semidiurnal tide with wavenumber 1 has been extensively studied [*Forbes et al.*, 1995; *Portnyagin et al.*, 1998; *Baumgaertner et al.*, 2005, 2006; *Murphy et al.*, 2003, 2006, 2009; *Hibbins et al.*, 2010]. Unfortunately, there is no simple relationship between tides in winds and those in temperatures since the latitudinal structures of their respective Hough modes are different. Considering the facts that temperatures critically determine chemistry, composition and dynamics of the middle and upper atmosphere, and directly reflect the impacts of solar radiation and Joule heating, the information of temperature tides is therefore important and greatly needed, especially in the polar regions. Airglow imagers can also observe temperature tides [*Hernandez et al.*, 1993; *Azeem and Sivjee*, 2009], but only at the emission altitude of the species and thus are incapable of providing tidal vertical profiles. Lidar observations at Davis Station (69°S) in the

Antarctic have provided a vertical profile of temperature tides in the summer [*Lübken et al.*, 2011]. Contrary to the conventional understanding that temperature tides are small in the polar region, *Lübken et al.* [2011] report that tides can induce a non-negligible temperature oscillation (up to 6 K) in the summer Antarctic mesopause region, although the tidal characterization was limited to a narrow altitude range (84−96 km).

A significant gap remains in observing and understanding temperature tides over a large altitude range in the Antarctic. Long-duration, large-altitude-range and high-resolution lidar measurements on temperatures can be used to fill in this gap. In this paper, we provide the first report and characterization of the amplitudes and vertical wavelengths of temperature tides in the Antarctic winter from 30 to 110 km using the two-year lidar measurements in 2011 and 2012 at Arrival Heights, McMurdo (77.8°S, 166.7°E) [*Chu et al.*, 2011a,b]. The lidar deployed is an iron (Fe) Boltzmann temperature lidar using pulsed alexandrite lasers (see details in *Chu et al.* [2002] and *Wang et al.* [2012]). It has an exceptionally large altitude coverage of temperatures from 30 to ~110 km, and during thermospheric Fe layer events it can even measure temperatures from 30 to 150 km [*Chu et al.*, 2011b].

Revealing tides from such high latitude like McMurdo is not trivial because large-amplitude inertia-gravity waves (IGWs) in the MLT [*Chen et al.*, 2013] and planetary waves (PWs) in the stratosphere [e.g., *Lu et al.*, 2013; *McDonald et al.*, 2011; *Alexander and Shepherd*, 2010; *Randel*, 1988; *Andrews et al.*, 1987] can contaminate the tidal signals. We apply a composite day method to extract tides from numerous waves present in the Antarctic winter, and develop a forward model to assess the aliasing effects from IGWs and PWs. The new features discovered include the rapid growth of diurnal and semidiurnal tidal amplitudes above 100 km, and the larger tidal amplitudes and faster growth rates in the lower thermosphere corresponding to larger Kp indices. Simulations from the Whole Atmosphere Model (WAM) compare

reasonably well with lidar observations despite some discrepancies. Consequently, WAM is used as a reference to reveal the dominant components of diurnal and semidiurnal tides in the Antarctic winter.

2.2 Lidar Observations and Data Analysis

2.2.1 Lidar Data and Composite-Day Analysis

The University of Colorado lidar group is conducting a lidar observational campaign at Arrival Heights (77.83°S, 166.67°E), McMurdo on Ross Island. This campaign is a collaboration between the United States Antarctic Program (USAP) and Antarctica New Zealand (AntNZ). Since the first data collection in December 2010, observations have been ongoing for over 2.5 years. The Fe Boltzmann lidar deployed in the campaign is capable of temperature measurements during both day and night, leading to full diurnal data coverage. Temperatures were derived from 30–70 km using the Rayleigh integration technique [*Hauchecorne and Chanin*, 1980] and from 80–110 km using the Fe Boltzmann technique [*Gelbwachs*, 1994]. The gap between 70 and 80 km exists because neither the Rayleigh nor Fe signal level is sufficient to derive accurate temperatures in this region. For convenience, we name the 30−70 km and 80−110 km regions as the Rayleigh region and Fe region, respectively.

The data used in this study were collected during the Antarctic winters (from May through August) in both 2011 and 2012 when the solar elevation was low. Such low background leads to high-quality temperature measurements. We further screen the data and remove outliers that have low signal-to-noise ratios, usually due to clouds. The 334 h of high quality data used in this study are distributed as follows: May (93 h), June (122 h), July (57 h) and August (62 h). The raw lidar data of photon counts were recorded in resolutions of 1 min and 48 m. In the

current tidal study, we reduce the temperature resolutions to 1 h and 1 km. At these reduced resolutions, typical measurement uncertainties of single temperature profiles are less than 1 K in the altitude ranges of 30–55 and 83–100 km, but vary between 1–10 K in the ranges of 55–70, 80−83 and 100–110 km.

As mentioned earlier, a major challenge of the tidal analysis at this high southern latitude is interference from IGWs in the MLT region and PWs in the stratosphere. IGWs are strong and frequently observed at McMurdo with dominant wave periods ranging between 4 and 9 h [*Chen et al.*, 2013]. The observed amplitudes of IGWs are usually on the order of 10–20 K and these waves can last over 20 h. In addition, *Lu et al.* [2013] reported that the eastward propagating PWs (relative to the ground) with periods of 1–5 days are prominent and long-lived in the winter stratosphere at McMurdo. Such PWs can induce temperature increases/decreases on the order of 10–20 K within a day, which have been frequently detected by the Fe lidar in the stratosphere at McMurdo. Furthermore, there are also reports of quasi-stationary PWs (QSPW) and long-period PWs in the Antarctic region [e.g., *Alexander and Shepherd*, 2010; *Randel*, 1988; *Andrews et al.*, 1987]. The aliasing signal from these large-amplitude waves must be sufficiently suppressed before tidal waves can be reliably derived. Fortunately, despite the large amplitudes of IGWs and PWs, their phases are incoherent from day to day, unlike the forced tidal waves that are coherent over long periods of time. Therefore, we use the composite day method to significantly reduce the incoherent wave effects while preserving the coherent tides.

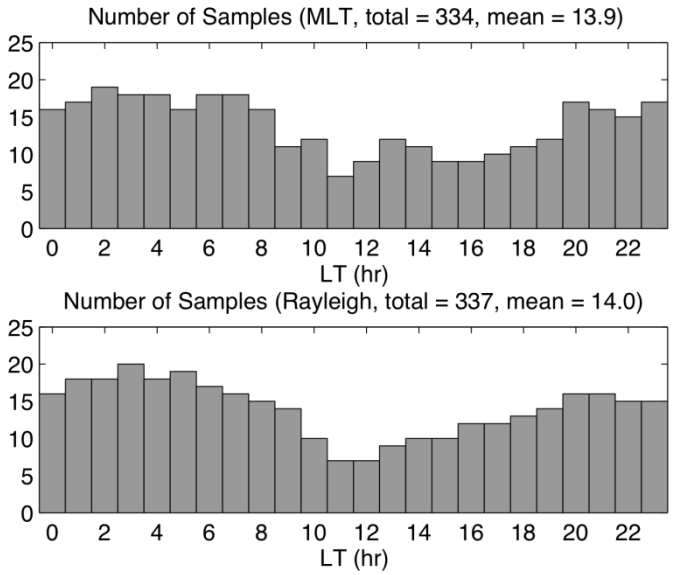

Figure 2.1. Diurnal distribution of hourly lidar data samples taken from May through August in 2011 and 2012 at McMurdo, separated into the (a) MLT and (b) Rayleigh regions. These data are used to compile temperature perturbations for the winter season. The total numbers of hourly samples are 334 and 337 for the MLT and Rayleigh regions, respectively.

A composite day of data covers a diurnal cycle (24 h) obtained through averaging either the absolute temperature measurements or temperature perturbations in the same local time (LT) and at the same altitude bin on different days within a chosen period, e.g., one month or the winter season. More data samples in the same time and altitude bin result in better suppression of the incoherent waves, in addition to reduce the measurement uncertainty of temperature for each bin. If the original temperature uncertainty at 1 h and 1 km resolutions is ΔT and the number of independent samples is N for a bin, the temperature uncertainty of this bin after averaging over these samples is given by $(\Delta T)_{ave} = \Delta T / \sqrt{N}$. The diurnal distribution of the sample numbers for the two winters in both Fe and Rayleigh regions are plotted in Figure 2.1. The minimum number of temperature samples is 7 at 11 LT in both regions, and the maximum number of samples is 19 at 2 LT for the 80–110 km and 20 at 3 LT for the 30–70 km. The mean number of temperature samples for each hour of the day through the cumulative May–Aug period in two winters is about 14. For this amount of data, there are sufficient samples over the winter season to derive

the tides, but not for each individual month. Therefore, we use the two winter data to compose a 24-h day and study the winter temperature tides, instead of monthly tides.

To form a composite day of temperature perturbations for the winter season, we first derive the composite day of temperature perturbations for each month via subtracting the monthly-mean temperature from the monthly composite. A total of eight monthly composite days of temperature perturbations in the two years are then averaged to obtain the winter composite day of temperature perturbations. A Hamming window with a full width of 5 h is then applied to further suppress the high frequency structures that remain in the temperature perturbations. The smoothed temperature perturbations are shown in Figure 2.2a with resolutions of 1 h and 1 km. Compared to the individual day of temperature perturbations illustrated in Figure 1 in *Chen et al.* [2013], the IGW signatures have been significantly reduced in Figure 2.2**Figure 2.2**a.

However, as long as the temperature perturbations induced by IGWs and PWs can be folded into the 24-h composite day and have spectral components close to tidal periods, the aliasing effects from IGWs and PWs can be non-negligible since their spectral leakages to diurnal and semidiurnal tides can still exist. Thus, a forward model is built to assess the aliasing impact caused by IGWs and PWs (see section 2.6) and help answer the question of how the large amplitude and phase incoherence of IGWs and PWs balance out each other and result in the overall uncertainties in deriving diurnal and semidiurnal tides. Forward model results will be discussed in conjunction with the lidar results in the following sections. But in short, we have found that the aliasing effects are negligible by applying the composite-day method and 5-h Hamming smoothing.

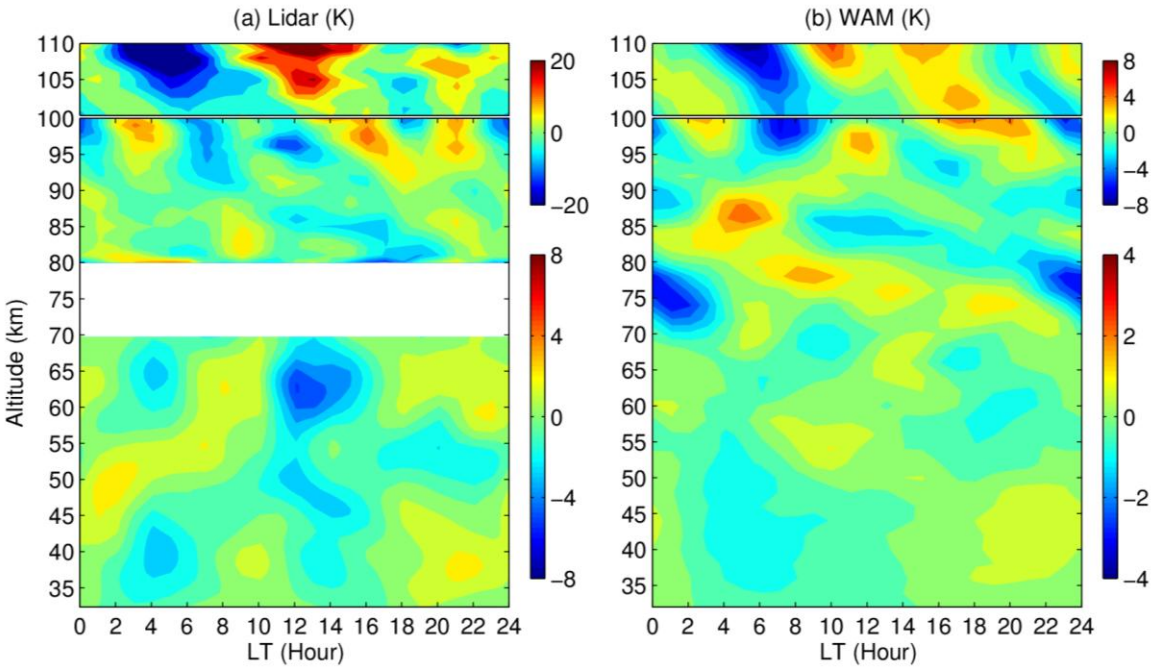

Figure 2.2. Hamming smoothed composite contours of temperature perturbation for a 24-h cycle from: (a) the observations of an Fe Boltzmann temperature lidar at McMurdo (77.8°S) from May to August of 2011 and 2012; and (b) four months of WAM output from May to August. The full Hamming window width is 5 hour. The temperatures below and above 100 km are indicated by the bottom and top colorbars, respectively.

2.2.2 Tidal Amplitudes, Phases and Vertical Wavelengths

In Figure 2.2a, it can be seen that the temperature perturbations of the winter composite vary between 3 and 6 K below 100 km while the perturbations increase rapidly above 100 km. The ridge-to-trough magnitudes of perturbation can reach nearly 40 K above 105 km. Also, downward phase progressions are clearly seen in the MLT region, indicative of upward propagating waves. Moreover, tidal signatures, i.e., the diurnal and semidiurnal variations, are appreciable in both the Rayleigh and Fe regions. For instance, in the Rayleigh region, considerable diurnal variations can be found between 50 and 55 km, with a cold phase before midnight (LT) and warm phase after that; semidiurnal variations can be found between 35 and 42

km, with a warm phase at about 9 and 21 LT. In the Fe region, semidiurnal variations can be seen around 95 km, with two cold phases found at 0 and 12 LT.

To delineate diurnal and semidiurnal tidal amplitudes and phases, we apply a harmonic fitting model comprising a mean temperature plus a diurnal tide and a semidiurnal tide to the composite dataset shown in Figure 2.2a:

$$\hat{T}(z,t) = T_o(z) + A_{24}(z)\cos\left[\frac{2\pi}{24}(t - P_{24}(z))\right] + A_{12}(z)\cos\left[\frac{2\pi}{12}(t - P_{12}(z))\right], \qquad (2.2.1)$$

where T_o is the diurnal mean, A_{24} and A_{12} are the amplitudes, and P_{24} and P_{12} are the phases of the diurnal and semidiurnal tides, respectively. Tidal phase is defined as the local time when temperature reaches the maximum. The obtained tidal amplitudes and phases are plotted in Figure 2.3. In general, lidar observed diurnal and semidiurnal tidal amplitudes are less than 3 K from 30 to 100 km, and rapidly increase with altitude above 100 km. The mean amplitudes in the Rayleigh region are 1.1 K and 1.2 K for diurnal and semidiurnal tides, respectively. The counterparts are 1.1 K and 1.0 K in the altitude range of 80−100 km. We feed these mean tidal amplitudes into the forward model (section 2.6) as the parameters of the diurnal and semidiurnal tidal amplitudes and find that the aliasing effects of IGWs in the Fe region on the diurnal and semidiurnal tides are about 10% and 30% (~0.1 K and ~0.3 K), respectively. Meanwhile, the effects of PWs in the Rayleigh region are about 33% and 10% (~0.3 K and ~0.1 K), respectively. It is expected that when the tidal amplitudes are small the relative aliasing effects from the IGWs and PWs would be large, and vice versa. When the tidal amplitudes equal 2 K, the forward model shows that the aliasing effects from IGWs and PWs decrease to less than half of the percentages presented above. It should be noted that while the Hamming window applied to the temperature perturbation contour helps reduce the aliasing effects from IGWs, it might slightly reduce the tidal amplitudes. Our test indicates that the tidal amplitudes derived from the

unsmoothed perturbation contour are about 3% and 10% larger than the amplitudes in Figure 2.3 for diurnal and semidiurnal tides, respectively.

As for tidal phases, the Fe region is characterized by downward phase progression in general and thus upward energy propagation. In Figure 2.3, downward phase progressions can be found from 50 to 110 km and 80 to 110 km for the diurnal and semidiurnal tides, respectively. A few outliers of semidiurnal tidal phases around 90 km are likely due to the small tidal amplitudes at the corresponding altitudes shown in Figure 2.3. The vertical wavelength estimated from the phase line is 29.0 km between 50 and 100 km for diurnal tides and 23.0 km between 80 and 110 km for semidiurnal tides (red dashed lines in Figure 2.3). The reason that 100–110 km is excluded when estimating the vertical wavelength of diurnal tide is because the slope of the diurnal tidal phase line becomes steeper above 100 km. From 100 to 106 km, the phases of the diurnal tide are nearly constant with altitudes (see Figure 2.5b in section 2.3 for detailed phase structures between 100 and 110 km). Applying a linear fit to the phases between 100 and 110 km, the obtained vertical wavelength λ_z is about 116 km. Although such a λ_z obtained from the 10-km range is not reliable, its large value supports the conclusion that the λ_z above 100 km is much longer than that below 100 km. As for the tidal phases in the low Rayleigh region, there is no obvious vertical phase tilting for both diurnal and semidiurnal tides, which indicates long vertical wavelengths.

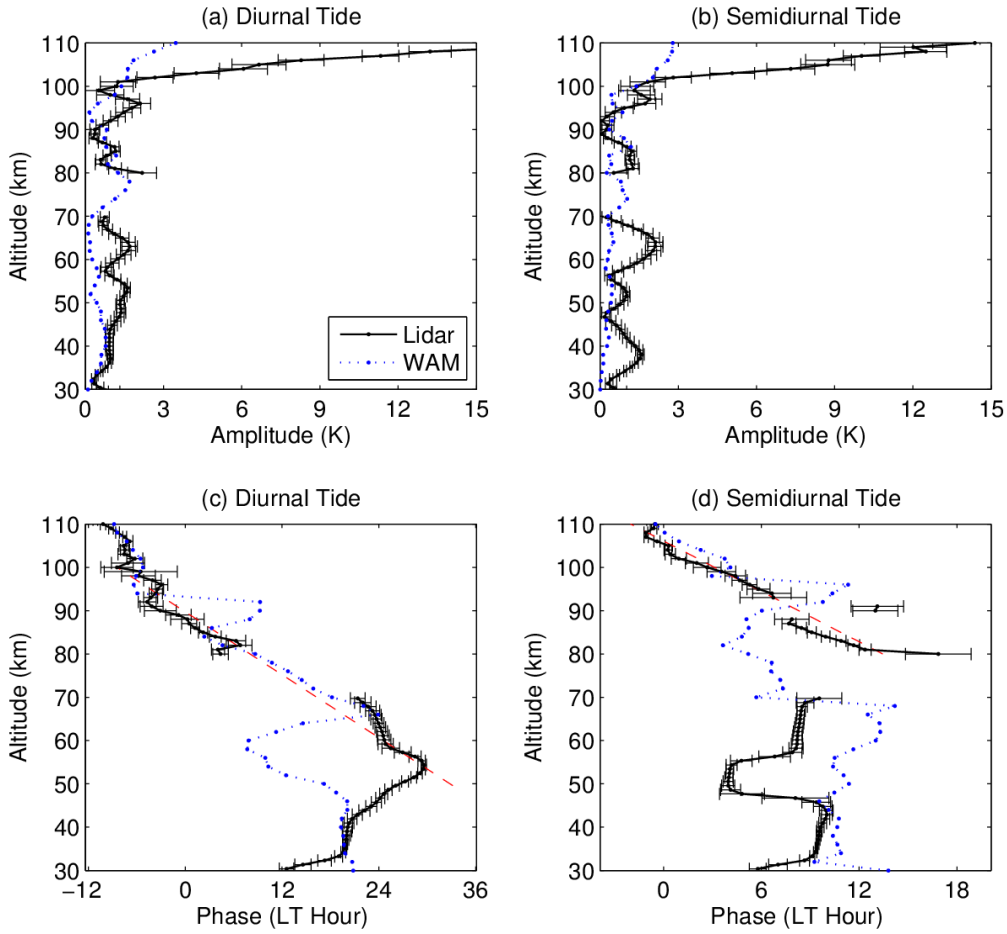

Figure 2.3. Diurnal and semidiurnal tidal amplitudes and phases of lidar observations (black solid lines) and WAM (blue dotted lines) derived from the temperature perturbations in Figures 2.2a and 2.2b. Here phases are defined as the local time of maximum temperature perturbations. The red dashed lines in Figures 2.3c and 2.3d correspond to linear fits of lidar tidal phases from 50 to 100 km and 80 to 110 km for diurnal and semidiurnal tides, respectively.

The fitting uncertainties of lidar tidal amplitudes and phases are plotted as error bars in Figure 2.3. The uncertainties of both diurnal and semidiurnal tidal amplitudes vary between 0.1 and 2 K from 30 to 110 km, while the phase uncertainties vary between 0.2 and 3 h. The method to estimating the fitting uncertainties is briefly described in section 2.7. It can be seen that the tidal phase uncertainties tend to be large when the corresponding tidal amplitudes are small. An illuminative example is the semidiurnal tidal phase uncertainties around 90 km (Figure 2.3d), for which the phase uncertainties are larger than those of the adjacent altitudes.

In order to quantify the overall effects of diurnal and semidiurnal tides on the temperature variations, the lidar temperature perturbation contours are reconstructed from the diurnal and semidiurnal tidal amplitudes and phases derived above and are shown in Figure 2.4a. In general, Figure 2.4a captures the major features of the temperature perturbations illustrated in Figure 2.2a. For example, the warm phase around 11−15 LT and the cold phase around 3−7 LT near 110 km are well reproduced in the reconstruction. The phase pattern in the Rayleigh region is strikingly similar to that in Figure 2.2a. It is understandable that higher frequency features are missing from the tidal reconstruction plot, which account for the differences between Figure 2.2a and the reconstruction plot. In the context of wintertime averages, diurnal and semidiurnal tides together can give rise to temperature perturbations of ~3–4 K in both the Rayleigh and lower Fe (80–100 km) regions in Figure 2.4a. Above 100 km, amplitudes of temperature perturbations increase rapidly and can reach over 20 K. Figure 2.4a reproduces the lidar-observed temperature perturbations reasonably well, indicating that the tidal amplitudes and phases are derived correctly from the winter data.

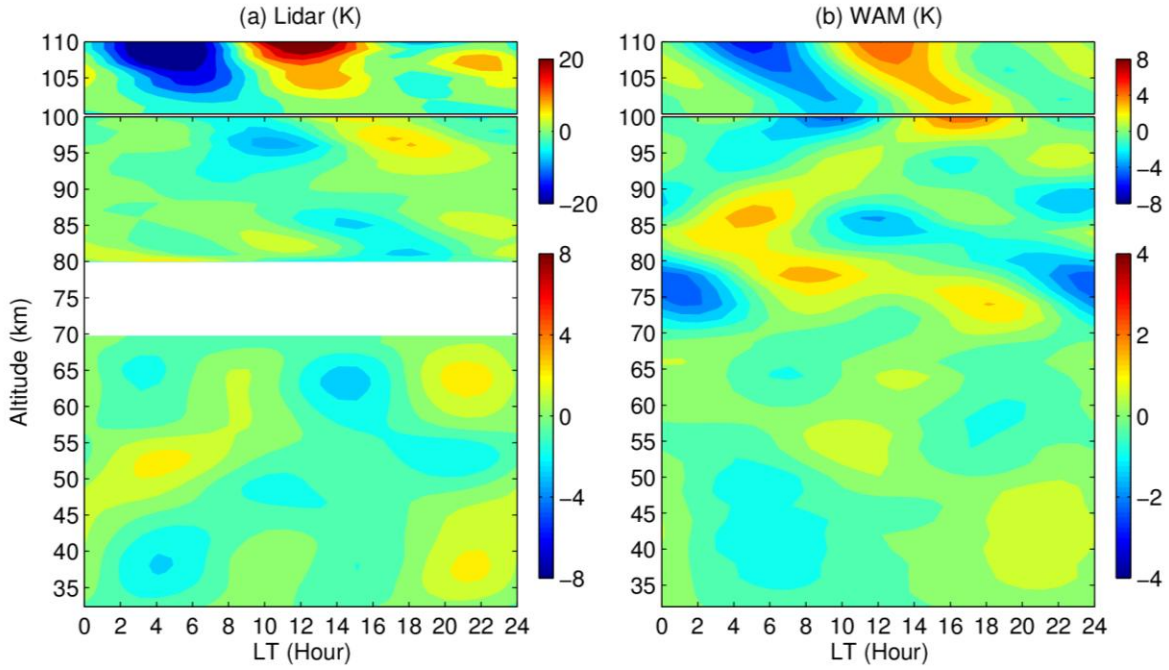

Figure 2.4. Reconstructed (a) lidar and (b) WAM temperature perturbations based on the diurnal and semidiurnal tidal amplitudes and phases in Figure 2.3. The temperatures below and above 100 km are indicated by the bottom and top colorbars, respectively.

2.2.3 Fast Growth of Tidal Amplitude from 100 to 110 km

The rapid increase of tidal amplitudes between 100 and 110 km observed by lidar (Figure 2.3) is intriguing. To quantify the growth rate of tidal amplitudes, we compare the observed scale heights of relative diurnal and semidiurnal tidal amplitudes between 100 and 110 km with that of the freely propagating wave. The scale heights of the tides observed by lidar are calculated by fitting the data with an exponential function defined as:

$$A'(z) = a\exp\left(\frac{z - z_0}{2H_{obs}}\right), \tag{2.2.2}$$

where A' denotes the relative tidal amplitude defined as the absolute tidal amplitude divided by the background temperature, H_{obs} denotes the scale height, and a is the relative amplitude at a

reference altitude z_0. On the other hand, the scale height of the freely propagating wave is equal to the atmospheric density scale height that is given by

$$H = \frac{kT}{Mg}, \tag{2.2.3}$$

where T denotes the mean background temperature observed by lidar, and k, M, and g are the Boltzmann constant, molecular mass, and gravitational acceleration, respectively. The fitted scale heights of lidar diurnal and semidiurnal tides between 100 and 110 km are 2.7 ± 0.1 km and 3.7 ± 0.5 km, respectively, which are smaller than the scale height of the freely propagating wave, 6.1 ± 0.6 km (see Table 2.1 for details). The smaller scale heights from lidar observations lead to faster amplitude increases than the freely propagating wave. Such a situation is demonstrated in Figure 2.5a where the blue solid line is the diurnal tidal amplitude observed by our lidar (the same as shown in Figure 2.3a between 100 and 110 km, and is termed as "all observation group" here) and the green dashed line is an example of the freely propagating wave, which takes lidar diurnal tidal amplitude at 100 km as the reference altitude. The faster growth of the blue curve than the green curve in Figure 2.5 implies that, in addition to the upward propagating tides from the lower atmosphere (< 100 km), there may exist other tidal sources either *in situ* or above this region.

From the above results, we characterize the increase of the tidal amplitudes above 100 km observed by lidar as "fast growth" because the growth rates of the tidal amplitudes exceed that of a freely propagating wave. We believe that the observations above 100 km are realistic since the estimated uncertainties are not large between 100 and 110 km (~1–2 K), and the aliasing effects from IGWs are also trivial compared with the increased tidal amplitudes in this altitude range.

Table 2.1. Scale height and rate of increase of diurnal tidal amplitudes between 100 and 110 km.

	Scale height [a] (km)	Rate of increase [b] (K/km)
	Lidar Observations	
All observations	2.7 ± 0.1	1.8 ± 0.3
Kp ≤ 1	3.0 ± 0.3 (4.0 ± 0.5) [c]	1.1 ± 0.3 (0.9 ± 0.2) [c]
Kp ≥ 2	2.4 ± 0.1	2.8 ± 0.3
Freely propagating waves	6.1 ± 0.6 [d]	0.35 ± 0.02 [e]
	WAM model	
Winter	8.0 ± 1.0	0.20 ± 0.05
Summer [f]	5.9 ± 0.4	0.48 ± 0.06

[a] Scale height is defined in equation (2.2.2).
[b] Rate of increase is defined by a linear fit to the tidal amplitude between 100 and 110 km.
[c] The values quoted in the parentheses are derived in the altitude range of 100−109 km, while the numbers outside the parentheses are for the altitude range of 100−110 km.
[d] The scale height of a freely-propagating wave is calculated as equation (2.2.3) using the background temperature measured by lidar. The calculation is repeated for every 1 km between 100 and 110 km. The mean and standard deviation of the results are quoted here.
[e] The rate of increase is obtained from a linear fitting to the freely propagating tide shown in Figure 2.5.
[f] The altitude range for WAM summer data is from 90 to 110 km.

Several theoretical and model studies show that thermal tides at high latitudes are dominated by the interference of upward propagating tides with tides excited by *in situ* solar forcing and those by the auroral momentum and energy inputs [*Fuller-Rowell et al.*, 1991; *Fesen et al.*, 1993]. Given that McMurdo is located at such a high geomagnetic latitude (~80°S), we investigate the possible link between geomagnetic activity and temperature tides by separating the lidar observations into different groups according to the different Kp indices, i.e., Kp ≤ 1 and Kp ≥ 2 (Figure 2.5). Similar to the "all lidar observation" group, both diurnal tidal amplitudes of Kp ≤ 1 and Kp ≥ 2 groups start to increase above 100 km and the growth rates are also greater than that of the freely propagating wave. We summarize the fitted scale height calculated by equation (2.2.2) and also the rate of amplitude increase by linear fit for each group in Table 2.1. Figure 2.5a and Table 2.1 demonstrate that the growth rates of the diurnal tidal amplitudes

become larger as the level of geomagnetic activity increases. Interestingly, it also shows that the fast growth of tidal amplitude exists even when the geomagnetic activity is minimum (i.e., Kp ≤ 1). It is worth mentioning that the portions of the data devoted into Kp ≤ 1 and Kp ≥ 2 groups are about 51.5% and 41.6%, respectively, of the total 334 hours; also the data of both groups are fairly evenly distributed in the year of 2011 and 2012, thus the effects of inter-annual variability of the tidal amplitudes can be neglected here. The tidal phase lines above 100 km for the three Kp conditions are plotted in Figure 2.5b. As noted earlier, the phase line for "all observations" is nearly vertical or slightly upward from 100 to 106 km and then it becomes downward progression. Interestingly, the phases of Kp ≤ 1 and Kp ≥ 2 have turning points around 106 and 102 km, respectively, where the phases are upward below the turning points but become downward above the points.

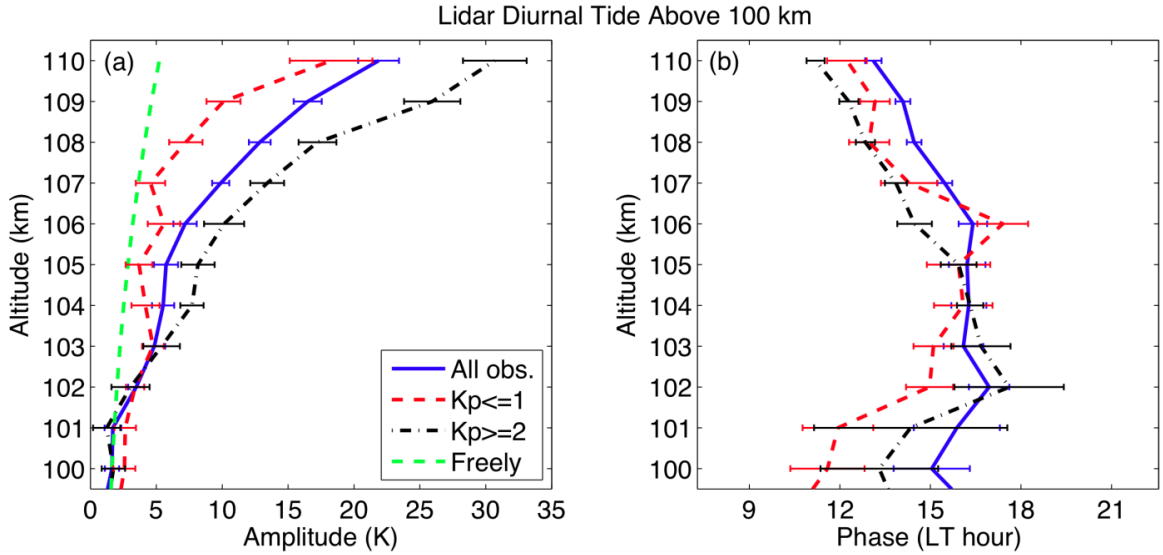

Figure 2.5. Lidar diurnal tidal amplitudes (a) and phases (b) from 100 to 110 km based on the different Kp indices. The freely propagating tidal amplitude is also plotted as a green dashed line in (a) for comparison.

2.3 Comparison with WAM and Dominant Components of Tides

2.3.1 Comparison with WAM-Resolved Tides

The lidar observations are compared with a sophisticated general circulation model, WAM. WAM extends from the surface to about 600 km and is built on an existing operational Global Forecast System (GFS) model [*Akmaev et al.*, 2008; *Fuller-Rowell et al.*, 2008; 2010] to study the dynamical links between the lower and upper atmosphere. WAM is a spectral model and was run at the moderate T62 spectral resolution corresponding to about 1.8º×1.8º in latitude-longitude for the present simulations. The vertical extension of the model domain requires the addition of physical processes operating in the neutral upper atmosphere such as radiative transfer under the breakdown of local thermodynamic equilibrium, heating by solar ultraviolet and extreme-ultraviolet radiation, mutual diffusion of major neutral species, and interaction with the ionosphere through ion drag and Joule heating. The grazing incidence integral [*Rishbeth and Garriott*, 1969] is used to treat the solar heating at very high latitudes when the zenith angle is close to 90º. Tidal forcing by solar radiation at very high latitudes tends to drive quite small tidal wind and temperature amplitudes [*Fesen et al.*, 1993] compared to tides propagating from the lower atmosphere or from geomagnetic activity.

For the study reported here, the model is first initialized and then allowed to run freely for a model year to produce a "free" unconstrained annual run. No variation in external forcing was imposed, but the model has all the natural internal variability expected of a tropospheric weather model. In the region of overlap, a GFS run was used to initialize the model; above the GFS upper boundary at about 62 km, WAM was initialized by empirical temperature and neutral composition fields from the NRLMSISE-00 model [*Picone et al.*, 2002]. After about two months of simulation the specific initial conditions are not apparent. Thus, the simulation results are

considered as model climatology rather than as corresponding to a specific period [*Fuller-Rowell et al.*, 2008; 2010]. The WAM model has also been incorporated into the operational Gridpoint Statistical Interpolation (GSI) data assimilation system, which enables the model to follow the dynamics of specific periods and forecast real weather events, such as sudden stratospheric warmings [*Wang et al.,* 2011; *Fuller-Rowell et al*., 2011].

The WAM simulation used for this study is for a very low level of geomagnetic activity, with the electric field specified by the Weimer electric field model [*Weimer*, 2005] for condition at the Kp = 1 level. This particular WAM simulation has no auroral precipitation. WAM has shown to be capable of resolving atmospheric tides to a great extent [*Akmaev et al.*, 2008; *Akmaev*, 2011]. In our study, four months (May–August) of WAM temperatures from a single-year run with a temporal resolution of 1 h and vertical resolution of 2 km were selected to derive the composite day of temperature perturbations using the same method as lidar data. The Hamming smoothed results are shown in Figure 2.2b.

Similar to Figure 2.2a, tidal signatures are appreciable in Figure 2.2b and there is a certain resemblance of the wave patterns between lidar and WAM. For instance, in both datasets, two warm phases propagate downward from 110 km around 11 and 23 LT to 90 km, and from 30 to 50 km, warm phases are found before midnight (0 LT) and cold phases after that. This agreement is better illustrated in the comparison of the reconstructed temperature perturbations (Figure 2.4). As discussed earlier in section 2.3, Figure 2.4a captures the major features of the smoothed temperature perturbations illustrated in Figure 2.2a. This is also true for the WAM simulations by comparing Figures 2.2b and 2.4b. A noticeable discrepancy between lidar and WAM is found at altitudes of 60–70 km, where several hours of phase shift exist between lidar and WAM. Nevertheless, WAM generally reproduces the observed tidal patterns, especially the phases between 90 and 110 km and between 30 and 50 km.

A closer inspection of Figures 2.4 reveals that the magnitudes of temperature perturbations induced by tides in WAM are approximately half of those in lidar observations at the same altitudes. It should be noted that the total hours used in WAM (2952 h in four months of one year) is about 8.8 times of the total lidar hours (over 330 h), which will suppress the incoherent components more effectively. In order to study whether the smaller temperature perturbations resolved in WAM are due to a larger total sampling or a real underestimation, we randomly selected a continuous period between May and August and obtain temperature perturbations in WAM. For each period, it includes the same number of data points as lidar. It is found that by using the same data hours, WAM temperature perturbations become comparable with lidar below 100 km whereas they are still less than half of the lidar perturbations between 100 and 110 km, no matter what periods are chosen for the comparison. This implies an underestimation of tides by WAM in the altitude range of 100–110 km.

The same harmonic model of equation (2.2.1) is applied to the composite day of WAM temperature perturbations (Figure 2.2b) and the results are also shown in Figure 2.3. The four-month mean tidal amplitudes in WAM are normally less than 2 K below 100 km, in general smaller than the lidar, which are not unexpected as discussed in the last paragraph. An amplitude-increasing trend above 100 km is noticeable, but with an underestimated magnitude and a much slower growth rate (Table 2.1). The lidar diurnal and semidiurnal tidal amplitudes are about 13.2 K and 12.5 K at 108 km, while the values are 2.6 K and 2.8 K for WAM, respectively. The scale height of the amplitude increase in WAM winter is 8.0 ± 1.0 km, which is larger than that of freely propagating wave (6.1 ± 0.6 km) and much larger than lidar observations (2.7 ± 0.1 km). This indicates that the tidal amplitude increases much more slowly in the WAM simulation. However, it is worth mentioning that the amplitude growth rate simulated by WAM in summer (derived in the same way as the winter counterpart except that

months are chosen from November to February) is faster compared to winter. The relative temperature perturbations (defined as absolute temperature perturbations divided by the mean temperature) show considerable amplitude increases at altitudes of 86–118 km for the diurnal tide and 82–100 km for the semidiurnal tide, respectively (Figure 2.6). The scale height of amplitude increase in summer, 5.9 ± 0.4 km, is slightly smaller than that of the freely propagating wave, although it is still larger than that derived from lidar data.

The WAM tidal phases agree with lidar observations above 100 km in general, as shown in Figures 2.3c and 2.3d. The phase agreements between lidar and WAM are also illustrated in the reconstructed tidal perturbations as discussed earlier in this section. It is suggested that WAM captures part of the underlying mechanisms giving rise to tides between 100 and 110 km but the total magnitudes need to somehow be augmented in winter. The consistency between the diurnal tidal phases is also found at altitudes below 100 km except for the ranges of ~85–90 km and ~45–60 km. The consistency for the semidiurnal tide is found below ~48 km and above ~97 km, while between 48 and 70 km, a phase difference of 3.8–7.4 h exists. Overall, WAM reproduces many of the features found in lidar observations.

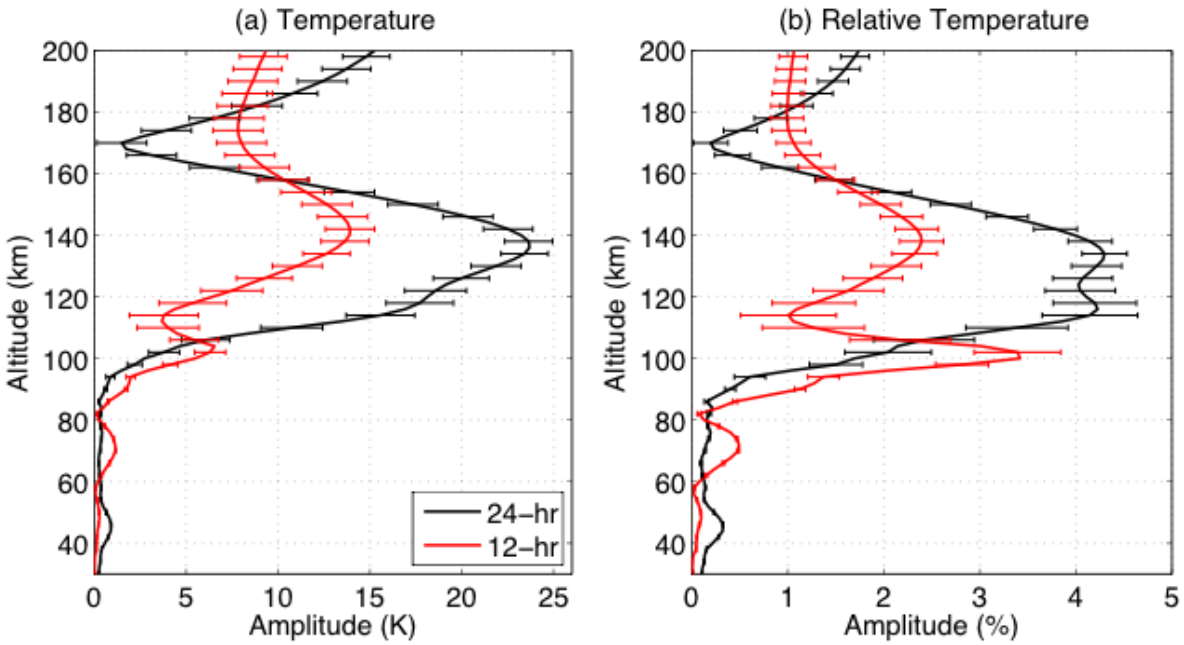

Figure 2.6. Summer mean tidal amplitudes in (a) temperature and (b) relative temperature perturbations from WAM. Black lines are the diurnal tide and red lines are the semidiurnal tide. The error bars are the uncertainties of tidal amplitudes estimated by the same method as lidar data (see the details in section 2.7).

2.3.2 Dominant Components of Tides

It is well known that tides observed from a single station are the superposition of migrating and nonmigrating tides [*Oberheide et al.*, 2006; *Lu et al.*, 2011]. Since WAM simulations show multiple consistencies with lidar observations, we apply WAM to provide a reference on the dominant tidal components at McMurdo. The WAM temperatures at 77.2°S (the closest latitude to McMurdo) are selected to compute the composite day of temperature perturbations at different longitudes. Then a 2D FFT is applied to the composited temperature perturbations as functions of time and longitude, from which the amplitude spectra with respect to wavenumber and frequency are inferred for each altitude.

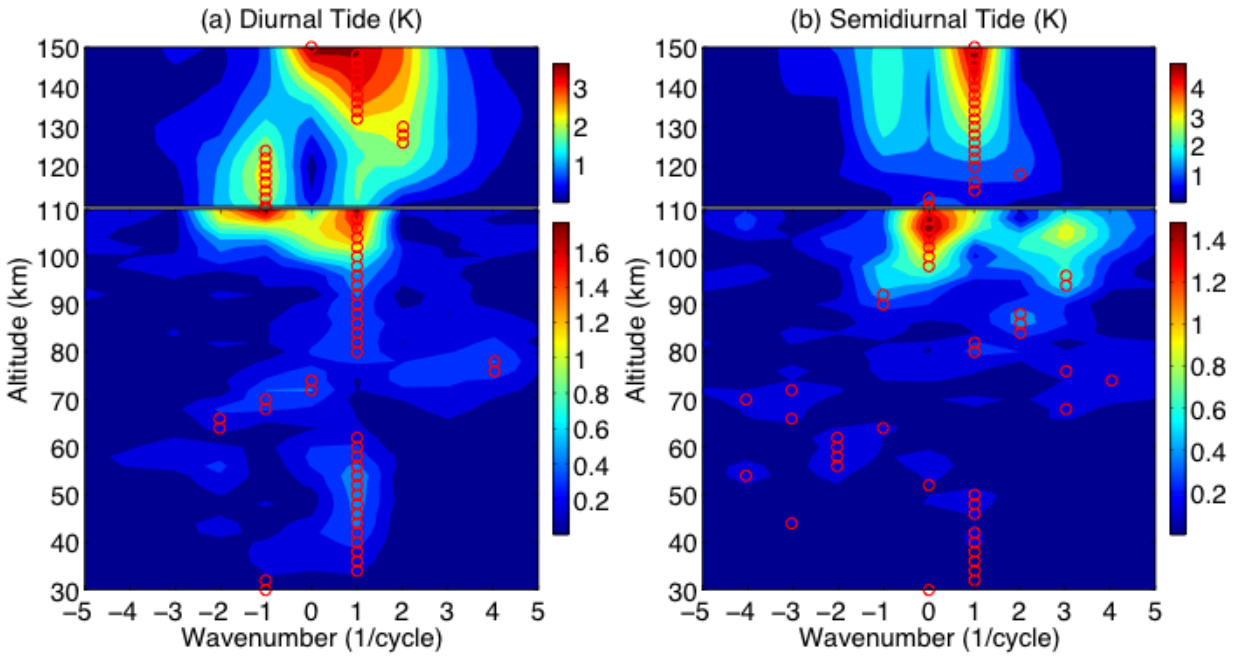

Figure 2.7. Amplitude spectra of (a) diurnal and (b) semidiurnal tides at 77.2°S from WAM. The wavenumbers with the largest amplitudes at each altitude are marked with red circles. Positive wavenumbers correspond to westward propagating tidal components while negative wavenumbers correspond to eastward propagating components. Zero wavenumbers indicate non-propagating tidal components that are zonally symmetric.

Figure 2.7 shows that the dominant component of the diurnal tide in WAM is the DW1 (westward propagating diurnal tide with wavenumber 1) from 30 to 110 km, which suggests that this component is likely to be the dominant diurnal tidal component observed at McMurdo. For the semidiurnal tide, two nonmigrating components S0 and SW3 are stronger than the other components between 90 and 110 km, where the phase of S0 changes approximately from ~7 to 1 LT and that of SW3 changes from ~11 to -1 LT (Figure 2.8). Thus, the vertical wavelengths of S0 and SW3 in this altitude range are estimated to be 40 and 20 km, respectively. Interestingly, the corresponding lidar observations of semidiurnal tidal phase in this altitude range (Figure 2.3d) is close to WAM prediction of the SW3 phases. In addition, the estimated vertical wavelength of ~23.0 km for the semidiurnal tide matches better with that of SW3 (i.e., ~20 km) than S0. Therefore, SW3 is more likely to be the dominant component of the semidiurnal tide

between 90 and 110 km at McMurdo. In the altitude range of 30−45 km, the phases of the semidiurnal tide largely follow those of SW1 (Figures 2.3d and 2.8), which supports the WAM prediction that SW1 is the strongest component in this altitude range. Similarly, based on the temperature observations made by MLS on *UARS* in the winter MLT region at 86 km, *Forbes and Wu* [2006] report that the dominant diurnal component is DW1 from ±60°–70° and the semidiurnal components SW1, SW2, and SW3 have comparable amplitudes with each other at ±60°.

One possible source of the nonmigrating semidiurnal tides (i.e., SW1 and SW3) is the nonlinear interaction of quasi-stationary PW wavenumber 1 and the migrating semidiurnal tide SW2. This mechanism can generate nonmigrating semidiurnal tides in winds in Antarctica and the dominant component is SW1 [*Forbes et al.*, 1995; *Baumgaertner et al.*, 2006; *Murphy et al.*, 2006]. Nevertheless, the WAM simulation shows that the SW2 component in temperature is very weak at McMurdo. Thus, according to WAM, the local nonlinear interaction of SW2 and PWs is unlikely to be the mechanism generating SW1 and SW3. It does not exclude, however, the possibility that SW1 and SW3 are generated by the nonlinear interaction elsewhere and then propagate to McMurdo [*Angelats i Coll and Forbes*, 2002; *Yamashita et al.*, 2002; *Baumgaertner et al.*, 2006].

A key difference between the diurnal and semidiurnal tides in Figure 2.7 is that the migrating component DW1 dominates the diurnal tide more uniformly with altitude, while multiple nonmigrating components of the semidiurnal tide such as SW1, SW3, SE1 and SE2 dominate at different altitude ranges below 90 km. The scattered dominance pattern for the semidiurnal tide and resulting irregular phases between 50 and 90 km shown in both WAM and observations make it difficult to estimate a single vertical wavelength in this region. So this is why we focus on the altitude range of 80–110 km to provide the lidar estimation of the vertical

wavelength for the semidiurnal tide, where the downward phase progression seems obvious and linearly changing with altitude. From the reference provided by WAM that different tidal components could dominate at different altitudes, we know that conducting reasonable simulations of tidal components especially the dominant ones, is key for models to reproduce realistic tides from a single-station observations.

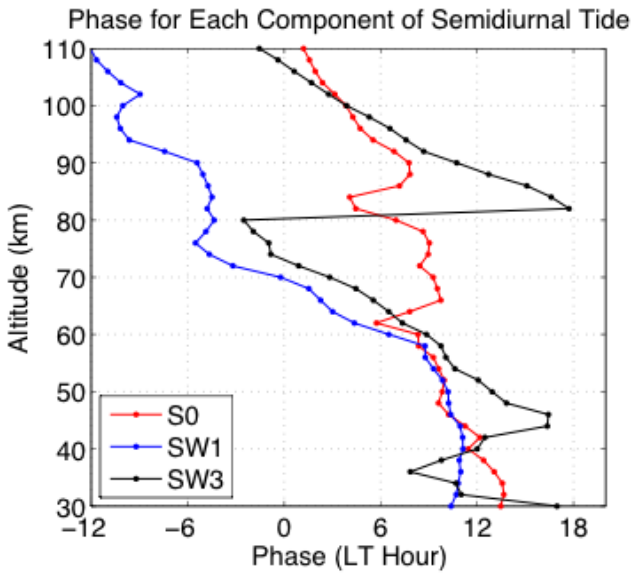

Figure 2.8. Phases for S0, SW1, and SW3 components of the semidiurnal tide from WAM.

2.4 Discussion

Figure 2.5 exhibits super-exponential amplitude increases of the diurnal tides above 100 km. Larger Kp indices appear to correspond to larger tidal amplitudes and faster growth rates from 100 to 110 km. The slopes of tidal phases become steeper above 100 km, and the tidal phases even barely change with altitude from 100 to 106 km, although the phases turn to be downward above 106 km. The significant amplitude increases and phase structure changes imply that there may exist additional tidal sources near or above 100 km. *Avery et al.* [1989] report vertical wavelengths of 20–40 km for wind diurnal tides below 100 km during winter months at Mawson, Antarctica (67°S), which is comparable to our results of ~29 km. In the same time, *Avery et al.* [1989] report that the wind diurnal tides at Mawson show evanescent structure and upward phase progression around 100 km. Similar phase behaviors have also been identified for high-latitude stations in the Northern Hemisphere, such as Poker Flat, Alaska (65°N) and Tromso, Norway (69.5°N). They suggested an *in-situ* forcing centered around 100 km for the diurnal tides at high latitudes, which is supportive of our speculation.

One possible tidal source is the geomagnetic activity as suggested by several model simulations. In the TIGCM simulation by *Fesen et al.* [1991], the diurnal tidal amplitudes of high-latitude temperatures in the lower thermosphere (100–150 km) show increases of 5–15 K with auroral forcings. *Fesen* [1997] shows that from 100 to 110 km, the amplitudes of diurnal temperature tides at 67.5° N increase from ~3 to ~9 K for Kp = 1, from ~6 to ~20 K for Kp = 3, and from ~10 to ~40 K for Kp = 5, respectively. The significant amplitude growth and correspondence of larger tidal amplitudes with higher geomagnetic activity levels are consistent with our observations. This consistency is also seen in the Coupled Thermosphere–Ionosphere–Plasmasphere model (CTIP) simulations [*Müller-Wodarg et al.*, 2001]. From their simulations,

Müller-Wodarg et al. [2001] suggest that: 1) The *in situ* diurnal and semidiurnal oscillations generated at high latitudes by ion-neutral interactions such as ion drag and Joule heating are stronger than the upwards propagating tides; 2) Due to their geomagnetic origin, the *in situ* oscillations strongly depend on Kp index and thus cause an overall dependency with larger Kp index giving rise to stronger diurnal and semidiurnal winds. It is unknown at which altitudes the Joule heating and ion drag associated with geomagnetic activity will act as a tidal source near McMurdo location. Figure 2.5b hints that the case of Kp ≤ 1 has higher altitudes (~100−106 km) for nearly vertical or upward phases than the case of Kp ≥ 2 (~100−102 km). This is consistent with a general understanding that stronger geomagnetic activity has a better chance to penetrate to lower altitudes.

On the other hand, the existences of fast amplitude growths for all Kp index categories including Kp ≤ 1 imply that even though geomagnetic activity may cause an enhancement of temperature tides, other additional contributors are still needed. Two possible candidates could be direct solar heating and chemical heating in the lower thermosphere. Direct solar heating refers to the absorbed solar energy that is converted to heat immediately, while chemical heating is the heat release due to exothermic reactions [*Smith et al.*, 2003]. Whereas direct solar heating occurs only during daylight thus depending on solar zenith angle, chemical heating occurs during both day and night [*Smith et al.*, 2003; *Mlynczak and Solomon*, 1993]. We have examined the duration of sunlight through diurnal cycles from May to August at McMurdo (figure not shown). It is totally dark between 100 and 110 km only for a period of 3–4 weeks (centered at winter solstice). Other than that, direct sunlight exists between 100 and 110 km and lasts for up to ~13 h per day, depending on timing relative to the winter solstice. At 130 km, the totally dark situation is absent and the minimum sunlit period is ~2 h. Due to the existence of solar radiation, the periodic absorption of it can likely generate tides locally and contribute to the observed

amplitude growth. On the other hand, the dominant chemical heating in the upper mesosphere and lower thermosphere is due to the exothermic reaction of $O + O \rightarrow O_2$ [*Smith et al.*, 2003; *Smith*, 2004]. Such an exothermic reaction can occur during both day and night and therefore is not expected to have a pronounced diurnal cycle unless the atomic O distribution is affected by tidal transport and solar radiation. In the MLT region, atmospheric tides can cause temperature, density and wind fluctuations, which can influence the exothermic reaction rate and atomic O density thus the chemical heating rate. According to *Smith et al.* [2003], if the heating is stronger where the tidal temperature tendency is positive, the tide will be amplified; a stronger heating coinciding with a negative tidal temperature tendency will lead to damping of the tide. Depending on the tidal phase, chemical heating could therefore contribute to the observed amplitude growth. Furthermore, there is some evidence that the nonmigrating semidiurnal tides SW1 and SW3 in the Southern Hemisphere propagate from the Northern Hemisphere [e.g., *Angelats i Coll and Forbes*, 2002; *Yamashita et al.*, 2002; *Baumgaertner et al.*, 2006; *Smith et al.*, 2007; *Murphy et al.*, 2009]. Although such propagation is so far limited to the summer tides, other tides might propagate laterally in winter. This could be another contributor to the rapid growth of certain tides in the layer above 100 km.

The observational evidences provided by lidar measurements in the current study may shed a light on some implications and speculations about the tidal sources in the high-latitude lower thermosphere. However, due to the lack of more extensive observations and modeling support, it should be noted that the effects of geomagnetic activity, solar heating and chemical heating on tides need to be better understood and modeled before any conclusions can be reached concerning their roles as tidal sources responsible for the observed fast amplitude growth.

2.5 Conclusions

This paper presents an unprecedented study on the diurnal and semidiurnal thermal tides in temperature from 30 to 110 km in the winter at McMurdo, Antarctica, using two years of the Fe Boltzmann lidar observations. Antarctic winter is a dynamic period with large PWs in the stratosphere [e.g., *Lu et al.*, 2013; *Alexander and Shepherd*, 2010; *Randel*, 1988; *Andrews et al.*, 1987] and extraordinary IGWs in the MLT region [*Chen et al.*, 2013]. These strong waves make it challenging to study thermal tides. Our lidar data show that the mean wintertime amplitudes of diurnal and semidiurnal tides are generally small below 100 km (less than 3 K) and do not increase significantly with altitude. Forward modeling demonstrates that the aliasing effects from PWs and IGWs on tides are less than 0.3 K, and it also shows that the relative effects become smaller when tidal amplitudes become larger. Despite small amplitudes below 100 km, phase structures of tides are reasonable and amplitude errors are small in most altitudes. Therefore, we conclude that the obtained tidal amplitudes are generally above noise levels and the tidal waves are authentic signatures. The vertical wavelength is estimated from the phase line to be 29.0 km between 50 and 100 km for diurnal tides and 23.0 km between 80 and 110 km for semidiurnal tides. WAM compares reasonably well with the observations below 100 km. With a reference provided by WAM, we find that the diurnal tide is likely linked to the DW1 component and the semidiurnal tide is most likely determined by SW3.

A new finding of this study is the fast growth of diurnal and semidiurnal tidal amplitudes above 100 km exceeding that of the freely propagating tides originating from the lower atmosphere. The investigation of the growth rates of tidal amplitudes by calculating the scale heights shows that the lidar-observed scale heights of both diurnal and semidiurnal tidal amplitudes are smaller than that of the freely propagating wave. Such fast growth exists for all Kp index cases and larger Kp indices appear to be corresponding to larger tidal amplitudes and

faster growth rates from 100 to 110 km. The slopes of diurnal tidal phases become steeper above 100 km, and the tidal phases even barely change with altitude from 100 to 106 km.

The fast growth of tidal amplitudes above 100 km observed by lidar is intriguing and novel for high-latitude observations. Although incoherent scatter radar (ISR) observations have shown fast increases associated with geomagnetic activity, most of them have been focused on tidal winds in the Northern Hemisphere and lower latitudes where ISR measurements are available [e.g., *Müller-Wodarg et al.*, 2001]. To our knowledge, the McMurdo lidar observations provide the first report of such a phenomenon in temperature tides in the winter Antarctic region. The significant amplitude increases and phase structure changes suggest the presences of tidal sources above or near 100 km in addition to the upward propagating tides from lower atmosphere. It is noteworthy that since the tidal amplitude uncertainties and aliasing effects from PWs and IGWs are small, the fast amplitude growth observed between 100 and 110 km is a robust feature. The underestimation of the amplitude growth above 100 km by WAM is likely because the model simulation is for a very low level of geomagnetic activity (Kp = 1) and has no auroral precipitation, which if included would considerably enhance the conductivities in the lower thermosphere and hence the Joule heating rates from the imposed electric field. The resultant rather weak geomagnetic forcing in WAM may well explain the weak response of the diurnal and semi-diurnal tides in the lower thermosphere at McMurdo.

The mechanism responsible for the fast amplitude growth of temperature tides in the lower thermosphere is an open question. Whether and how the geomagnetic activity, solar heating and chemical heating would affect the thermal tides at such high southern latitudes (geographic ~77.8°S and geomagnetic ~80°S) are unknown. The quantitative evaluations require more observational data and modeling work. A better characterization and understanding of tides

at high geomagnetic latitudes will help to assess the tidal impacts on space weather and at the same time, hint at the effects of geomagnetic activity on high-latitude thermal tides.

2.6 Appendix 2A: A Forward Model to Assess Aliasing

A forward model adopting the Monte Carlo method is built to see how the large amplitudes and phase incoherence of IGWs and PWs balance out each other by quantifying the aliasing effects of IGWs and PWs on tides. This forward model assumes that the temperature perturbations are mainly contributed from the diurnal and semidiurnal tides as well as from IGWs in the altitude range of 80–110 km and from PWs in the range of 30–70 km, which can be expressed as:

$$\begin{aligned} T'(z,t) = {} & A_{T_{24}} \cos(k_{T_{24}} z + \omega_{T_{24}} t + \phi_{T_{24}}) + A_{T_{12}} \cos(k_{T_{12}} z + \omega_{T_{12}} t + \phi_{T_{12}}) \\ & + A_{IGW} \cos(k_{IGW} z + \omega_{IGW} t + \phi_{IGW}) + A_{SPW} \cos(k_{SPW} z + \omega_{SPW} t + \phi_{SPW}) . \\ & + A_{LPW} \cos(k_{LPW} z + \omega_{LPW} t + \phi_{LPW}) + T_{bias}(z) \end{aligned} \qquad (2.6.1)$$

A, k, ω, and ϕ correspond to amplitude, wavenumber, frequency, and phase, respectively. The subscripts T_{24}, T_{12}, *IGW*, *SPW* and *LPW* correspond to diurnal tidal wave, semidiurnal tidal wave, IGW, short-period PW and long-period PW, respectively. Here, the SPWs have periods less than 5 days that are used to represent the prominent eastward propagating PWs observed by *Lu et al.* [2013] at McMurdo, while the LPWs have periods between 10 and 70 days that represent the quasi-stationary PWs and other long-period PWs in the stratosphere and mesosphere [e.g., *Randel*, 1988; *Andrews et al.*, 1987; *Alexander and Shepherd*, 2010]. A T_{bias} term is also included to account for the possible residual seasonal trend and residual day-to-day variations caused by other waves that are not considered in the first five terms. A program is coded utilizing equation (2.6.1) to repeatedly generate data segments that consist of diurnal and

semidiurnal tidal signals as well as the IGW signal or SPW and LPW signals to simulate the derived temperature perturbation profiles in the Fe and Rayleigh regions, respectively.

To determine the aliasing effect from IGW in the Fe region, we set the amplitudes of SPW and LPW terms to zero but let the parameters associated with IGW term and T_{bias} in equation (2.6.1) be randomly chosen by the program while keeping those associated with tidal terms fixed. The selecting ranges of amplitudes (A_{IGW}), wavelengths (k_{IGW}), and periods (ω_{IGW}) of the IGWs are determined according to the observational paper by *Chen et al.* [2013], and the range of phases (ϕ_{IGW}) is from 0 to 2π. The ranges of randomly chosen parameters and the values of the fixed parameters are summarized in Table 2.2. In addition, we also let the length of data segment, namely the time span *t*, be randomly determined by the program. Since most of the lidar data spans are between 3 and 24 h, we set the range of *t* from 3 to 24 h as well. Similarly, to assess the aliasing effects from SPW and LPW in the Rayleigh region, we set the IGW term to zero but let the parameters of SPW term and T_{bias} in equation (2.6.1) be randomly chosen by the program while keeping those associated with tidal terms fixed. The selecting ranges of SPW parameters are determined according to the observational paper by *Lu et al.* [2013]. Furthermore, the amplitude for the LPW term is determined from an analysis to the Modern Era Retrospective-Analysis for Research and Applications (MERRA) data around McMurdo latitude in the winters of 2011 and 2012 (figures not shown). A fixed period between 10 and 70 days (e.g., 20, 30, 40, 50 and 60 days) is chosen for the LPW term with a fixed initial phase, but we let the data segment time span be randomly determined by the program as done in the IGW case. Different initial phases or periods of the LPW are tried for different runs of the simulation, and the aliasing effects are estimated from the average of these different runs. The parameter ranges for SPW and LPW terms are also summarized in Table 2.2.

By repeating the above data segment generating procedure, the program accumulates certain amount of these segments and generates a composite day of temperature perturbation contour. Similar to the lidar data processing in section 2.2, a Hamming window with a full width of 5 h is also applied to the simulated composite perturbation contour. The number of segments that are needed to generate the composite day is determined when the total hours of these segments equal the total hour of lidar data shown in Figure 2.1 (334 h in the MLT and 337 h in the Rayleigh region). In this case, 23 data segments are accumulated for one composite contour. After the smoothed composite perturbation contour is obtained, the harmonic fitting model (equation (2.2.1)) presented in section 2.2 is then applied to derive the tidal amplitudes and phases at each altitude. In order to quantify the aliasing effects of IGWs and PWs, we compare the means of the diurnal and semidiurnal tidal amplitudes obtained from 300 cases of simulated temperature perturbation contours with the prescribed tidal amplitudes (A_{T24} and A_{T12}). The reason that 300 case runs are chosen for the Monte Carlo method is to ensure that the means of the tidal amplitudes converge to stable values. The forward model results are discussed in section 2.2.

Table 2.2. Ranges/values of parameters in the forward modeling [a]

	Amplitude A (K)	Wavelength $\lambda = 2\pi/k$ (km)	Period $T = 2\pi/\omega$ (hour)	Phase ϕ (radian)
		Randomly chosen parameters		
IGW	10–20	20–40	4–9	0–2π
SPW (< *10 days*)	3–10	60–100	72–120	0–2π
LPW (> *10 days*)	2–4	60–100	240−1680	0–2π
		Prescribed parameters [b]		
D- tide (T_{24})	~1	30	24	0
SD- tide (T_{12})	~1	20	12	0

[a] The range of T_{bias} is from -3 to +3 K and it is randomly selected for each data segment.
[b] The amplitudes of diurnal tide and semidiurnal tide are about 1 K in the MLT (80–100 km) and the Rayleigh region, according to Figure 2.3.

2.7 Appendix 2B: Estimation of Harmonic Fitting Errors

The harmonic fitting model (equation (2.2.1)) can be rewritten as:

$$\hat{T}(t) = M + D_C \cos(\omega t) + D_S \sin(\omega t) + S_C \cos(2\omega t) + S_S \sin(2\omega t), \tag{2.7.1}$$

where $\omega = 2\pi/24$. The relations between diurnal and semidiurnal parameters in equation (2.2.1) and (2.7.1) are:

$$T_O = M \tag{2.7.2}$$

$$A_{24} = \sqrt{D_C^2 + D_S^2} \tag{2.7.3}$$

$$A_{12} = \sqrt{S_C^2 + S_S^2} \tag{2.7.4}$$

$$\Phi_{24} = \omega P_{24} = \tan^{-1}(D_S / D_C) \tag{2.7.5}$$

$$\Phi_{12} = 2\omega P_{12} = \tan^{-1}(S_S / S_C). \tag{2.7.6}$$

Using the least-squares fit approach [*Taylor*, 1997], the fitted parameters are related to the measured temperature values as follows:

$$M = \frac{1}{n}\sum_{i=1}^{n} T(t_i) \tag{2.7.7}$$

$$D_C = \frac{\sum_{i=1}^{n} T(t_i)\cos(\omega t_i)}{\sum_{i=1}^{n} \cos^2(\omega t_i)} \tag{2.7.8}$$

$$D_S = \frac{\sum_{i=1}^{n} T(t_i)\sin(\omega t_i)}{\sum_{i=1}^{n} \sin^2(\omega t_i)} \tag{2.7.9}$$

$$S_C = \frac{\sum_{i=1}^{n} T(t_i)\cos(2\omega t_i)}{\sum_{i=1}^{n} \cos^2(2\omega t_i)} \tag{2.7.10}$$

$$S_S = \frac{\sum_{i=1}^{n} T(t_i)\sin(2\omega t_i)}{\sum_{i=1}^{n} \sin^2(2\omega t_i)}, \tag{2.7.11}$$

where n is the number of independent data points.

The errors in the fitted parameters are assumed to be mutually statistically independent. They are related to ΔT, the deviation of the measured individual temperature T from the tidal model $\hat{T}$ given by equation (2.7.1). That is,

$$\Delta T(t) = T(t) - \hat{T}(t). \tag{B12}$$

Here the deviation ΔT can be introduced by photon noise, gravity and planetary waves (non-tidal waves), and the error in the tidal model (i.e., tidal components other than the diurnal and semidiurnal tides in equation (2.7.1)). Under equal-weight fit and if we assume that the root mean square (RMS) temperature measurement errors are approximately the same regardless the time of day, the RMS errors in the fitted parameters can be derived from equations (2.7.2) to (2.7.11) using the propagation of errors [*Taylor*, 1997]:

$$\sigma_M = \sqrt{\frac{1}{n}} Std(\Delta T) \tag{2.7.13}$$

$$\sigma_{D_C} = \sigma_{D_S} = \sigma_{S_C} = \sigma_{S_S} = \sqrt{\frac{2}{n}} Std(\Delta T) \tag{2.7.14}$$

$$\sigma_{A_{24}} = \sigma_{A_{12}} = \sqrt{\frac{2}{n}} Std(\Delta T) \tag{2.7.15}$$

$$\sigma_{\Phi_{24}} = \sqrt{\frac{2}{n}} \frac{Std(\Delta T)}{A_{24}} \tag{2.7.16}$$

$$\sigma_{\Phi_{12}} = \sqrt{\frac{2}{n}} \frac{Std(\Delta T)}{A_{12}} \tag{2.7.17}$$

$$Std(\Delta \hat{T}) = \sqrt{\frac{5}{n}} Std(\Delta T). \tag{2.7.18}$$

Note that for the tidal fit where we have a temperature sample for every hour, n = 24. The temperature variance $Var(\Delta T) = Std^2(\Delta T)$ can be estimated by computing the variance of the difference between the actual hourly temperature measurements and the fitted harmonic model:

$$\frac{1}{n}\sum_{i=1}^{n}\left[T(t_i) - \hat{T}(t_i)\right]^2 = Var(\Delta T)_{PN} + Var(\Delta T)_W + Var(\Delta \hat{T}) = \left(1 + \frac{5}{n}\right) Var(\Delta T), \tag{2.7.19}$$

where the first term represents photon noise induced variance, the second term represents the variance induced by non-tidal waves like gravity and planetary waves, and the third term is the error in the fitted tidal model. Therefore, the temperature variance can be derived as:

$$Var(\Delta T) = \frac{1}{(1 + 5/n)} \frac{1}{n}\sum_{i=1}^{n}\left[T(t_i) - \hat{T}(t_i)\right]^2 = \frac{1}{29}\sum_{i=1}^{24}\left[T(t_i) - \hat{T}(t_i)\right]^2. \tag{2.7.20}$$

Once $Var(\Delta T)$ is computed using equation (2.7.20), the RMS errors of the fitted parameters can be obtained from equations (2.7.13) to (2.7.17).

2.8 Appendix 2C: Downward Phase Progression of Lidar Diurnal Tides at McMurdo

In Figure 2.3c, both lidar and WAM exhibit vertically-propagating tidal structures in the mesosphere region. Furthermore, diurnal tidal component spectra shown in Figure 2.7a indicate that migrating diurnal tide (DW1) has dominant amplitude in the same region. According to classical tidal theory, DW1 is expected to propagate only equatorward of ±30°, and should be trapped near the levels of excitation poleward of ±30°. However, this is under the assumption that the background mean winds equal to zero. In reality, as shown in Figure 2.9, the zonal mean

winds in the winter hemisphere are strong and eastward propagating below 100 km. If the background mean zonal winds exist, the Doppler shifted frequency of the tide propagating in the opposite direction to the background winds becomes higher than that in an atmosphere at rest and the vertical propagation becomes possible at latitudes greater than 30° [*Ekanayake et al.*, 1997]. Therefore, in this section, we further investigate the diurnal tidal behavior in the polar region using WAM data and study how the background mean zonal winds affect the propagation of the diurnal tides.

The general dynamical equations governing atmospheric motions comprise zonal and meridional momentum conservations, continuity, and thermal energy equations. The full set of the equations can be found in many literatures and textbooks [e.g., *Lindzen*, 1971]. It should be noted that several assumptions have been made in the equations: the gas constant for air is assumed constant, the atmosphere is considered very thin comparing with the Earth's radius, the ellipticity and surface topography of the Earth are ignored, and hydrostatic equilibrium is assumed. Even though these assumptions are made, the governing equations are highly nonlinear and cannot be solved analytically. However, the full set equations can be simplified such that they are linear and inviscid, with mean winds equal to zero [*Holtan*, 1975]. The simplification allows the meridional and vertical dependencies of the tidal fields to be separated. This yields what are referred to as the classical tidal equations. In short, the linearized tidal equation set reduces to an eigenfunction-eigenvalue problem where the eigensolutions (Hough functions) of Laplace's tidal equation describe the horizontal structures of each mode, and the eigenvalues (equivalent depths) fix each mode's vertical structure [*Forbes and Hagan*, 1979]. *Lindzen and Chapman* [1969] gives detailed descriptions of how classical tidal equations can be solved. *Forbes* [1995] also gives great detailed review of the classical solution and its applications in predicting tidal structure.

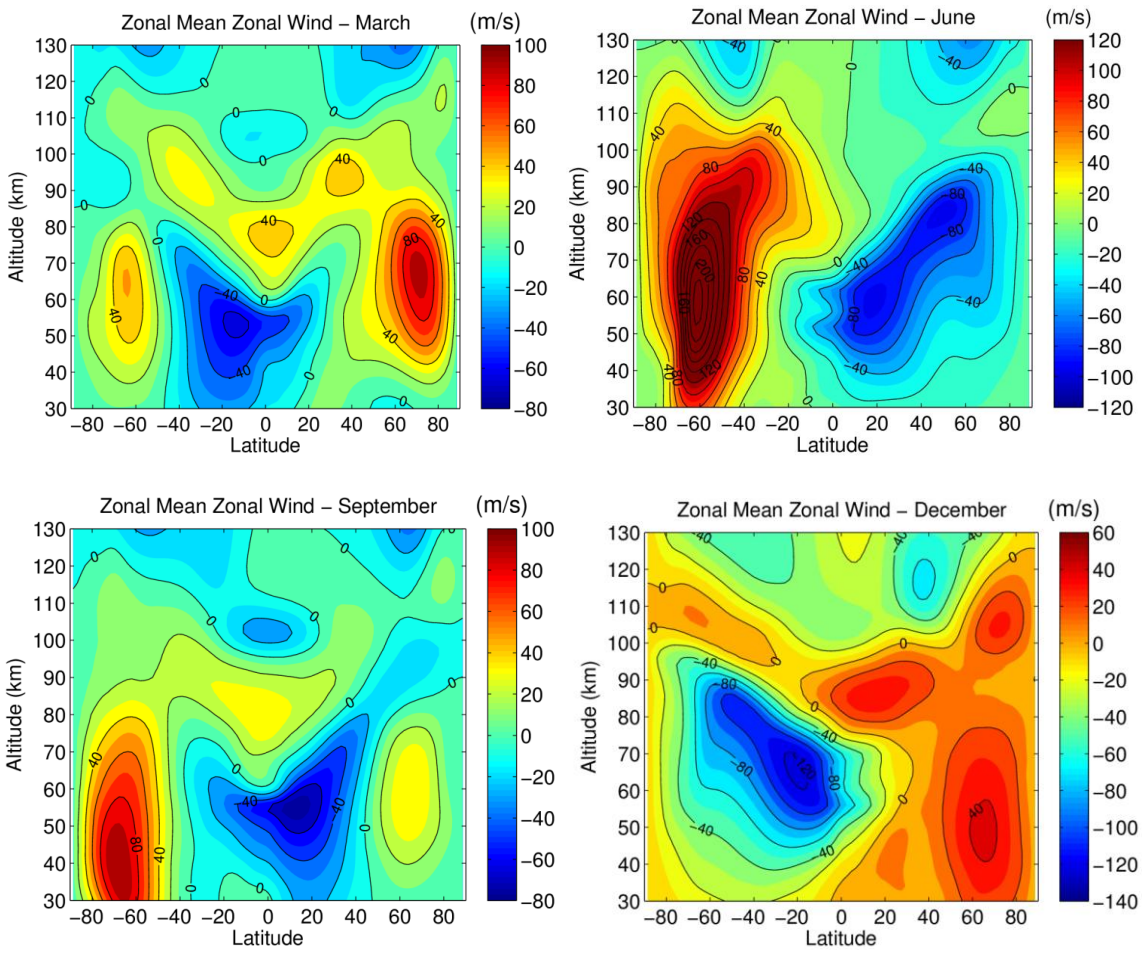

Figure 2.9. WAM output of zonal mean zonal winds in March, June, September, and December. Positive numbers represent eastward velocities.

In the classical tidal theory, the negative equivalent depths correspond to exponentially decaying solutions or trapped waves [*Lindzen and Chapman*, 1969]. By using *f* plane approximation to construct a rotating-plan analog to the spherical equations, we are able to gain further insight into the equivalent depth. The concept of this method is that the vertical structure of tide can be matched by properly choosing the frequency, zonal wavenumber, and meridional wavenumber of an "equivalent" gravity wave [*Lindzen*, 1970; *Murata*, 1972]. For a uniformly rotating spherical viscous atmosphere, *Murata* [1972] showed that the tidal equations are still separable, and the equivalent depth of the internal gravity wave is:

$$gh = \frac{\left(\sigma^2 - f^2\right)}{\left(m^2 + k^2\right)}, \tag{2.8.1}$$

where h is the equivalent depth, g is the gravitational acceleration, σ is the wave frequency, f is the Coriolis rotation rate, and m and k are the wavenumbers in the zonal and meridional direction, respectively. The Coriolis rotation rate $f = 2\omega\cos\theta$, where ω is the rotating frequency of the Earth, and θ is colatitude. Therefore, from equation (2.8.1), the negative equivalent depth of diurnal tides ($\sigma = \omega$) occurs when $\sigma^2 - f^2 < 0$, which correspond to poleward of ±30°. It should be noted that the background mean wind here is assumed zero.

Following *Forbes* [1995], if the none-zero background mean winds are considered in the linearized meridional and zonal momentum equations, it can be shown that the wave frequency σ should be replaced by the Doppler-shifted frequency σ_D and has the relation as follows:

$$\sigma_D = \sigma - \frac{sU}{a\sin\theta}, \tag{2.8.2}$$

where s is the zonal wavenumber, U is background mean wind (eastward > 0), a is the radius of Earth, and θ is colatitude. Here $s > 0$, and σ can be positive or negative, $\sigma > 0$ with eastward propagation and $\sigma < 0$ with westward propagation. We then replace σ in equation (2.8.1) with the Doppler-shifted frequency, and the negative equivalent depth occurs when $\sigma_D^2 - f^2 < 0$. In the winter hemisphere, with the eastward background mean wind, the westward migrating and nonmigrating diurnal tidal components have the relation: $|\sigma_D| > |\sigma|$. Therefore, for example, the vertical propagation of DW1 becomes possible in the regions with latitudes greater than 30°.

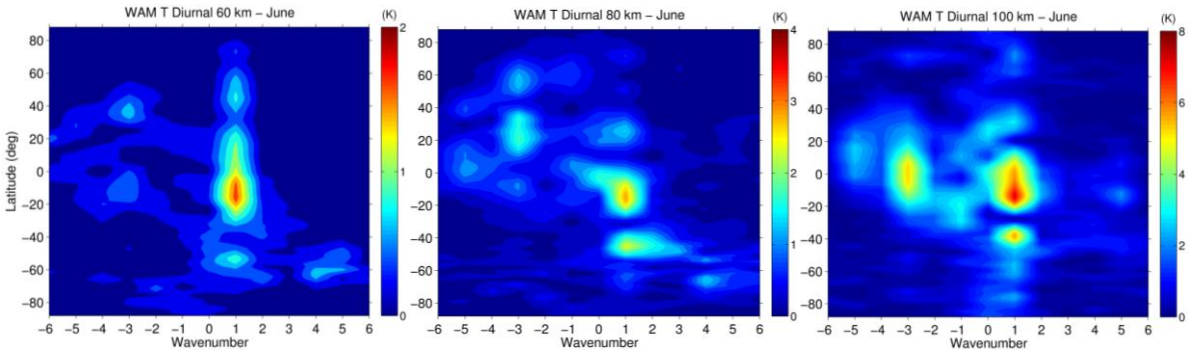

Figure 2.10. Amplitude spectra of monthly diurnal tide in temperature from WAM in June. Positive wavenumbers represent westward propagating component.

To investigate the diurnal tidal behavior in the winter polar region, one year run of WAM temperature outputs are used to extract the components of diurnal tides at different latitudes in order to obtain the global structure of each component. Figure 2.10 shows the diurnal tidal spectra of temperature in June at 60, 80, and 100 km. To obtain the spectra, 2D FFT is applied to the temperature perturbations as functions of time and longitude at each latitude, from which the amplitude spectra with respect to wavenumber and frequency are inferred from each altitude. From the amplitude spectra, DW1 is the dominant component in the mid- and low latitude regions. In the high latitude region, the amplitude of DW1 decreases and the amplitudes of non-migrating components are comparable with DW1.

Figure 2.11 show the altitude-latitude distributions of the amplitude and phase of temperature tides of DW1, DW2, and DW3 in June. Significant amplitudes are seen in the MLT region for each component. Also, the amplitude distributions of all 3 westward propagating components shift toward south hemisphere where the background mean zonal winds are eastward, which are consistent with the prediction of the background mean wind effect just presented earlier. Furthermore, the white lines in Figure 2.11 indicate the position where the Doppler shifted frequency is equal to the Coriolis frequency, and significant tidal amplitudes are

confined in the region where Doppler shifted frequency is greater than Coriolis frequency. The tidal phases also show vertical progression in the same regions.

In summary, although the eastward background mean wind allows DW1 propagates at latitudes greater than 30°, it is still not sufficient for DW1 to propagate in the polar region. Also, the other westward non-migrating components have non-negligible amplitudes between 60 and 100 km as shown in Figure 2.7a. For a single location, the observed temperature perturbations would be the mixture of migrating and non-migrating components. Therefore, it is likely that the cause of the downward phase progression of diurnal tide at McMurdo observed by lidar seen in Figure 2.3c is the result of the mixture of the westward propagating tidal components.

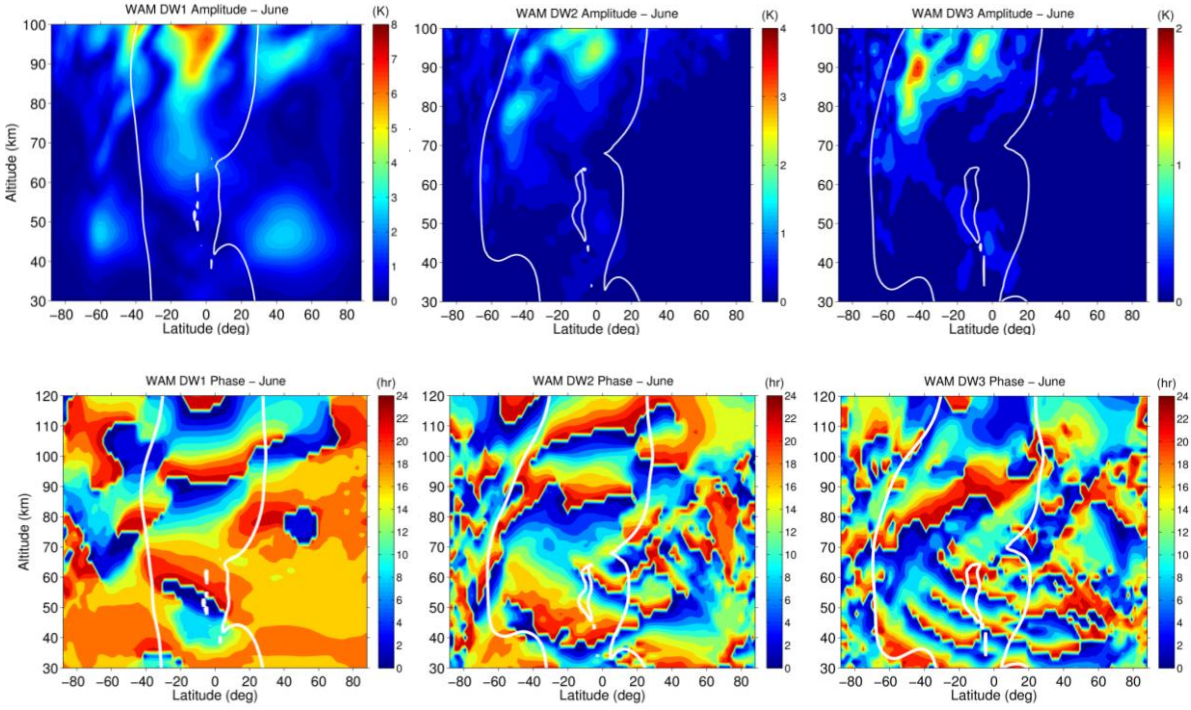

Figure 2.11. (Top row) Amplitudes and (bottom row) phases of DW1, DW2, and DW3 component of temperature tides from WAM. White lines show the position where the Doppler shifted frequency is equal to the Coriolis frequency.

CHAPTER 3

Lidar and CTIPe Model Studies of the Fast Amplitude Growth with Altitude of the Diurnal Temperature 'Tides' in the Antarctic Winter Lower Thermosphere and Dependence on Geomagnetic Activity

3.1 Introduction

Two years of lidar observations at McMurdo (77.8°S, 166.7°E) have revealed a super-exponential amplitude growth with altitude of diurnal temperature tides in the lower thermosphere from 100 to 110 km during Antarctic winters in 2011 and 2012, exceeding that of the freely propagating tides originating from the lower atmosphere (see Figure 5 in *Fong et al.* [2014] or Figure 2.5). Such fast growth exists for all levels of the Kp magnetic-activity index, with larger Kp corresponding to larger tidal amplitudes and faster growth rates with altitude, indicating a connection with geomagnetic activity and the strengths of the magnetospheric sources. The slopes of tidal phases become steeper above 100 km, and the tidal phases barely change with altitude from 100 to 106 km, although the phases turn to be downward above 106 km. Such phase structure changes and Kp dependence suggest additional tidal sources near or above 100 km. Besides solar and chemical heating, the consequences of magnetospheric sources must be considered at polar latitudes.

Numerical simulations have revealed that magnetospheric forcing can enhance thermospheric tides at high latitudes [*Fuller-Rowell et al.*, 1991; *Fesen et al.*, 1993; *Fesen*, 1997; *Müller-Wodarg et al.*, 2001]. The effects of magnetospheric convection can be transferred to the horizontal neutral wind through ion drag [*Zhu et al.*, 2005], causing rotation and

convergence/divergence of the airflow. The convergent/divergent horizontal winds induce vertical winds because of the requirement of mass continuity and result in adiabatic cooling/heating [*Kwak and Richmond*, 2007, 2014]. Joule heating can also induce vertical motion, and the resultant dynamical cooling/heating tends to counteract the Joule-heating-induced temperature changes. The ion drag causes a change of the bulk motion (wind) kinetic energy and has a momentum contribution from both the Pedersen conductivity (Pedersen drag) and from the Hall conductivity (Hall drag). Pedersen drag is perpendicular to the electric field and tends to be rotational; Hall drag is parallel to the electric field so tends to be divergent or convergent [*Richmond*, 1995]. Auroral activity enhances particle precipitation heating via increased energetic particle fluxes. It also enhances Joule heating and both components of ion drag via increased conductivity. All of these mechanisms contribute to the lower thermosphere energetics and cause the change of internal energy (temperature). The magnetospheric sources vary with magnetic local time, in addition to having irregular variations, and contribute to the *in-situ* generation of diurnal tides.

Despite such a general understanding, it is still unknown at which altitudes the different heating mechanisms can act as tidal sources near McMurdo. The enhanced temperature tides indicate a manifestation of ion-neutral coupling and magnetospheric energy dissipation in the lower thermosphere. In this work, we attempt to quantify the relative contributions of the range of potential mechanisms of *in-situ* tidal generation in the lower thermosphere using the Coupled Thermosphere Ionosphere Plasmasphere Electrodynamics (CTIPe) model [*Fuller-Rowell et al.*, 2002]. The main questions to answer include: What mechanisms are responsible for the observed diurnal tide enhancement? How does geomagnetic activity affect the energetics in the lower thermosphere? The model simulations will be compared to the new lidar observations spanning four years from 2011 to 2014 at McMurdo. Concerning the designation of the 24-h component of

the temperature variation as a "tide", we followed the practice of some previous authors (e.g., *Fesen* [1997]) to designate as a "tide" any periodic variation of the atmosphere that is a harmonic of one day, regardless of the source.

This chapter is based on the GRL paper [*Fong et al.*, 2015]. Upon the paper, the detailed lidar data process procedure will be further described in section 2, CTIPe model run and model data process procedure will be discussed in section 3, and the results of the mechanistic study and the conclusions will be given in section 4 and 5, respectively.

3.2 Updated Lidar Observations

McMurdo is located on Ross Island, near the poleward edge of aurora oval. Since the Fe Boltzmann lidar observations at McMurdo started in December 2010 [*Chu et al.*, 2011a,b], four years of temperature data (30–110 km) have been acquired so far. The ~530 h of data collected in the last two winters (2013 and 2014) are more extensive than those in the first two winters (~330 h in 2011 and 2012). We analyze the new datasets to confirm the fast growth findings that were based on the first two winters of data [*Fong et al.*, 2014]. As illustrated in Figures 3.1a and 3.1b, the latter two years of data support the original findings of fast growth in diurnal tidal amplitudes and changing phase structures, but giving somewhat smaller amplitudes than the earlier two years. This is likely due to the smaller average Kp index during the observations as average Kp index is 1.95 and 1.71 for years 2011–12 and 2013–14, respectively, during lidar observations. Figure 3.2 and Figure 3.3 plot the Kp index distributions from May to August for years 2011–14. It could be seen that during 2014, the averaged Kp indices are smaller than those of years 2011–13, in general.

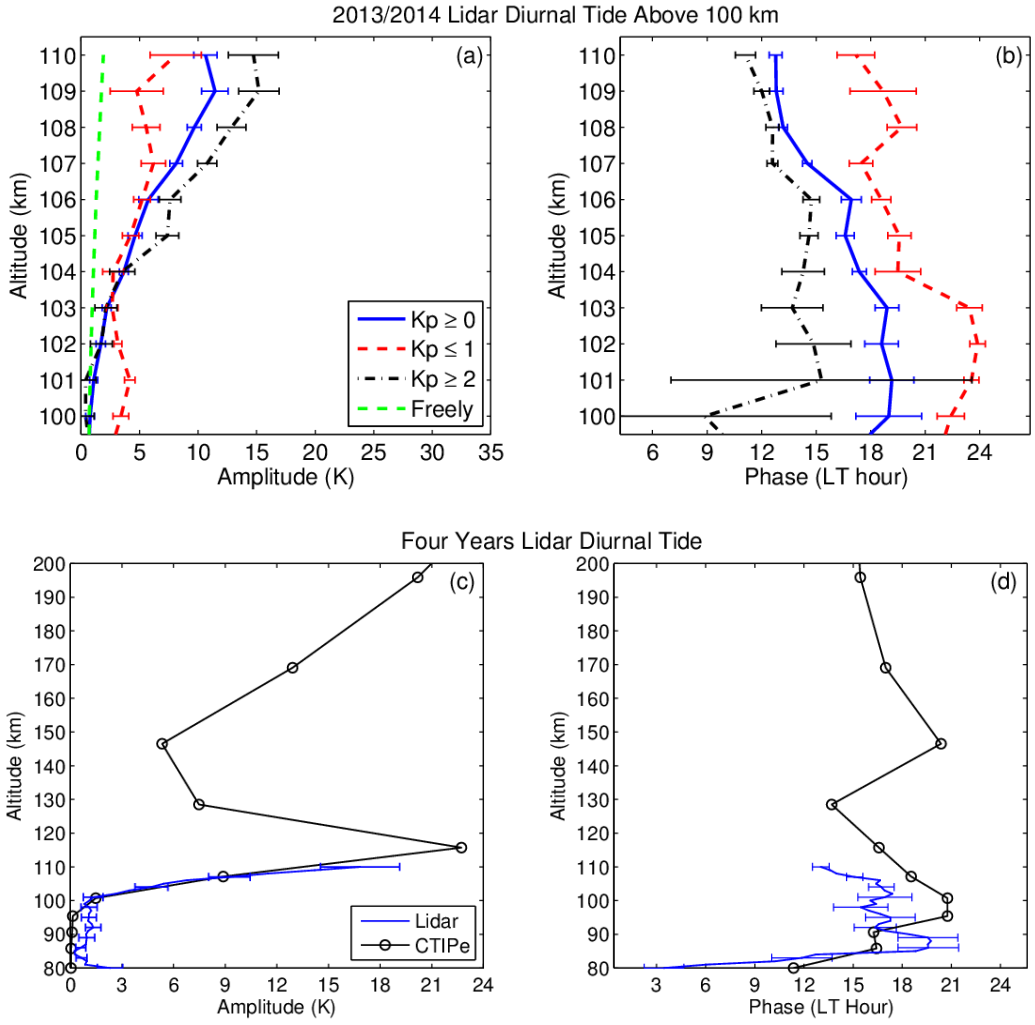

Figure 3.1. Lidar observations of diurnal temperature tides in the MLT region from 100 to 110 km during the winter season (May through August) at McMurdo, Antarctica: (a) The tidal amplitudes and (b) phases from 2013 and 2014 lidar data. (c) The tidal amplitude and (d) phase derived from 4 years of lidar observation (2011–2014) compared with the CTIPe modeled diurnal tidal amplitude and phase near McMurdo derived from the 8-month simulations (May through August in 2011 and 2012).

The detailed lidar data process procedures are summarized as the following:

(1) Select the lidar temperature data from May to August in 2011-2014, including both Rayleigh (30-70 km) and MLT (80-110) region: As described in Chapter 2 (lidar winter tide chapter), the temperature profiles were binned to 1 h and 1 km.

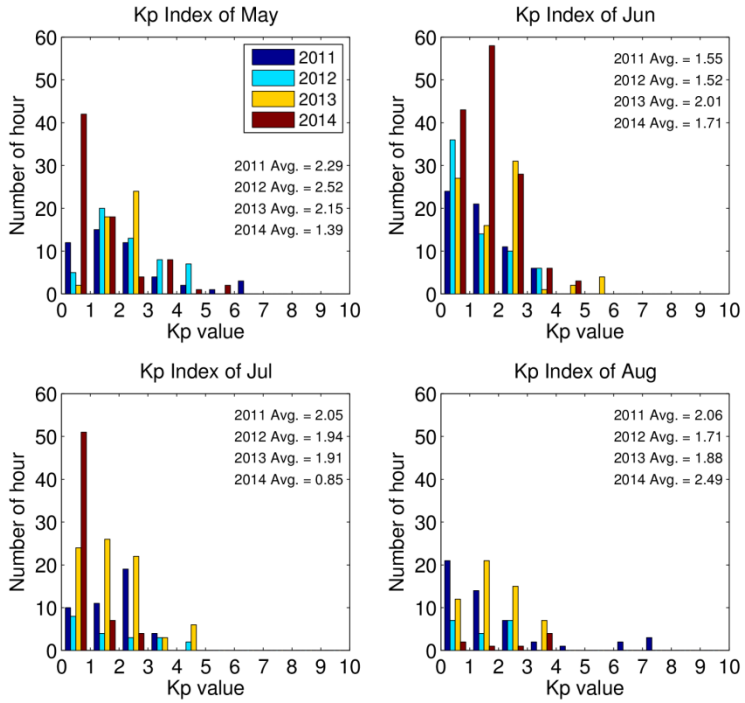

Figure 3.2. Kp index distributions of winter months (May to August) from 2011 to 2014 of lidar observation days only. The four-month lidar observation Kp averages are 1.96, 1.93, 1.98, and 1.46 for 2011, 2012, 2013, and 2014, respectively.

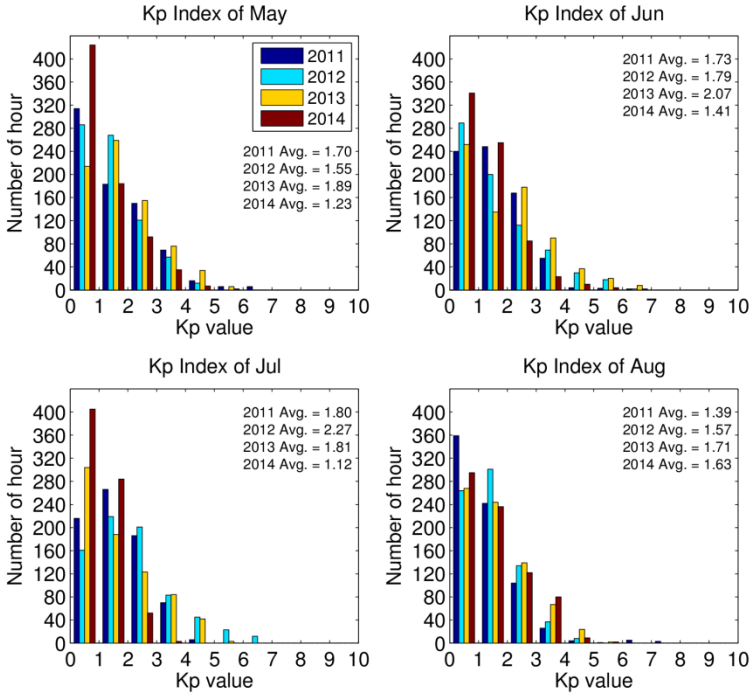

Figure 3.3. Similar with Figure 3.2 but include all the days in each month. The four-month Kp averages are 1.65, 1.80, 1.87, and 1.35 for 2011, 2012, 2013, and 2014, respectively.

(2) Screen and remove unreasonable temperature data: Below 100 km, set data point to NaN if the temperature value is greater than 400 K. Above 100 km, set data to NaN if the temperature value is greater than 500 K.

(3) Select lidar temperature profile based on the Kp index: The daily Kp index data provided by the National Geophysical Data Center has 3-hour temporal resolution (ftp://ftp.ngdc.noaa.gov/STP/GEOMAGNETIC_DATA/INDICES/). Namely, there are 8 Kp measurements every day, which are corresponding to 0-3 UT, 3-6 UT, 6-9 UT, and so on. Since the lidar profiles have temporal resolution of 1 hour, the original 8-point Kp indices are expanded to 24 points. For example, when UT = 4 or 5, the Kp index would be the original 3-6 UT Kp value; when UT = 3, the Kp index would be the mean of 0-3 UT and 3-6 UT Kp values. Depending on the Kp criteria (e.g., $Kp \leq 1$, $Kp \geq 0$, or $Kp \geq 3$), the lidar profiles were selected if the corresponding Kp indices satisfied the criteria.

(4) Construct the winter composite day of temperature perturbations: To form a composite day of temperature perturbations for the winter season, we first derive the composite day of temperature perturbations for each month via subtracting the monthly-mean temperature from the monthly composite for each Kp category. The winter composite day of temperature perturbations are obtained by averaging the all monthly composite days of temperature perturbations.

(5) Smooth the temperature perturbation composite and derive diurnal temperature tides: A Hamming window with a full width of 5 h is applied to the composite in order to suppress the high frequency structures that remain in the temperature perturbations. Then the diurnal tidal amplitudes and phases are derived at each altitude point with the harmonic fitting model shown in Chapter 2 (equation (2.2.1)).

3.3 CTIPe Model Simulations

The CTIPe model is a global, three-dimensional, time-dependent, nonlinear, and self-consistent upper atmosphere model which solves equations of momentum, energy and continuity for neutral particles and ions on an Eulerian co-rotating spherical grid [*Fuller-Rowell et al.*, 2002]. The CTIPe has evolved over the past few decades and currently consists of four distinct components which run concurrently and are fully coupled. The four components are: a global thermosphere model, a high-latitude ionosphere model, a mid- and low-latitude ionosphere/plasmasphere model, and an electrodynamics calculation at mid and low-latitude. The global thermospheric model was developed by *Fuller-Rowell and Rees* [1980] and *Rees et al.* [1980] and the high-latitude ionosphere model were developed by *Quegan et al*. [1982]. These first two components were fully coupled by *Fuller-Rowell et al.* [1987] and are known as the Coupled Thermosphere-Ionosphere Model (CTIM). At this time, the empirical global ionospheric model of *Chiu* [1975] was still used for low latitudes ionosphere. Later on, the model was extended to include the third component, the mid- and low-latitude ionosphere/plasmasphere dynamic model which is based on the model of *Bailey* [1983], by *Millward* [1993]. These three components are described under the name of the Coupled Thermosphere Ionosphere Plasmasphere (CTIP) model by *Millward et al.* [1996]. The electrodynamics calculation was developed by *Richmond and Roble* [1987] and was implemented into the CTIP model by *Millward et al.* [2001], resulting in the creation of the CTIPe model.

The current CTIPe model solves the momentum, energy, and composition equations for the neutral atmosphere with a resolution of 18^{o} in longitude and 2^{o} in latitude, and each longitude slice sweeps through local time with a 1-min time step. For the vertical direction, it uses a pressured-based coordinate system of 15 levels starting from the lower boundary of 1 Pa at 80

km to, depending on the level of solar and magnetic activity, about 500-600 km altitude with resolution of 1 scale height. The CTIPe model requires few external drives: 1) Tidal inputs at the lower boundary, which are based on the results from the global scale wave model (GSWM) [*Hagen et al.*, 1995; 1999]; 2) Solar UV and EUV, which heats, ionizes, and dissociates the atmosphere; 3) Magnetospheric sources at high latitudes, such as the convection electric field which is imposed from Weimer model 2005 [*Weimer*, 1995, 2005] and the auroral precipitation which comes from an empirical model based on TIROS-NOAA series of satellites [*Fuller-Rowell and Evans*, 1987]. Figure 3.4 gives an illustrative diagram of the CTIPe model structure. More detailed description of the CTIPe model can be found in *Fuller-Rowell et al.* [2002] and *Maruyama et al.* [2007].

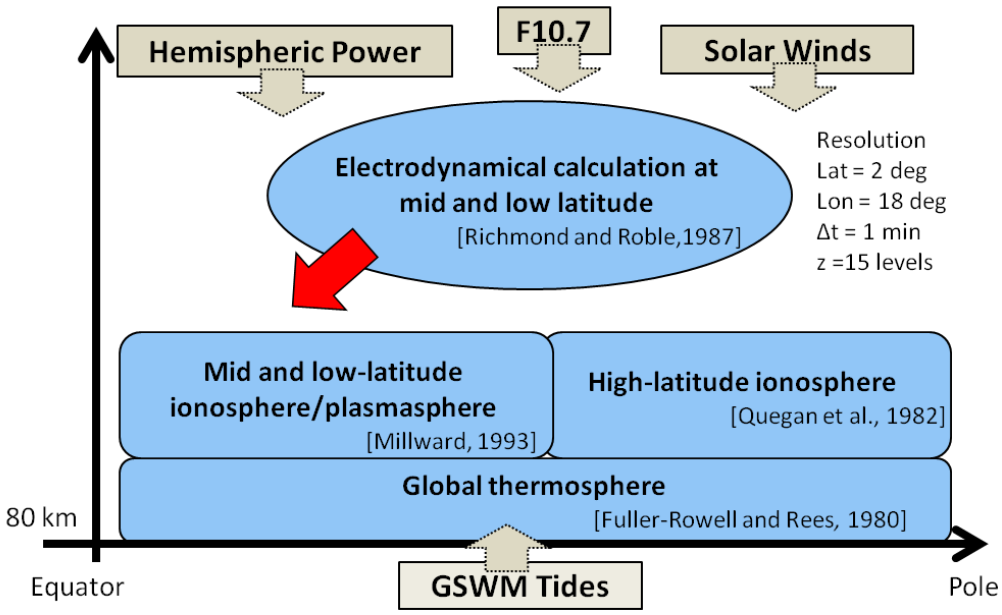

Figure 3.4. Structure of the CTIPe model. The CTIPe model consists of four components (blue) and requires few external parameters to drive the model (gray).

In this study, three different model runs from May to August in 2011 and 2012 were launched. The first one is a real-time run, for which the aforementioned external drivers are fed to the model based on real observations, the second is a run with Hall drag turned off, and the third is a run with the lower boundary tidal inputs from GSWM [*Hagan and Forbes*, 2002, 2003; *Zhang et al.*, 2010a, b] turned off in order to investigate the effects from the lower atmosphere. A diurnal temperature composite is formed with the real-time model run output of two Antarctic winters using the same procedure as described in *Fong et al.* [2014]. The diurnal temperature tides are then derived from the composite with the same harmonic fitting as in *Fong et al.* [2014]. The model results from 80 to 200 km near McMurdo are compared with the 4 years of 80–110 km lidar observations in Figures 3.1c and 3.1d. It is clear that the CTIPe diurnal tidal amplitudes have similar behaviors as the lidar observations from 80 to 110 km, including that of the amplitudes being small below 100 km and increasing rapidly with altitude above 100 km from a few K to over 20 K. The phase structures of CTIPe between 100 and 110 km are also comparable to the lidar observations (difference within 2–5 hours). The good agreement between CTIPe and lidar results enables us to analyze the model results to determine the mechanisms behind the observed fast growth of the diurnal tide at high latitudes.

When such tidal analyses are applied to every model grid point, the resultant diurnal tidal amplitudes in the southern polar plots reveal a concentric ring surrounding the geomagnetic South Pole. Shown in Figure 3.5 is an example of the temperature diurnal tidal amplitudes of the Antarctic region under different Kp conditions at pressure level 7 (~116 km). Note that level 7 corresponds to the altitude of the largest tidal amplitude in Figure 3.1c. Other adjacent levels show similar patterns as level 7 but smaller amplitudes. To minimize the effect of direct solar heating, only June data in 2011 are used to derive tides all over the Antarctic region. We

consider Kp ≥ 3 as disturbed geomagnetic conditions and Kp ≤ 1 as quiet conditions. It is obvious that the tidal amplitudes are larger under the disturbed conditions compared with quiet conditions, consistent with the lidar observations at lower altitudes. The tidal amplitudes form a concentric pattern that encircles the geomagnetic pole (white cross in Figure 3.5). The peak amplitudes averaged along the concentric patterns are about 20.3 K, 29.1 K, and 47.6 K and for Kp ≤ 1, Kp ≥ 0 (i.e., all Kp), and Kp ≥ 3, respectively. The sizes of concentric patterns are similar for all the Kp conditions, and the distance from the geomagnetic pole to the amplitude peak is ~2000 km, corresponding to the geomagnetic latitude of ~72° S. Such concentric rings well overlap the observed auroral zones [http://legacy-www.swpc.noaa.gov/pmap/index.html], which strongly indicates a geomagnetic source of the tidal enhancements that will be studied below.

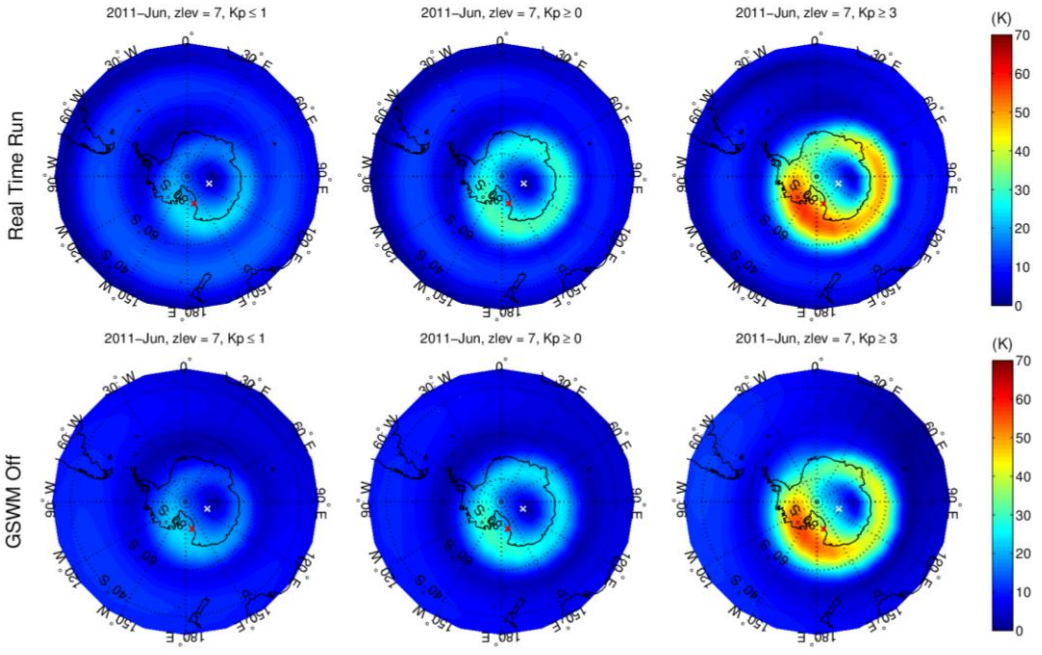

Figure 3.5. Diurnal tidal amplitudes of temperatures from the CTIPe simulations at pressure level 7 (~116 km), under different Kp conditions: Kp ≤ 1 (left), Kp ≥ 0 (middle), and Kp ≥ 3 (right). In the top row are the real-time run cases, and in the bottom row are the cases with lower boundary tidal forcing removed. The location of the south geomagnetic pole is marked with a white cross and that of McMurdo with a red cross.

3.4 Mechanistic Studies

Treating the upper atmosphere as an ideal gas we obtain from the entropy equation (note that the horizontal gradients of temperature and pressure are ignored) the heating rate is:

$$c_P \frac{\partial T}{\partial t} = Q_{diabatic} - \left[c_P w \frac{\partial T}{\partial z} - \frac{w}{\rho} \frac{\partial p}{\partial z} - \frac{1}{\rho} \frac{\partial p}{\partial t} \right], \tag{3.4.1}$$

where T is the temperature, p is the pressure, c_P is the specific heat per unit mass at constant pressure, w is the vertical wind velocity with positive being upward, ρ is density, t is time and z is altitude. The first term on the right hand side is the diabatic heating rate per unit mass due to heat transfer, i.e., all non-adiabatic processes (solar heating, chemical heating, Joule heating, auroral particle heating, vertical heat conduction, and viscous heating, etc.), while the second term (in brackets) represents the adiabatic effects of vertical heat advection and work done to the surroundings of the air parcel in consideration. Appendix 3A gives the derivation of equation (3.4.1). Among the diabatic terms, the Joule heating rate, which has been written out from the CTIPe model, is computed as $Q_{Joule} = \vec{J} \cdot \left(\vec{E} + \vec{V} \times \vec{B} \right) / \rho$, where $\vec{E}$ is the electric field computed from the electric potential provided by the empirical model Weimer-2005 [*Weimer*, 2005], $\vec{J}$ is the current density, $\vec{V}$ is the neutral wind velocity, and $\vec{B}$ is the geomagnetic field. To compute the adiabatic heating rate, we assume hydrostatic equilibrium so that $\partial p / \partial z = -\rho g$, where g is the gravitational acceleration, and take $\partial p / \partial t = 0$; thus, the adiabatic term becomes $\left[c_P w \frac{\partial T}{\partial z} + wg \right]$. Taking the vertical wind, temperature and geopotential height output from CTIPe, the adiabatic heating rate is calculated using this simplified equation.

The diurnal tides induced by each of the above heating terms are then derived as follows. Equation (3.4.2) is fitted to the time series of the heating rate induced by each heating term,

divided by c_p, so that the amplitudes and phases of the diurnal and semidiurnal tides are derived at every model grid point in the southern polar region.

$$\left(\frac{\partial T}{\partial t}\right)_{term} = A_{24}\omega_{24}\sin(\omega_{24}t+\varphi_{24}) + A_{12}\omega_{12}\sin(\omega_{12}t+\varphi_{12}), \quad (3.4.2)$$

where A_{24} and A_{12} are the amplitudes, ω_{24} and ω_{12} are the angular frequencies, and φ_{24} and φ_{12} are the phases of diurnal and semidiurnal tides, respectively, associated with this heating term. Here the heating rate time series is obtained by the same diurnal composite method as used in Figure 3.5.

Plotted in Figure 3.6 are the diurnal temperature tidal amplitudes induced by Joule heating (a–c) and adiabatic heating (d–f) under different Kp conditions at CTIPe pressure level 7. The concentric ring patterns occur in all panels. The tidal amplitudes induced by the total effects of Joule heating and adiabatic heating (g–i) arithmetically averaged between 60°S and 90°S are 23.6 K, 14.5 K, and 11.4 K, for Kp ≥ 3, Kp ≥ 0, and Kp ≤ 1 conditions, respectively. These amplitudes make up about 80% of the corresponding simulated temperature tidal amplitudes (Figure 3.5), which are 29.5 K, 17.5 K, and 19.1 K for Kp ≥ 3, Kp ≥ 0, and Kp ≤ 1 conditions, respectively. The particle precipitation heating makes only minor contributions to the diurnal tides below 120 km, according to the CTIPe simulation results (Figure 3.7): only 1–2 K even under disturbed conditions (Kp ≥ 3), which are significantly smaller than that of the Joule heating or adiabatic heating at the same levels.

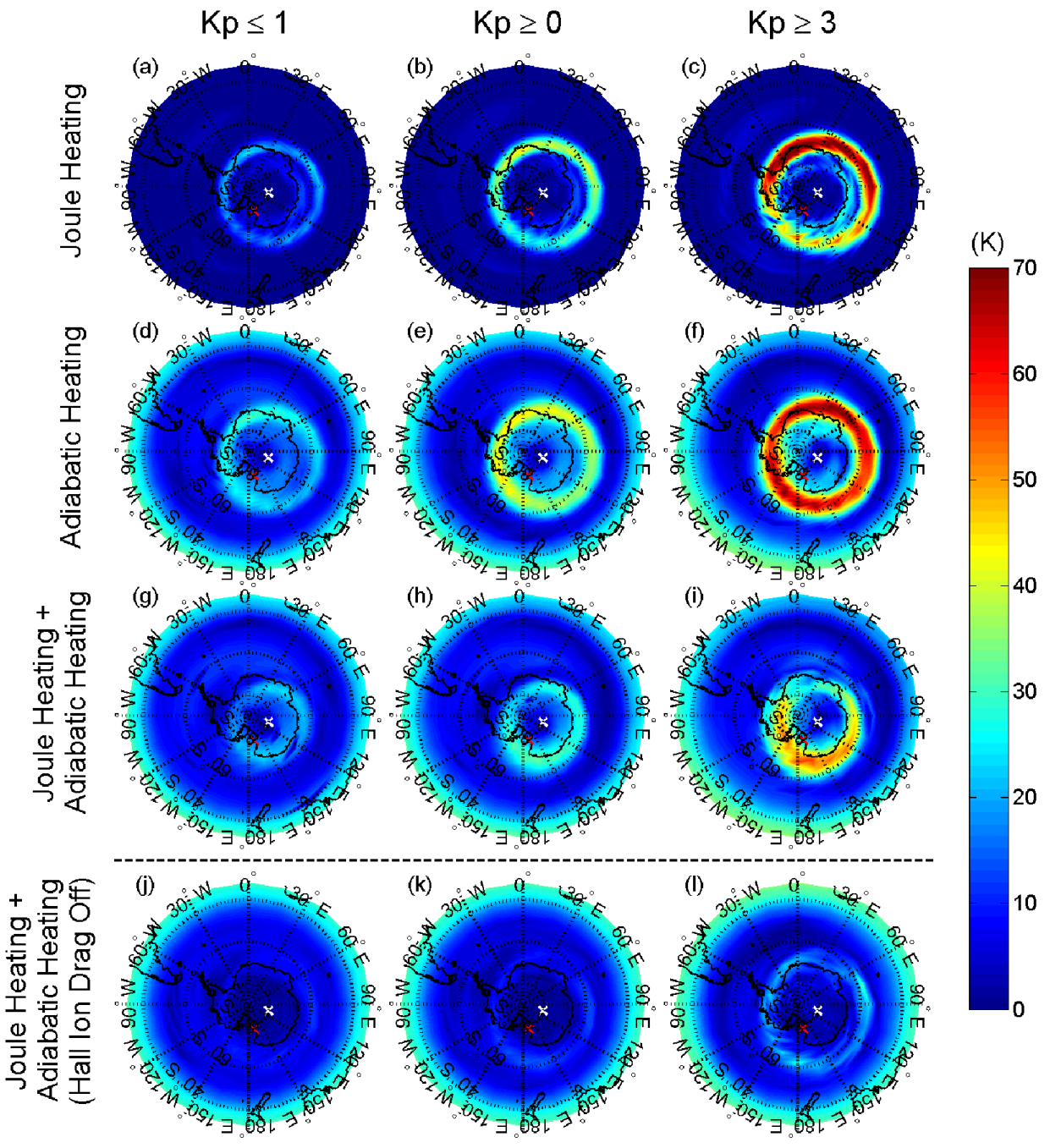

Figure 3.6. Real-time CTIPe model simulations in June 2011 on the diurnal tidal amplitudes of temperatures induced by individual heating terms: (a-c) Joule heating, (d-f) adiabatic heating, and (g-i) the sum of Joule heating and adiabatic heating. (j-l) The diurnal tidal amplitudes of temperatures when the Hall ion drag is removed from the CTIPe model. The simulation results are for CTIPe pressure level 7 (~116 km) under different magnetic-activity indices of Kp ≤ 1, Kp ≥ 0, and Kp ≥ 3 for the left, middle and right columns, respectively.

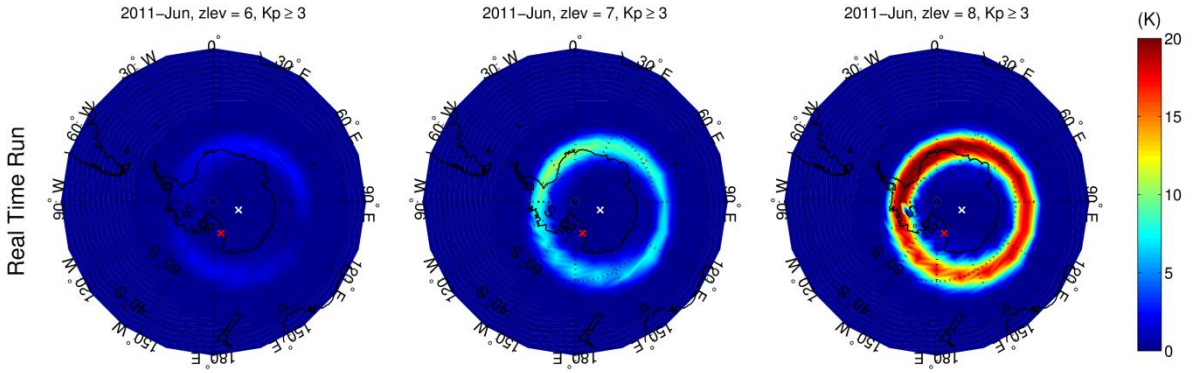

Figure 3.7. Real-time CTIPe model simulations in June 2011 on the diurnal tidal amplitudes of temperatures induced by particle precipitation term (C8) on level 6 (~106 km), level 7 (~116 km), and level 8 (~126 km) under disturbed condition.

As pointed out in *Roble et al.* [1982], both ion-drag-induced convergent/divergent airflow and Joule heating can induce vertical motion, leading to the adiabatic heating/cooling. It is necessary to identify the dominant mechanism between the two. Considering that the Hall ion drag tends to dominate over the Pedersen ion drag below 120 km [*Kwak and Richmond*, 2007], a test run was launched with the Hall ion drag force removed from the momentum equations in the CTIPe model. The results are shown in Figure 3.6j–l and Figure 3.8. Once the Hall ion drag is removed, the patterns of the induced diurnal tidal amplitudes (Figure 3.6j–l) become very small compared with the real-time run (Figure 3.6g–i), demonstrating that the adiabatic effects driven by Joule heating alone tend to cancel the Joule heating effects. This test also indicates that it is the adiabatic effects of the Hall ion drag that dominate the diurnal tidal forcing in Figure 3.6g–i, which would explain the fact that the maximum amplitudes (Figure 3.6g–i) occur at higher latitudes than the Joule heating effects (Figure 3.6a–c). Taking McMurdo as an example, the induced diurnal amplitudes between 100 and 116 km are significantly reduced, by ~80% at 116 km and ~85% at 106 km when compared with the real-time run case (Figure 3.8a). The horizontal winds in the case of the Hall-drag-off run are smaller than those of the real-time run (not shown), and the wind vector differences between the two runs show divergent and

convergent patterns as illustrated in Figure 3.8b, instead of rotational patterns typical for Pedersen drag. Since Hall drag is in the direction of the electric field, the divergent and convergent patterns of the horizontal wind difference indicate the Hall drag dominance over Pedersen drag in the lower thermosphere below 120 km. The Hall drag tends to be offset by a counteracting horizontal pressure-gradient force, so that it tends to produce increased pressure where the electric field is convergent and decreased pressure where the field is divergent. The convergence and divergence of the electric field maximize around the poleward edge of the auroral oval, near the polar cap boundary. Below 120 km the amplitude of relative pressure perturbation grows with height, implying a diurnal variation of the scale height and temperature. Therefore, Hall drag tends to produce a diurnal temperature tide that maximizes around the polar cap boundary instead of at the center of the auroral zone, where Joule heating maximizes. Overall, the relationships between the Joule heating, adiabatic effect, Hall ion drag, and the induced temperature variations could be illustrated as shown in Figure 3.9.

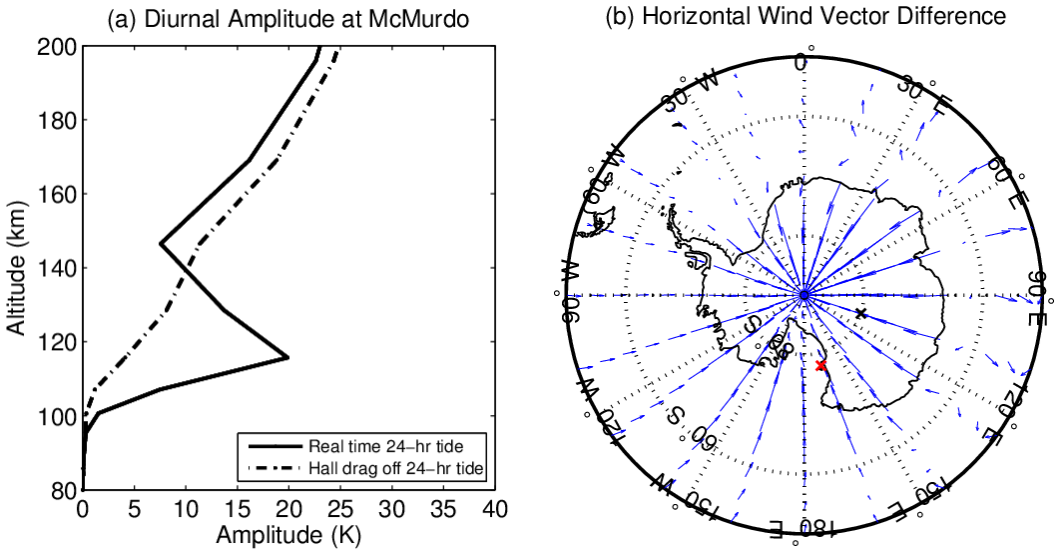

Figure 3.8. (a) Diurnal temperature amplitudes derived from the CTIPe real-time run and the Hall-drag-off run in June 2011. (b) Horizontal wind vector difference between the real-time run and the run without Hall ion drag at 116 km on 5 June 2011 at 6 UT.

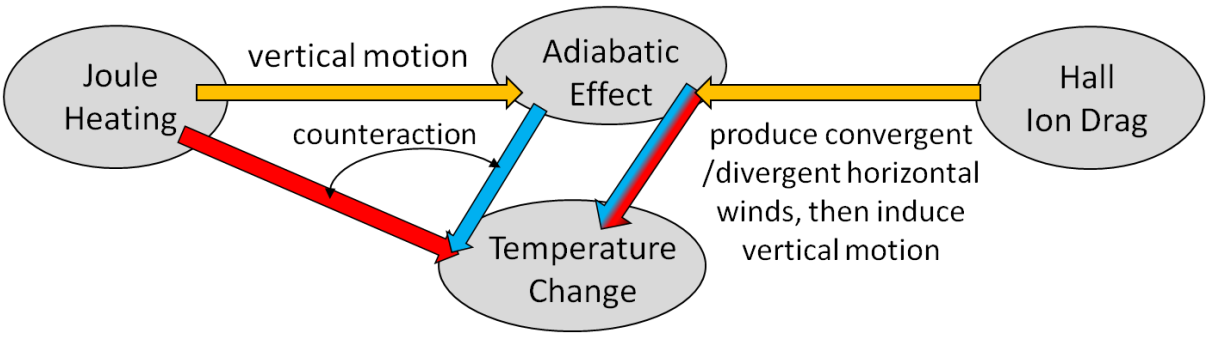

Figure 3.9. Illustrative diagram of the sources of adiabatic heating/cooling and their relations between temperature changes.

The simulation results also demonstrate the Kp dependence of the induced diurnal tidal amplitudes as well as the individual terms of adiabatic, Joule and particle heating. Because the ion drag forcing is larger under more disturbed conditions due to the increased conductivities and electric field, and the Hall-ion-drag-induced adiabatic effect is the dominant source of diurnal tides as shown above, the aurora-enhanced ion drag induces stronger vertical motion thus stronger adiabatic heating/cooling at larger Kp. Again, since the magnetospheric sources vary with magnetic local time, ion-drag-induced adiabatic effects have projections on the diurnal variations, contributing to the *in-situ* generation of diurnal temperature tides and inducing the Kp dependence of the tidal amplitudes. The aurorally driven tides tend to be largest in the generation region, and do not show much, if any, vertical propagation.

The contributions of the tides propagating from the lower atmosphere to the thermospheric tides are small in the polar region but significant in the mid latitudes, according to the CTIPe model run with lower boundary tidal forcing excluded (the bottom row of Figure 3.5). The reduction of the diurnal tidal amplitude at McMurdo is only 0.7 K (relative change ~3.4 %) when compared to the real-time run for the Kp $\geq$ 0 case. It can also be seen that the lower boundary tidal forcing has greater impact (~65%) on the tidal amplitudes equatorward of 60° than on those of the polar regions (~10%), which indicates that the lower-atmosphere tide is a

dominant source in the mid- and low-latitude regions. It should be noted that the GSWM tides used in the CTIPe model do not include all the tidal sources, such as nonlinear interactions between planetary waves and tides [*Zhang et al.*, 2010a, b], and it is known that GSWM may underestimate the tidal amplitudes in the polar region [e.g., *Murphy et al.*, 2006; *Lübken et al.*, 2011].

We also investigate the contributions from direct solar heating, for which CTIPe shows that the induced diurnal amplitudes are less than 3 K poleward of 60°S and below 126 km near winter solstice as shown in Figure 3.10. This is considered a minor effect in this study. Another possible tidal source is chemical heating. Exothermic chemical processes could be enhanced due to particle precipitation, e.g., the dissociative ionization of O_2 could increase the concentration of atomic O and thus enhance the three body reaction of atomic O: $O + O + M \rightarrow O_2 + M$, which is the dominant reaction above 100 km as shown in Figure 3.11 [*Smith et al.*, 2003]. However, according to *Smith et al.* [2003], though the heating rate of this three-body reaction can reach about ~12 K/day around 103 km, it does not have a pronounced diurnal cycle due to the long lifetime of O, which should also lead to a minor contribution to the temperature diurnal amplitude in the lower thermosphere.

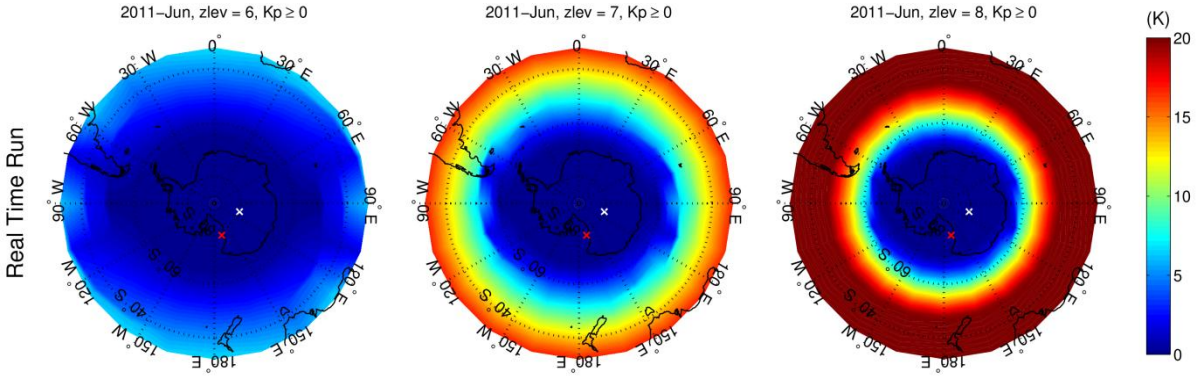

Figure 3.10. Real-time CTIPe model simulations in June 2011 on the diurnal tidal amplitudes of temperatures induced by solar heating term on level 6 (~106 km), level 7 (~116 km), and level 8 (~126 km).

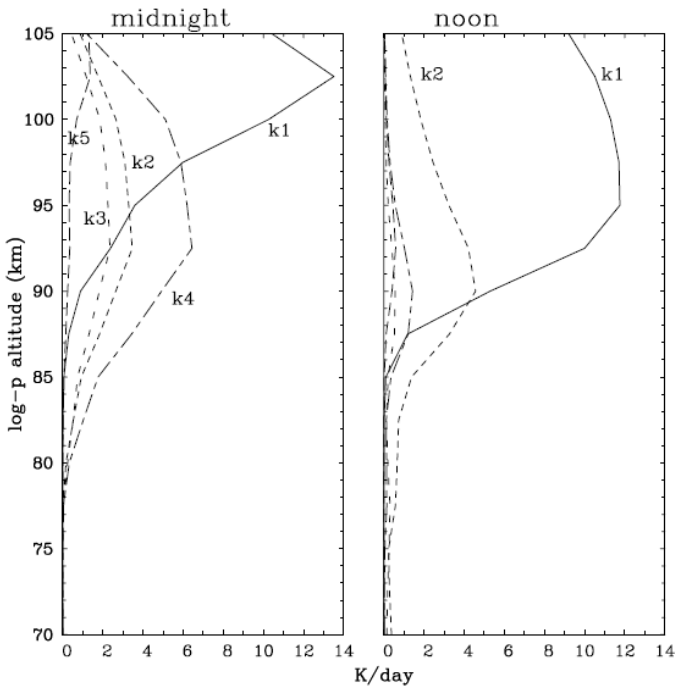

Figure 3.11. Chemical heating rates (K/day) at the equator for the five largest reactions listed in Table 1 of *Smith et al.* [2003]. k_1 is the heating rate of the three body reaction of atomic oxygen: $O + O + M \rightarrow O_2 + M$. Figure is taken from *Smith et al.* [2003].

3.5 Conclusions

After *Fong et al.* [2014] firstly reported the super-exponential increase of the diurnal tidal amplitude in temperature from 100 to 110 km at McMurdo, the lidar observations in the winters of 2013 and 2014 confirm the fast growth with altitude of the diurnal tides and confirm that the tidal amplitudes increase in strength with the Kp index. The winter temperature tides simulated by the CTIPe model are consistent with the 4 years of lidar observations at McMurdo, and the fast growth features are nicely reproduced with clear Kp dependence. From the mechanistic studies using the CTIPe model, we conclude that the Hall-ion-drag-induced adiabatic effects, varying with magnetic local time, are the dominant source responsible for the observed diurnal tides at McMurdo. Although the Joule heating term alone is large, it has a minor contribution to the diurnal tides due to the counteraction by Joule-heating-induced adiabatic effects. CTIPe

simulations predict that such diurnal temperature amplitudes *in-situ* generated by polar ionospheric convection in the lower thermosphere maximize near the polar-cap boundary and form concentric ring patterns that encircle the south geomagnetic pole. Aurora increases the Hall ion drag through increasing conductivities and electric field, leading to stronger vertical motion and adiabatic effects, which explains the Kp dependence of the observed diurnal tidal amplitudes. Other tidal sources, such as particle precipitation, tides propagating from the lower thermosphere, and direct solar heating, are shown to have minor effects on the observed diurnal tides in the lower thermosphere, according to the CTIPe model simulations. Lastly, it is worth to point out that the one-scale-height resolution of CTIPe is not ideal, but it is sufficient to simulate the *in-situ*-forcing-induced local dynamical response and the adiabatic consequences, through the physical processes captured in the model. There is an effort underway to improve the vertical resolution, at which point we expect to confirm the physics of the response, although the amplitudes of the temperature response may change.

3.6 Appendix 3A: Derivation of the Heating Rate Equation

Here we give the derivation of the heating rate equation shown in equation (3.4.1). From the second and the first law of thermodynamics, we have:

$$dS = \frac{dQ}{T} = \frac{dU - dW}{T} = \frac{dU + PdV}{T}, \tag{3.6.1}$$

S is entropy of gas with total mass m, Q is the change of heat, T is temperature, W is work done by the gas, P is pressure, V is total volume and U is the internal energy. For ideal gas, we have $dU = C_V dT$, where C_V is the specific heat under constant volume. Also with $P/T = nR/V$, (3.6.1) can be written as the following:

$$dS = \frac{C_V}{T} dT + nR \frac{dV}{V} \tag{3.6.2}$$

It can be shown that $dP/P + dV/V = dT/T$ and $C_P - C_V = nR$. Replace dV/V in (3.6.2):

$$dS = \frac{C_V}{T} dT + nR \frac{dT}{T} - nR \frac{dP}{P} = \frac{C_P}{T} dT - nR \frac{dP}{P} \ . \tag{3.6.3}$$

Divide (3.6.3) by the total mass *m*, we have

$$\frac{dS}{m} = \frac{C_P/m}{T} dT - \frac{nR}{mP} dP = \frac{dQ/m}{T} \ . \tag{3.6.4}$$

Now, define $s = S/m$, $c_P = C_P/m$, and $\mu = m/n$, where *n* is number of mole. The total time derivative of (3.6.4) could be written as:

$$\frac{ds}{dt} = \frac{c_P}{T} \frac{dT}{dt} - \frac{R}{\mu P} \frac{dP}{dt} = \frac{dQ/dt}{mT} \ . \tag{3.6.5}$$

The total time derivative is given by $\frac{d}{dt} = \frac{\partial}{\partial t} + \vec{v} \cdot \nabla$. And $\frac{R}{\mu P} = \frac{V}{mT} = \frac{1}{\rho T}$, where ρ is density. Therefore, the second equal sign of (3.6.5) becomes:

$$c_P \frac{\partial T}{\partial t} + c_P \left(\vec{v} \cdot \nabla T \right) - \frac{1}{\rho} \frac{dP}{dt} = \frac{dQ/dt}{m} \ , \tag{3.6.6}$$

where *v* is velocity. If we assume $\frac{\partial T}{\partial x} = 0 = \frac{\partial T}{\partial y}$, then (3.6.6) can be reduced to

$$c_P \frac{\partial T}{\partial t} = \frac{dQ/dt}{m} - \left[c_P w \frac{\partial T}{\partial z} - \frac{1}{\rho} \frac{dP}{dt} \right] , \tag{3.6.7}$$

where *w* is the speed in the vertical direction. From the hydrostatic equilibrium assumption, we have: $\partial P = -g\rho\partial z \Rightarrow \frac{\partial P}{\partial z} = -g\rho$. Also, with the assumption of $\frac{\partial P}{\partial x} = 0 = \frac{\partial P}{\partial y}$, (3.6.7) becomes the final form shown in equation (3.4.1):

$$c_P \frac{\partial T}{\partial t} = \frac{dQ/dt}{m} - \left[c_P w \frac{\partial T}{\partial z} - \frac{1}{\rho} \frac{\partial P}{\partial t} - \frac{w}{\rho} \frac{\partial P}{\partial z} \right] . \tag{3.6.8}$$

3.7 Appendix 3B: Lidar Observations of Winter Temperature Tides at McMurdo from 2011 to 2014

In Chapter 2, the lidar observations of temperature tide were derived from the austral winter months of year 2011 and 2012 at McMurdo. In Chapter 3, the mechanism of fast growth of temperature tides with altitude above 100 km was studied by the CTIPe model. In Appendix 3B, the lidar data collected in the winters (May to August) of 2013 and 2014 were processed with the same method as described in Chapter 2, then they are combined with the 2011 and 2012 data, in order to examine if the similar tidal behavior can be observed. Some of the results from 2013–14 were shown in previous sections of this chapter.

Figure 3.12a and Figure 3.13a shows the smoothed lidar temperature perturbations from 2013–14 and 2011–14, respectively. Figure 3.13a shows much clear diurnal tidal structure in the Rayleigh region (30–70 km) and semidiurnal tidal structure in the MLT region (80–100 km) than Figure 3.12a. As discussed in Chapter 2, since Figure 3.13a combines 4 years of lidar data, the contamination from the planter waves in the Rayleigh region and 4 to 9 hour gravity waves can be more effectively suppressed than using only two years of data. Using the harmonic fitting model shown in equation (2.2.1), we derived the diurnal and semidiurnal tidal amplitudes and phases along altitude from Figure 3.12a and Figure 3.13a, which are shown in Figure 3.14 and 3.15, respectively (semidiurnal tides are not shown). In general, similar to the 2011–12 results illustrated in Figure 2.3, lidar observed diurnal tidal amplitudes are less than 3 K from 30 to 100 km, and rapidly increase with altitude above 100 km. However, unlike 2011–12, the diurnal phases for both cases do not exhibit apparent downward phase structures in the MLT region, and both of them seem to have long vertical wavelengths instead.

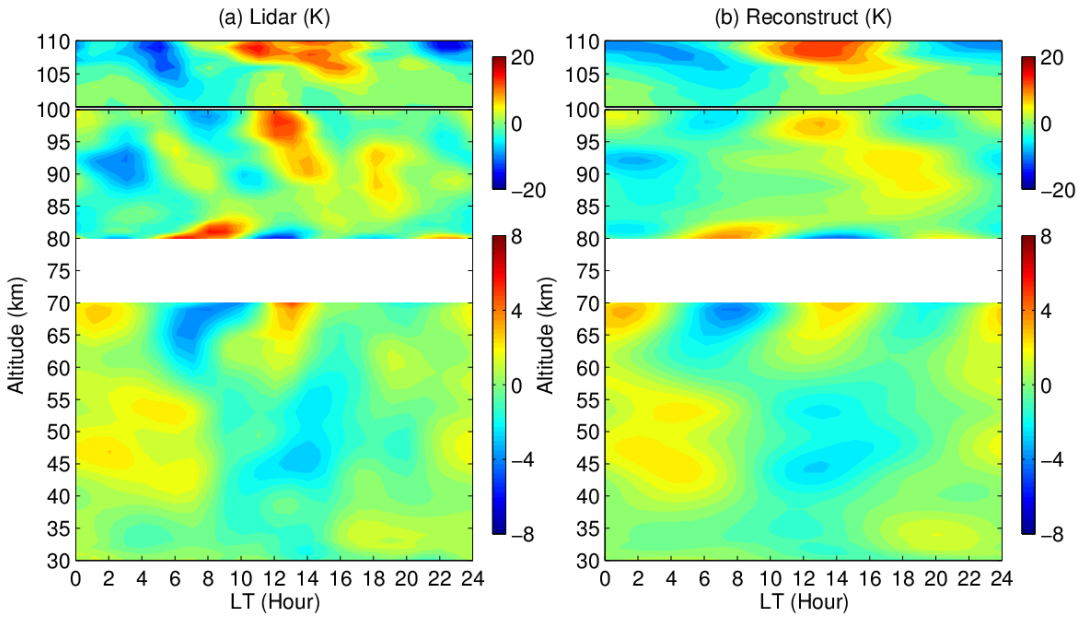

Figure 3.12. Hamming smoothed composite contours of temperature perturbation for a 24-h cycle from: (a) the observations of an Fe Boltzmann temperature lidar at McMurdo (77.8°S) from May to August of 2013 and 2014; and (b) reconstructed lidar temperature perturbations based on the diurnal and semidiurnal tidal amplitudes and phases in Figure 3.14. The temperatures below and above 100 km are indicated by the bottom and top colorbars, respectively.

Further comparing the diurnal tidal amplitudes increasing rates with altitude above 100 km of 2011–12 (Figure 2.3a), 2013–14, and 2011–14 cases, it can be seen that 2011–12 has the fastest amplitude growth rate, then the second one is the 2011–14, and 2013–14 has the slowest growth rate. The tidal amplitude reaches about 21 K, 15 K, and 11 K at 110 km for 2011–12, 2013–14, and 2011–14, respectively. The reason that 2013–14 case has the slowest increase rate is probably due to the relative small average Kp indices in 2014. As shown in Figure 3.2 and Figure 3.3, 2014 has the smallest monthly average Kp indices for most of the months, no matter consider only the mean of lidar observational days or the mean of whole month, comparing with those of 2011 to 2013.

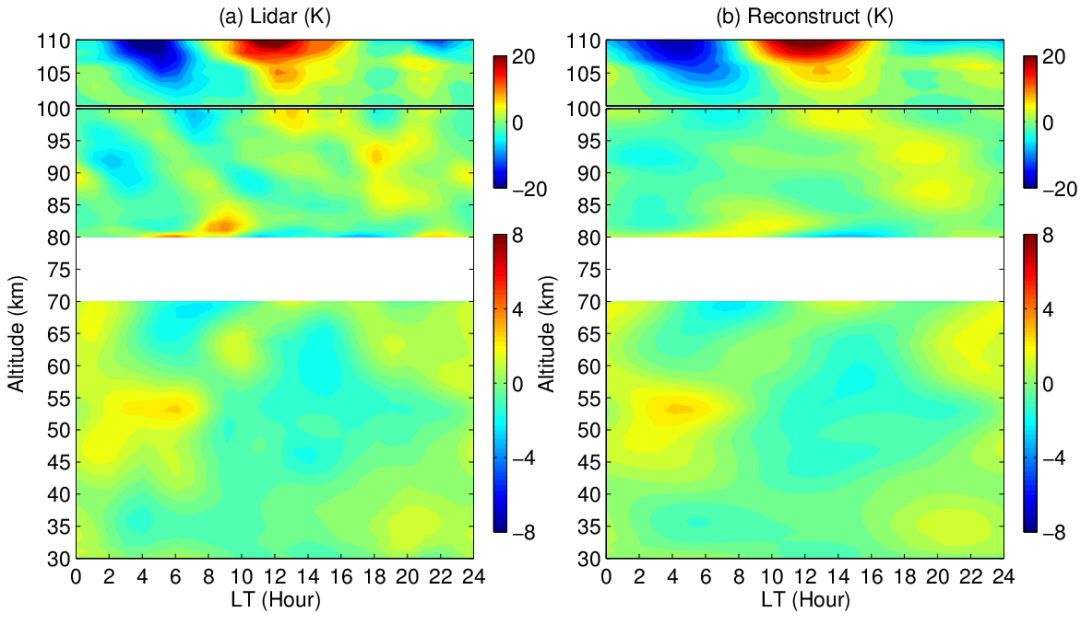

Figure 3.13. Similar to Figure 3.12, but the lidar data is from 2011 to 2014. The temperatures below and above 100 km are indicated by the bottom and top colorbars, respectively.

In order to quantify the overall effects of diurnal and semidiurnal tides on the temperature variations, the lidar temperature perturbation contours are reconstructed from the diurnal and semidiurnal tidal amplitudes and phases derived from 2013–14 and 2011–14 cases. The results are shown in Figures 3.12b and 3.13b. In general, Figures 3.12b and 3.13b captures the major features of the temperature perturbations illustrated in Figures 3.12a and 3.13a, respectively. For example, the warm phase around 11−13 LT and the cold phase around 3−5 LT near 110 km are well reproduced in the reconstruction for both cases. The phase patterns in the Rayleigh regions are also consistent to the original temperature perturbation contours. In the context of wintertime averages, diurnal and semidiurnal tides together give rise to temperature perturbations of ~3–4 K in both the Rayleigh and lower Fe (80–100 km) regions. Above 100 km, amplitudes of temperature perturbations increase rapidly and can reach over 20 K.

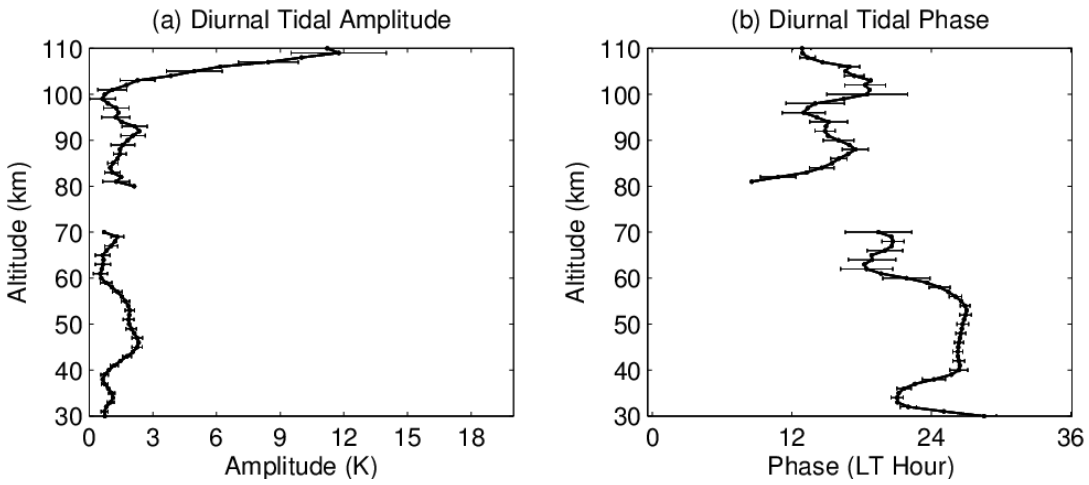

Figure 3.14. Winter diurnal tidal amplitudes and phases of lidar observations derived from the temperature perturbations in Figure 3.12a (2013–2014). Here phases are defined as the local time of maximum temperature perturbations.

Similar to what we have demonstrated in Figure 2.5 and Figure 3.1a-b, we examined the Kp dependence of diurnal tidal amplitudes for 2011–14 case. The lidar data were separated based on the Kp conditions: Kp ≤ 1, Kp ≥ 2, and Kp ≥ 0 (equivalent to all lidar observation), and the diurnal tidal amplitudes were derived by the harmonic fitting model (equation (2.2.1)). As shown in Figure 3.16, as what we should anticipate, the Kp ≥ 2 group has the fastest increase rate of diurnal tidal amplitudes with altitude, the Kp ≤ 1 group has the slowest increase rate, and Kp ≥ 0 group is in between. The tidal phases for Kp ≥ 0 and Kp ≥ 2 groups are similar, the phases change from LT = 21 at 101 km to about LT = 13 at 110 km. However, a phase jump exists for Kp ≤ 1 group between 103 and 108 km, which is probably due to the small tidal amplitudes at the corresponding altitudes.

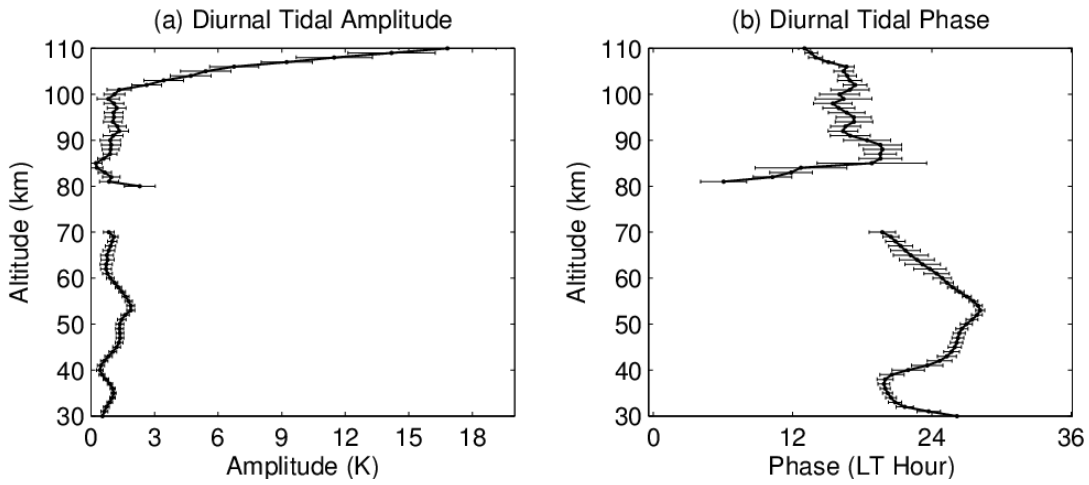

Figure 3.15. Winter diurnal tidal amplitudes and phases of lidar observations derived from the temperature perturbations in Figure 3.13a (2011-2014). Here phases are defined as the local time of maximum temperature perturbations.

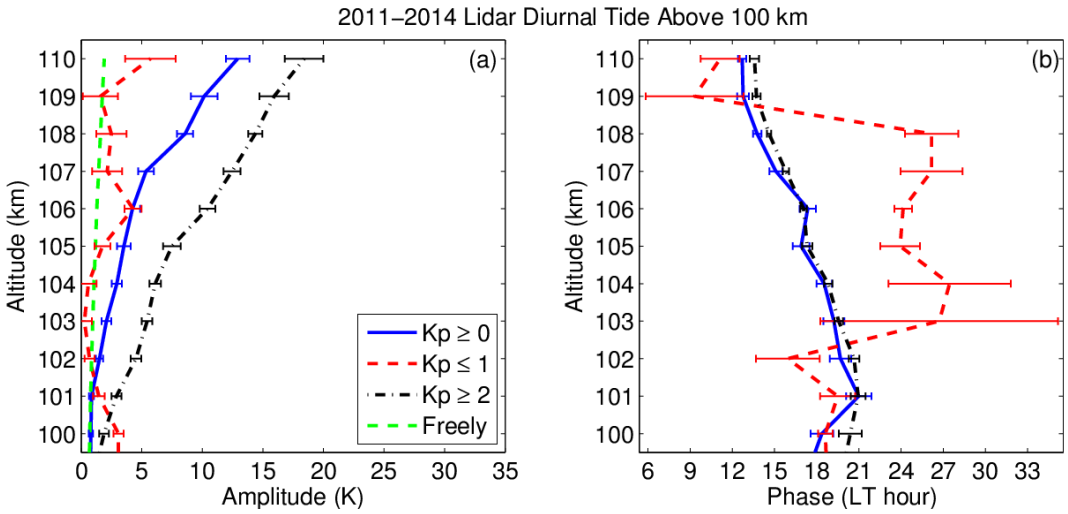

Figure 3.16. Lidar observations of diurnal temperature tides in the MLT region from 100 to 110 km during the winter season (May through August) at McMurdo, Antarctica: (a) The tidal amplitudes and (b) phases from 2011 and 2014 lidar data.

CHAPTER 4

First Climatology of Temperature Structures from 0 to 110 km During 2011-2014 at McMurdo, Antarctica

4.1 Introduction

Temperature is among the most important parameters in atmospheric science studies. In the polar region, temperature plays a dominant role in numerous geophysical phenomena, such as polar mesospheric cloud (PMC), polar stratospheric clouds (PSC), and chemical reactions in the mesosphere and lower thermosphere (MLT) region [e.g., *Chu et al.*, 2006, 2011a; *Collins et al.*, 1993; *Di Liberto et al.*, 2014; *Plane*, 2003; *Plane et al.*, 2015]. Temperature is also a key variable in the study of climate change, which has become one of the most serious and challenging issues in the end of last century and this century. Human beings have been trying numerous approaches to monitor and investigate the ongoing and future impacts to our environment. Studies have shown that the polar middle and upper atmosphere is more sensitive to global climate change than low latitude regions [*IPCC report*, 2001]. Middle and upper atmosphere temperature measurements at polar regions are crucial and an excellent contribution to the monitoring of climate change.

Numerous ground-based and satellites observations have been published and extensive data sets are available in the tropical and temperate zones. However, in the polar region observations of temperature are rare due to the difficult access and the harsh environment for ground-based instruments, and the limited viewing geometries of space-borne instruments. In the Antarctic region, most of the early temperature measurements were obtained by balloonsondes,

which are typically limited to altitudes below ~30 km. There have been lidar observations of mesospheric and stratospheric temperature at the South Pole (90°S), Syowa (69°S, 39.6°E), Davis (69.6°S, 78.0°E), and McMurdo stations [*Pan and Gardner*, 2003; *Kawahara et al.*, 2004; *Klekociuk et al.*, 2003; *Lübken et al.*, 2014; *Di Donfrancesco et al.*, 1996]. It is worth mentioning that some of the datasets were confined to measuring temperature only in the stratosphere due to the principle utilized for temperature derivation, and some of the datasets were sparse or had short observation periods spanning only one to two years. Mesospheric temperature observations made by OH airglow imagers were reported at the South Pole, Mawson (67.6°S, 62.9°E), and Davis [*Hernandez et al.*, 1992; *Hernandez, 2003*; *Greet et al.*, 1994; *Burns et al.*, 2002, 2003]. Also, in situ temperature measurements from 35 to 93 km made by rocket-launched falling spheres during late summer at Rothera were reported by *Lübken et al.* [1999; 2004]. Due to the low signal-to-noise ratio or lack of measurement capabilities during daytime/summertime, some of the Antarctic temperature measurements were limited to night-time/wintertime observations only.

Although several observations of temperature in the mesosphere and the lower thermosphere (MLT) region have been successfully made at the South Pole and near the Antarctic Circle, a significant gap remains in latitude coverage remains between ~69°S and 90°S. Long-duration, large-altitude-range and high-resolution lidar measurements of temperatures can be used to fill this gap. In the austral summer of 2010, University of Colorado (CU) Lidar group deployed an iron (Fe) Boltzmann lidar system at McMurdo. The lidar data is able to provide ground truth measurements for satellite observations and also serve as the baseline for measurements decades from now on to compare with to assess climate changes. This lidar is currently the only on-going resonance fluorescence temperature lidar in Antarctica. The lidar has been operated during almost every clear sky period since the day of installation, and over 5000

hours of data have been collected so far. In this paper, we characterize the temperature structure above McMurdo from 0 to 110 km by combining the lidar measurements with radiosonde data of the lower stratosphere and troposphere obtained from 2011 to 2014. About 4400 hours of lidar data taken in 395 days through 4 years were used. The observed temperature structure and seasonal variations are compared with satellite measurements such as Sounding of the Atmosphere using Broadband Emission Radiometry (SABER) experiment and Microwave Limb Sounder (MLS), and model simulations. We also compare the results with the South Pole lidar observations of *Pan and Gardner* [2003] and other Antarctic stations.

4.2 Observations

4.2.1 McMurdo Campaign and Lidar Observations

The lidar observational campaign at Arrival Heights (77.83°S, 166.67°E), McMurdo on Ross Island has been conducted by the CU lidar group since December 16, 2010. The campaign has been ongoing for over 4 years. The Fe Boltzmann lidar system deployed at McMurdo is capable of temperature measurements during both day and night for full diurnal coverage. The system is comprised of two independent channels measuring absorption lines of 372 nm and 374 nm; meanwhile, each channel works as a Rayleigh lidar individually. Temperatures can be derived from 80–110 km using measurements from both channels by the Fe Boltzmann techniques [*Gelbwachs*, 1994], and from 30–70 km by the Rayleigh integration technique [*Hauchecorne and Chanin*, 1980]. Detailed description of the system design and temperature measurement capabilities can be found in *Chu et al.* [2002]. The gap between 70 and 80 km exists because neither the Fe signal level nor Rayleigh signal is sufficient to derive accurate

temperatures in this region. In this paper, we name the 30−70 km and 80−110 km regions as the Rayleigh region and Fe region, respectively.

The statistics of total lidar observation hours and lidar runs are summarized in Table 4.1. From 2011 to 2014, a total of ~4400 hours of lidar data were collected from the 253 lidar runs. More data were collected during the four summer months (November through February) than in the other months because of greater availability of lidar personnel and better weather conditions. However, although the winter months (May to Aug) have lower average observation hours than the other months, the retrieved temperatures during these four months actually has the highest quality because of the high signal-to-noise level due to the low solar background level (~0 in total dark night). The raw lidar data of photon counts were recorded in resolutions of 1 min and 48 m. In this study, we reduced both the Rayleigh and Fe temperature resolutions to 1 hour and 1 km, which is sufficient for forming temperature climatology. The procedure to retrieve the temperature profiles will be introduced shortly.

Table 4.1. McMurdo lidar observations periods for data used to derive monthly temperature from 2011 to 2014.

	Jan	Feb	Mar	Apr	May	Jun	Jul	Aug	Sep	Oct	Nov	Dec
Year	Hour (Episode [a])											
2011	130 (4)	109 (6)	45 (5)	65 (5)	63 (6)	74 (4)	53 (3)	77 (5)	34 (4)	52 (3)	127 (5)	189 (5)
2012	146 (11)	153 (10)	69 (7)	72 (7)	55 (5)	89 (5)	35 (4)	31 (3)	97 (6)	135 (8)	88 (6)	97 (3)
2013	156 (7)	23 (4)	58 (4)	135 (8)	55 (5)	86 (6)	92 (5)	77 (5)	71 (5)	108 (4)	98 (5)	202 (6)
2014	162 (5)	66 (5)	104 (5)	54 (5)	128 (4)	150 (5)	77 (3)	25 (4)	60 (5)	102 (6)	73 (5)	144 (7)
Total	594 (27)	351 (25)	276 (21)	326 (25)	301 (20)	399 (20)	257 (15)	210 (17)	262 (20)	397 (21)	386 (21)	632 (21)

[a] Episode means the number of lidar run, some lidar runs spanned more than 1 day.

The derivation of Fe temperature is based on the Maxwell-Boltzmann distribution law as shown in equation (5.2.1) [*Chu et al.*, 2002]:

$$\frac{P_{374}}{P_{372}} = \frac{g_2}{g_1}\exp\left(-\Delta E \big/ k_B T\right), \tag{4.2.1}$$

where P is the population of the corresponding state, g is the degeneracy factor, ΔE is the energy difference between the two levels, k_B is the Boltzmann constant, and T is the temperature. The population ratio on the left-hand-side of equation (4.2.1) can be obtained from the lidar measurements, and then temperature can be calculated. The altitude span of the Fe layer determined the altitude range of Fe temperature to be derived. In order to derive robust temperature, the Fe density has to reach a minimum level. During wintertime, the Fe layer usually spans from as low as 75 km to over 110 km, and the Fe layer peak is located around 85 km [*Yu et al.*, 2012]. On some occasions, the Fe layer can extend to over 155 km [*Chu et al.*, 2011b]. The summertime Fe temperature measurements are usually limited by the low Fe densities due to polar mesospheric cloud (PMC) particles and the high-level solar background. The other factor that hinders the temperature measurements in summer is that the very low mesopause temperature (~130 K) significantly decreases the population of Fe atom in the 374 nm state. At 200 K, the ratio P_{374}/P_{372} is about 1/26, but at 130 K, the ratio decrease to about ~1/130. Such a low population ratio further increases the difficulty of obtaining temperature. The uncertainties of the observed Fe temperatures vary depending on the altitude, resolution, and observing month. Typical uncertainties of temperature profiles in winter are less than 1 K in the altitude ranges of 80–100 km (Fe main layer), and between 1–10 K in the range of 100–110 km with 3-hr and 2 km full width hamming smoothing. During March, around local noon, the uncertainties are about 1–10 K in the Fe main layer, and > 10 K above 100 km.

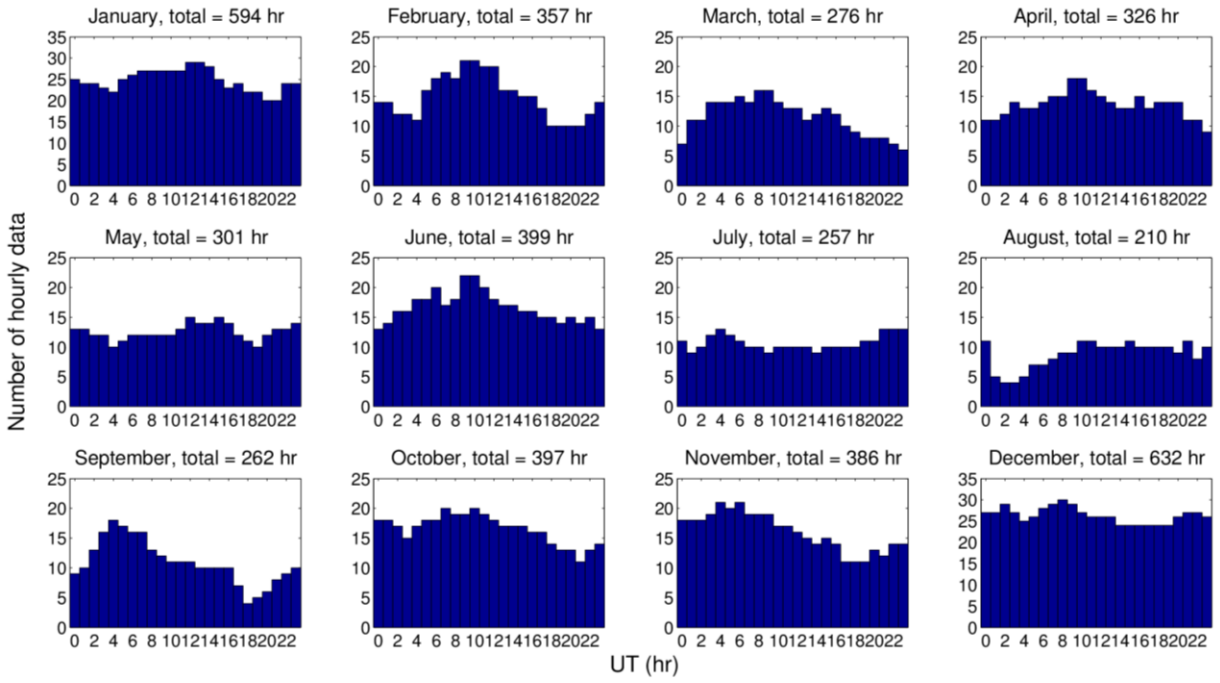

Figure 4.1. Diurnal distribution of hourly lidar data samples from 2011 to 2014. Note that the scales of January and December are different.

Since the Rayleigh lidar signal scattered by molecule in the air is proportional to atmospheric density, the Rayleigh integration technique can deliver temperature profiles from the relative density profile by combining the hydrostatic equation and the ideal gas law. The vertical temperature profile $T(z)$ can be written as [*Hauchecorne and Chanin*, 1980; *Gardner*, 1989]:

$$T(z) = \frac{T(z_0)\rho(z_0)}{\rho(z)} + \frac{M}{R}\int_z^{z_0} g(r)\frac{\rho(r)}{\rho(z)}dr\,, \qquad (4.2.2)$$

where z_0 is the highest altitude of the temperature profile, ρ is atmospheric density, M is the mean molecular mass of the atmosphere, R is the universal constant, g and is the gravitational acceleration. Equation (4.2.2) is calculated downward with a presumed seeding temperature $T(z_0)$. In this study, the seeding temperature is obtained from the Naval Research Laboratory Mass Spectrometer Incoherent Radar empirical model (MSISE-00) [*Picone et al.*, 2002], and the seeding altitude is around 70 km, depending on the Rayleigh signal-to-noise-ratio. During wintertime, the seeding altitude is usually chosen above 70 km, while in summertime, the

seeding altitude sometimes are lowered to 65 km or 60 km. Typical uncertainties of Rayleigh temperature profiles in winter (May to August) are less than 1 K below 50 km, 1–3 K in the range of 50–60 km, and 3–10 K above 60 km under 2-hr integration window and 1 km vertical resolutions. During summer, around local noon, the uncertainties are less than 5 K below 45 km, 5–10 K in the range of 45–55 km, and greater than 10 K above 55 km with 4-hr integration window and 1 km vertical resolutions.

In this study, the Fe temperature profiles are derived from the raw data using hamming smoothing windows with full-width-half-maximum (FWHM) of 1.5 hr and 1 km from March to September. The Rayleigh temperature profiles are derived with 2 hr and 1 km integration windows in winter months (May to August), and 4 hr and 1 km windows for rest of the months. We summarize the monthly diurnal distribution of the hourly lidar data through 2011 to 2014 in Figure 4.1. Most of the universal time (UT) hourly bins for each month contain at least 10 samples except for a few bins in August and September that have fewer than 5 samples (e.g., UT = 2 and 3 in August, and UT = 18 and 19 in September). In general, the 4-year lidar data are distributed quite evenly, which makes the temperature climatology more representative.

The monthly mean lidar temperature profiles were computed using 4 years of measurements. We first obtained a composite day of data that covers a diurnal cycle (24 h) through averaging the temperature measurements in the same UT time and at the same altitude bin on different days within the same month and same year. More data samples in the same hour and altitude bin result in better reduction of the measurement uncertainty of temperature for each bin. If the original temperature uncertainty at 1 h and 1 km resolutions is ΔT and the number of independent samples is N for a bin, the temperature uncertainty of this bin after averaging over these samples is given by $(\Delta T)_{ave} = \Delta T / \sqrt{N}$. From this step, 48 composite days corresponding to 4 year of total 48 months were obtained. Each composite day was then averaged to form a

monthly mean profile. The final monthly mean lidar temperature profiles were obtained by simply averaging the 4 profiles of the same month in 4 years.

The composite method is chosen to calculate the monthly mean temperature is because that in order to obtain a representative climatology temperature structure and to eliminate the bias induced by gravity waves (GWs), planetary waves (PWs), and tides as much as possible, the aliasing signal from these large-amplitude waves must be sufficiently suppressed. There are various and perhaps different processes in Rayleigh and Fe regions that might affect the temperature climatology. *Chen et al.* [2013] and *Lu et al.* [2013] report that during wintertime strong GW in the MLT region and PW activities in the stratosphere at McMurdo were frequently observed. The amplitudes of these waves are usually reach on the order of 10–20 K. *Fong et al.* [2014] reports that the winter temperature diurnal and semidiurnal tidal amplitudes are about 1–3 K below 100 km but can grow quickly with altitude between 100 and 110 km. However, considering the GWs and traveling PWs are phase incoherent from day to day, forming a composite day can sufficiently reduce the effects caused by these waves. Moreover, the composite method, sorting first into hourly bins, naturally removes the temperature variations induced by the diurnal and semidiurnal tides.

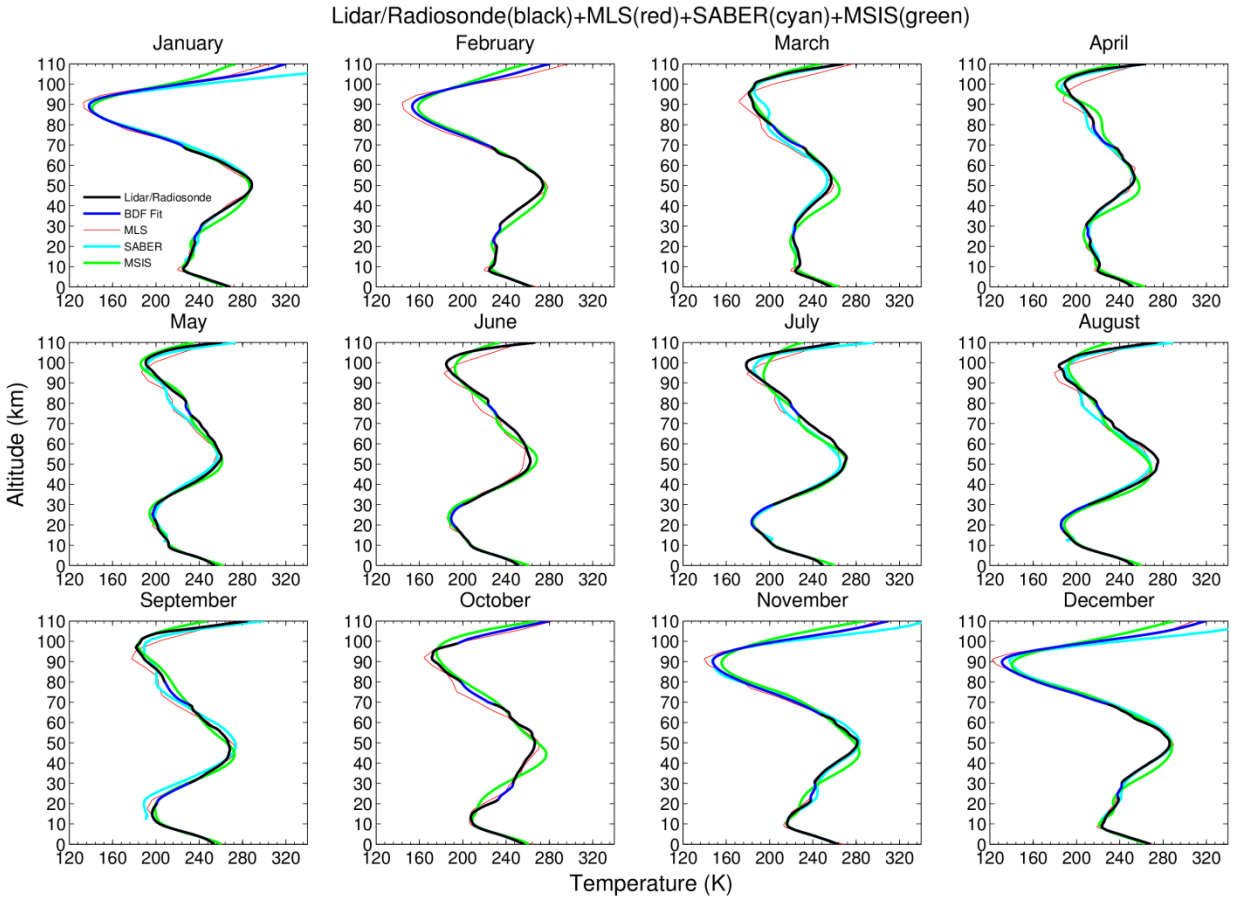

Figure 4.2. 4 year (2011–2014) monthly mean temperature profiles obtained from lidar and radiosonde observations. Radiosonde temperatures are from the ground to ~25 km, Rayleigh temperatures are from 30 km to ~70 km, and Fe temperatures are above 80 km. The BDF predicted temperatures (see section 4.7) are plotted in blue curves. The temperatures observed by lidar and radiosonde in combination with the BDF predicted temperatures were smoothed with a full window of 5 km. Monthly mean profiles from model MSISE-00 (green) and the 2011–2014 monthly mean profiles from MLS (red) and SABER (cyan) are also plotted for references. (No SABER data in February, June, and October due to the instrument viewing geometry and satellite yaw maneuver.)

The monthly mean Fe and Rayleigh temperature profiles are plotted in Figure 4.2 as the bold black curve. During wintertime, both Fe and Rayleigh temperature have good altitude coverage with Fe temperatures spanning from 80 to 110 km and Rayleigh temperatures from 30 to 74 km. For the rest of the months, Rayleigh temperatures also have good coverage from 30 to 70 km; the exception is in November when the highest altitude reaches only 65 km because of the low data quality caused by weather, high solar background, and low lidar power.

Furthermore, the low signal level of the lidar 374 nm channel due to the cold mesopause temperature and the high solar background also challenges the Fe temperature derivations in the non-winter months. For example, the Fe temperature spans from 80 to 99 km in October, and no data is available in summer months for now (November–February). Therefore, in order to fill in the data gaps between Rayleigh and Fe temperatures and compensate for the lack of Fe temperature data between 80 and 110 km in some non-winter months, the 4-step backward differentiation formula (BDF) is applied to fit the gaps by using the temperature gradients derived from the MSISE-00, Sounding of the Atmosphere using Broadband Emission Radiometry (SABER) experiment, and the Earth Observing System (EOS) Microwave Limb Sounder (MLS) temperature measurement. The fitted temperature curves are also plotted as blue curve in Figure 4.2. The detailed description of the BDF method is given in section 4.7.

4.2.2 McMurdo Radiosonde

In this study, we utilized the temperature data collected by radiosonde at McMurdo station to fill in the measurement between ground and 30 km. The main reason that the Rayleigh temperature derivation was halted to ~30 km is because the strong scattered signal from lower altitude can saturate and cause non-linear response of the receiver detector, photomultiplier tubes (PMT). The other reason is that aerosol particles below ~20 km and polar stratospheric clouds (PSC) between 15 and 25 km during winter [e.g., *Di Liberto et al.*, 2014] can cause strong unwanted Mie scattering signals in the lidar raw profiles. The radiosonde balloons were launched regularly twice per day from late September to early March at UT 0 and UT 12 and once per day in winter at UT 0. 200-gram balloons were used during summertime and switched to 300-gram balloons in winter in order to compensate the severe reduction of the balloon elasticity due to the cold stratosphere temperature which causes balloon to burst at lower altitude. The payload was

the Vaisala model RS92-D. The pressure (0.1 hPa resolution, 1 hPa accuracy), temperature (0.1 K resolution, 0.5 K accuracy), and relative humidity (1 % resolution and 5 % accuracy) were sampled every 2 seconds during ascent and the altitude was derived from the pressure. Radiosonde data is available at Antarctic Meteorological Research Center (AMRC) server (ftp://ice.ssec.wisc.edu/pub/mcmurdo/radiosonde/) and is available from 1956 to the present date.

The radiosonde data used were from 2011 to 2014. Since the balloons were launched at fixed times, the monthly mean temperature profile is calculated by averaging the daily profiles obtained in the same month. Similar to the procedures of processing the lidar data, the final monthly mean radiosonde temperature profiles were computed by taking the mean of the 4 profiles of the same month in 4 years. The final monthly mean radiosonde temperature profiles are plotted in Figure 4.2 as bold black curves below ~25 km. As shown in Figure 4.2, data gaps also exist between the Rayleigh temperature and the radiosonde temperature. We applied the same BDF method (to be presented in section 4.7) to predict the temperature in the gaps.

Lastly, the monthly mean temperatures observed by both lidar and radiosonde in combination with the BDF predicted temperatures were vertically smoothed with a full window of 5 km, and the results are plotted in Figure 4.2. For those altitudes covered by radiosonde and lidar measurements, the uncertainties of the mean temperatures are ±1 K or better.

4.3 Seasonal Temperature Variations

4.3.1 Seasonal Variation

Figure 4.3 illustrates the overall monthly mean temperature contour combing the lidar and the radiosonde data. The temperatures calculated by the BDF method are plotted as well at

those altitudes not covered by either lidar or radiosonde measurements. To characterize the seasonal variations in the temperature structure from 0 to 110 km, a harmonic fitting model comprised of the mean temperature and annual, semi-annual, and 4-month sinusoidal components was applied to Figure 4.3:

$$\hat{T}(z,t) = T_o(z) + A_{12}(z)\cos\left[\frac{2\pi}{12}(t - P_{12}(z))\right] + A_6(z)\cos\left[\frac{2\pi}{6}(t - P_6(z))\right] + A_4(z)\cos\left[\frac{2\pi}{4}(t - P_4(z))\right], \quad (4.3.1)$$

where T_o is the annual mean, A_{12}, A_6, and A_4 are the amplitudes, and P_{12}, P_6, and P_4 are the phases of the annual, semi-annual, and 4-month oscillation, respectively. The obtained annual, semi-annual, and 4-month amplitudes and phases are plotted in Figure 4.4.

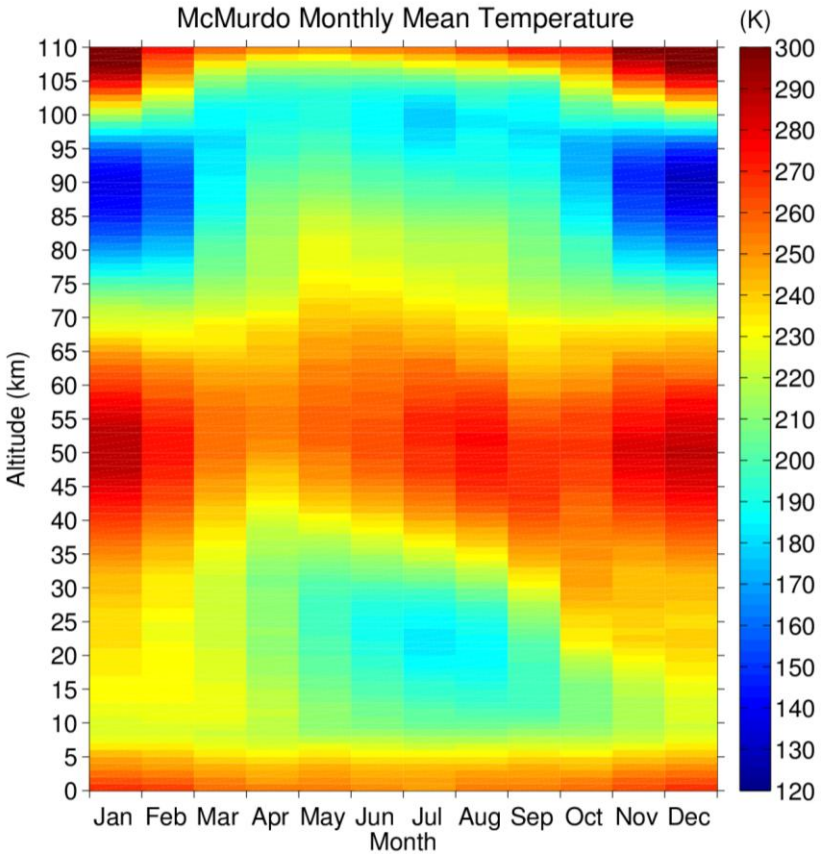

Figure 4.3. Combined monthly mean radiosonde and lidar temperature, with the 4-step BDF method filling in the gaps (see text for details). The vertical resolution is 1 km.

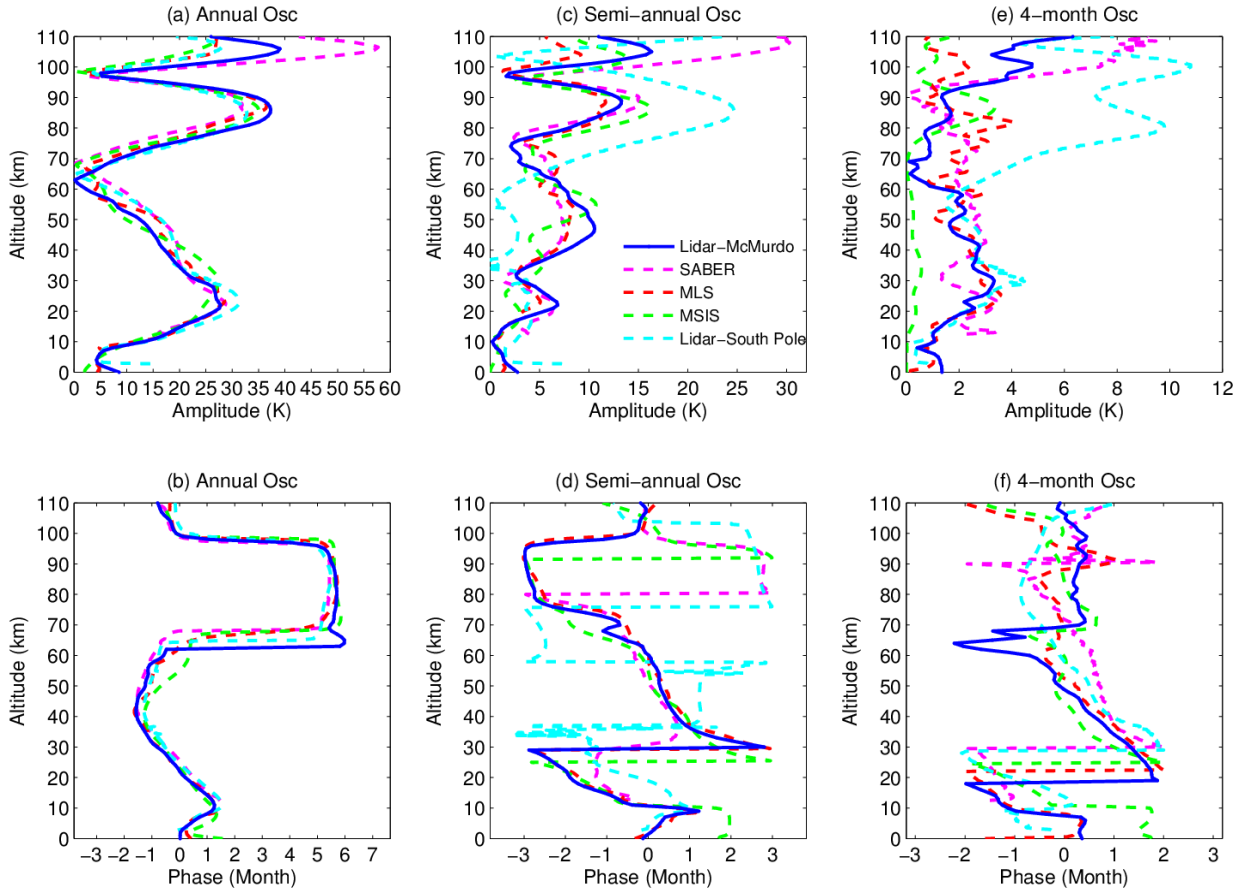

Figure 4.4. Altitude profiles of the (a) annual amplitude (b) annual phase (c) semi-annual amplitude (d) semi-annual phase (e) 4-month amplitude (f) 4-month phase computed from lidar/radiosonde measurements shown in Figure 4.2, SABER (magenta), MLS (red), MSISE-00 (green), and the South Pole lidar measurements (cyan).

In general, the observed annual and semi-annual oscillations dominate at McMurdo from 0 to 110 km, but the annual oscillation is larger. The annual oscillation has three peaks in altitudes: one in the lower stratosphere at about 22 km with an amplitude of 27.2 K, and two in the MLT region at 86 and 106 km with amplitudes of 38.0 K and 40.5 K, respectively. The peak in the lower stratosphere corresponds to the warmest temperature around December and January, and the peak at 86 km corresponds to the warmest temperature in May. The semi-annual oscillation amplitude has four peaks, three of them have peaks at altitudes similar to where the annual oscillation peaks and the forth peak is at 47 km. The 4-month oscillation amplitudes are small and do not have clear peak; the amplitudes are less than 3 K below 95 km and no greater

than 6.3 K above that. Furthermore, an obvious phase shift occurs between 60 and 100 km in the annual oscillation. This is because the summer mesopause region is colder than the winter mesopause region, while the situation is reversed both at lower altitudes and above 100 km (Figure 4.3). The uncertainties of the harmonic amplitudes are ±1.0 K or lower, and the phase uncertainties depend on the harmonic amplitudes. When the harmonic amplitudes are greater than 2 K, the phase uncertainties are less than 10%. Also plotted in Figure 4.4 for comparison are the fitting results from the MSISE-00, SABER, and MLS, which we will discuss in the next section.

4.3.2 McMurdo Temperature Climatology Model

To further characterize the temperature structure at McMurdo, we adopted the approach described in *Pan and Gardner* [2003]. The monthly temperature residuals were firstly computed at each altitude between 0 and 110 km from the monthly temperature with the mean plus harmonic fits removed (annual, semi-annual, and 4-month), and then they were smoothed by a Hamming window with FWHM of 6 weeks and time resolution of 1 day. The smoothing can reduce the short period variations and decrease the measurement errors. The temperature climatology model was then computed from the mean plus the annual, semi-annual, and 4-month fitting results with the smoothed temperature residuals added back. The contour of temperature climatology is plotted in Figure 4.5; we denote this smoothed climatology as MCM-15 in the rest of this paper.

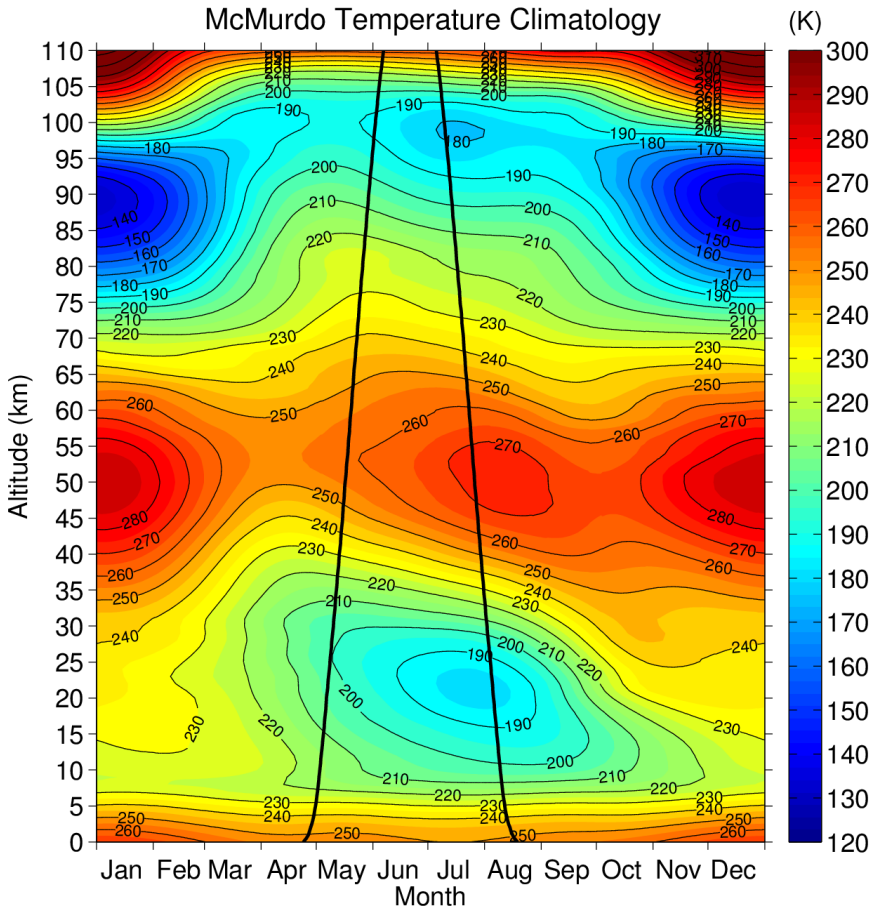

Figure 4.5. The observed mean atmospheric temperature structure at McMurdo (McM-15) from 0 to 110 km. Polar nights (24 h darkness) occur between the bold black curves at 77.8°S. The vertical resolution is 1 km.

Figure 4.5 exhibits the expected temperature structure in the polar region. The summer tropopause with a temperature of ~220 K lies near 8 km. The winter tropopause is indistinct and its altitude is difficult to determine by examining the temperature profile directly [*Zängl and Hoinka*, 2001]. However, using the *World Meteorological Organization* [1957] definition, in which the tropopause is defined as "the lowest level at which the lapse rate decreases to 2 K/km or less", the winter tropopause altitudes at McMurdo vary in the range of 8–12 km (lapse rate profiles not shown). Below the tropopause, there is no distinct temperature seasonal variation through the whole year. In the lower stratosphere, the temperature decreases as the solar heating due to the UV absorption by ozone decreases between fall and early-winter. During winter, the

coldest temperature reaches ~180 K around 20 km in early August when solar heating is absent. After the Sun rises over the lower stratosphere in mid-August, the temperature starts to increase again in this region. At stratopause altitudes, the temperature is mainly determined by the solar heating (negligible in winter), radiative cooling, and the adiabatic cooling/heating associated with the downwelling/upwelling driven by the meridional circulation. In the winter stratopause region, the adiabatic heating warms up the atmosphere and partially offsets the radiative cooling, which results in the existence of a stratopause and warm temperature in the stratopause region when there is no direct sunlight from mid-May to late-July [*Hitchman et al.*, 1989]. After the Sun rises in early August, the stratopause continues warming up with the additional heating from the UV absorption of ozone. However, during September and October, the weakening of the downwelling effect decreases the adiabatic heating. Consequently, the net total of radiative cooling, ozone heating, and adiabatic heating becomes negative and results in a decreasing temperature. In the mesopause region, the cold summer mesopause temperature is as low as ~135 K from December to January, and the elevated and warm mesopause during winter were observed. These mesopause features are also associated with adiabatic cooling in the summer and adiabatic heating in the winter.

The net daily heating and cooling rates were also plotted in Figure 4.6 along with the RMS rate. The net heating and cooling rates were calculated by taking the time derivative of the MCM-15 temperatures at each altitude. Below 100 km, two major periods of heating occur; one in the MLT region from February to March, with the peak of 1.09 K/day, and the other in the lower stratosphere region from late August to October, with a magnitude of 0.90 K/day. The major periods of cooling below 100 km occur in the MLT region from October to November, with a peak of 0.96 K/day, and in the stratopause region from February to March, with a peak of -0.68 K/day.

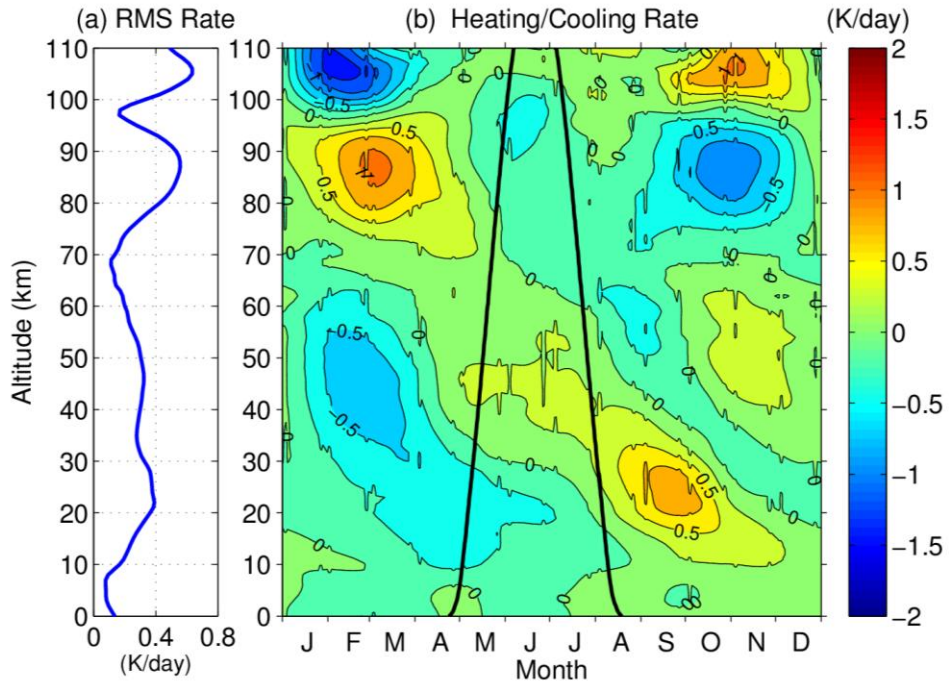

Figure 4.6. (a) RMS rate and (b) daily heating/cooling rates derived from MCM-15 observational data. Polar nights (24 h darkness) occur between the black curves at 77.8°S. The vertical resolution is 1 km.

4.4 Comparison with MSISE-00 model and satellite measurements at McMurdo

4.4.1 MSISE-00 model

We first compare the temperature structures observed by lidar and radiosonde with MSISE-00. The monthly mean MSISE-00 temperature profiles were calculated from all the hourly temperature profiles at McMurdo using the real $F_{10.7}$ solar flux measurements through 2011–2014. With the same composite method as lidar data, total 48 composite days corresponding to 48 months from 4 years were first calculated, and the 4 profiles of the same month in 4 years were then averaged for the monthly mean temperature. The temperature difference between MCM-15 and MSISE-00 (MCM-15 minus MSISE-00) is plotted in Figure 4.7 along with the RMS temperature difference. Below 20 km, MCM-15 is in good agreement with MSISE-00; the RMS differences are less than 6 K except for the ground level (0 km). In the

altitude range of 20 to 45 km, the RMS temperature differences vary between 6 and 10 K. The major temperature differences occur around October from 20 to 30 km, with the positive different of 8–12 K, and the non-winter months from 30 to 45 km, with the negative differernces of 8–16 K. Such temperature discrepancies could be caused by the variation of the ozone concentration, which are not taken into consideration in the MSISE-00 model, or interannual variability in the winter/spring calculation. During winter, it appears that MCM-15 has warmer temperature by 4–8 K from 50 to 70 km and colder temperature by 8–16 K in the mesopause region (95–105 km) than MSISE-00. The colder temperature in the mesopause region could be due to the weaker than expected compressional heating associated with the meridional circulation [*Pan et al.*, 2002; *Kawahara et al.*, 2002]. In the altitude range of 105–110 km, the MCM-15 is in average warmer than MSISE-00 by over 20 K.

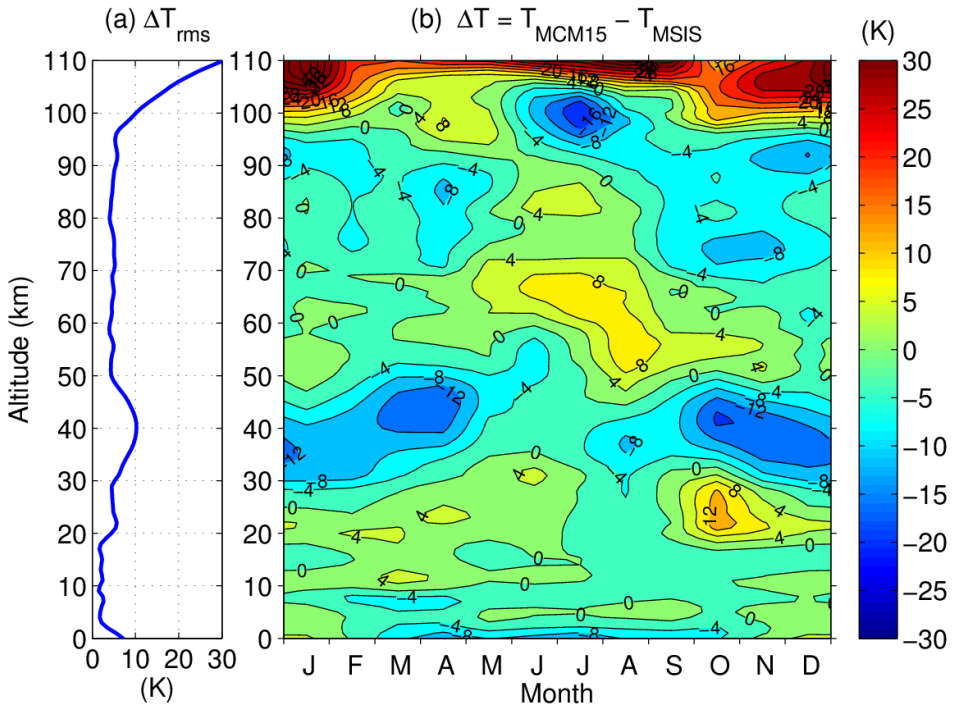

Figure 4.7. (a) RMS and (b) absolute temperature differences (MCM-15 minus MSISE-00) between the MCM-15 observational model and MSISE-00 model. The vertical resolution is 1 km.

Despite the temperature discrepancies, the annual and seasonal variations of MCM-15 and MSISE-00 below 100 km are similar to each other, as shown in Figures 4.4a and 4.4b; above 100 km, the peak amplitude of the annual cycle of MCM-15 is greater than that of MSISE-00 by ~15 K. Differences can also be seen in the semi-annual and 4-month oscillation amplitudes. MSISE-00 has three semi-annual amplitude peaks below 60 km; the altitudes of the peaks do not coincide with the peaks of MCM-15. Moreover, the structure of the 4-month oscillation amplitude of MSISE-00 is also very different from that of MCM-15. The MSISE-00 4-month oscillation has small amplitudes of less than 0.6 K below 75 km and a prominent peak of 3.5 K at 87 km, while MCM-15 amplitudes are over 1 K for most altitudes.

4.4.2 SABER and MLS

The lidar climatology of temperature structure at McMurdo is also compared with the SABER and MLS satellite measurements. SABER is one of the four instruments onboard the NASA Thermosphere, Ionosphere, Mesosphere, Energetics, and Dynamics (TIMED) mission satellite launched in December of 2001. SABER provides global kinetic temperature measurements between 83°N and 83°S from ~10 to 130 km using the measurements from the 15 μm CO_2 channels [*Russell et al.*, 1999; *Gille and House*, 1971]. Because of the viewing geometry of the instrument, the latitude coverage for one day usually extends from 53° in one hemisphere to 83° in the other. This coverage flips every ~60 days due to the yaw maneuvers required for the TIMED satellite. The Earth Observing System (EOS) MLS is one of the four instruments onboard the NASA EOS Aura satellite launched on July 15, 2004. MLS also provides global temperature measurements between 82°N and 82°S from ~0 to 120 km using O_2 spectral lines [*Waters et al.*, 2006; *Schwartz et al.*, 2008]. Unlike the SABER instrument, MLS

cover high southern latitude region year-round without interruption. In this study, we processed the four years of both SABER and MLS temperature data from 2011 to 2014 near McMurdo. The monthly mean temperature profiles were obtained by averaging the daily measurements in the 10° (latitude) by 20° (longitude) area centered at McMurdo. The data can be downloaded from the official websites (http://saber.gats-inc.com/ and ftp://acdisc.gsfc.nasa.gov/ftp/data/s4pa/).

The monthly mean temperature profiles of SABER and MLS are plotted also in Figure 4.2 in order to compare with the lidar and radiosonde measurements. In the troposphere and the lower stratosphere, the SABER and MLS measurements are in good agreement with the radiosonde measurements. In the altitude range 40 to 70 km, both MLS and SABER have colder temperatures than the lidar in winter months (May to August). In the MLT region, it is apparent that MLS has a colder mesopause temperature and a lower mesopause altitude than those of lidar, but those of SABER, on the contrary, are relatively consistent with lidar measurements. However, it should be noted that the vertical resolution of MLS decreases as altitude increases, and the vertical resolution is ~4–5 km in the MLT region. Therefore, it seems that the MLS could not resolve the temperature structure at and above mesopause well. Furthermore, the SABER measurements only cover from mid-March to mid-May, mid-July to mid-September, and mid-November to mid-January, thus the bias for those months with observations only during half part of the month should be considered.

Plotted in Figure 4.8 is the monthly mean temperature difference between MCM-15 and MLS (MCM-15 minus MLS). The RMS differences are less than 5 K between 3 and 60 km, and are less than ~10 K from 60 to 100 km. The generally warmer temperatures of MCM-15 between 60 and 90 km are consistent with those reported by *Schwartz et al.* [2008], i.e. that the MLS measurements have cold bias which could reach -8 K in this altitude range. The SABER also has

a small RMS temperature difference with MCM-15 with less than 6 K below 60 km, and less than 10 K between 60 and 100 km (Figure is not shown). Generally speaking, considering the known cold bias of the MLS data and the other factors discussed above, the temperature structures of both SABER and MLS compare well with MCM-15 below 100 km. We also found that the seasonal annual and semi-annual variations illustrated in Figure 4.4 show similar structures of the three data sets below 100 km. Above 100 km, SABER has the largest annual, semi-annual, and 4-month oscillation amplitudes with peak of 58 K, 31 K, and 9.5 K, respectively; MCM-15 has amplitudes of all of the harmonic oscillations that are between those of SABER and MLS.

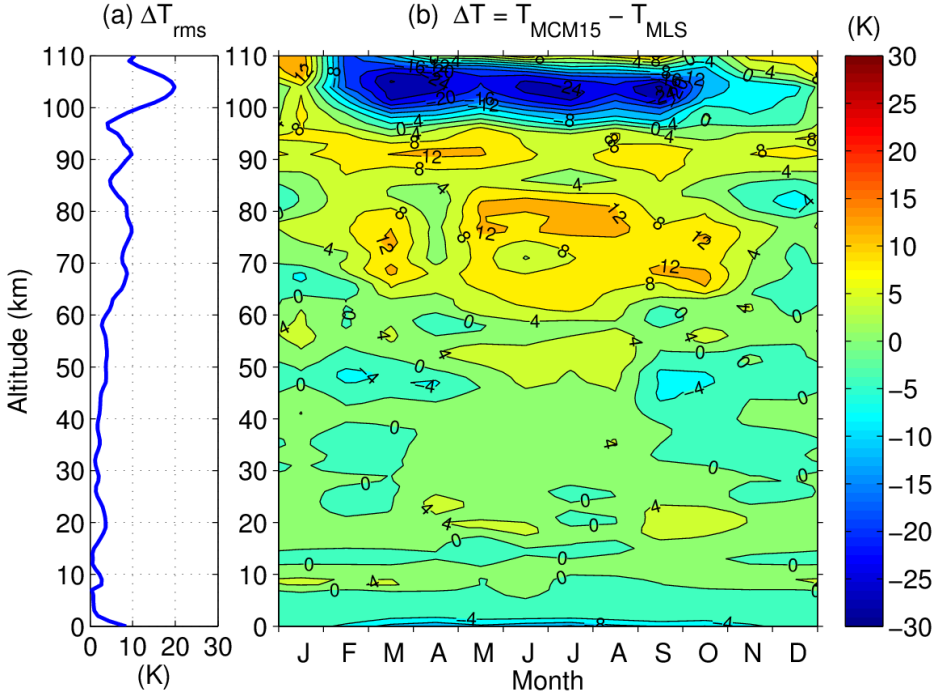

Figure 4.8. (a) RMS and (b) absolute temperature differences (MCM-15 minus MLS) between the MCM-15 observational model and the MLS satellite measurements. The vertical resolution is 1 km.

4.5 Discussion

4.5.1 Latitudinal Dependence

From 1999 to 2001, the University of Illinois lidar group deployed the Fe Boltzmann temperature system and made temperature observations from 30 to 110 km at the South Pole station [*Pan and Gardner*, 2003]. During the same period, the Shinshu University lidar group also deployed a Na temperature lidar system and obtained wintertime temperature (late March to early October) at Syowa station (69°S) [*Kawahara et al.*, 2004]. The two sets of data are excellent references for our McMurdo observations to investigate whether there is latitudinal dependence of the temperature structure in the high southern latitude region. Following the names used in *Pan and Gardner* [2003] and *Kawahara et al.* [2004], we name the South Pole temperature model as UISP-02 and the Syowa temperature model as SYOWA-04.

Although the latitude of McMurdo station is in between the South Pole and Syowa, by comparing the temperature models between the three locations, we found that the general features of temperature structure at McMurdo are closer to those of Syowa than the South Pole (see Figure 4 of *Kawahara et al.* [2004] and Figure 4 of *Pan and Gardner* [2003]). The two salient differences between McMurdo and the South Pole are: 1) In the stratopause region, temperature peaks reaching over 270 K can be seen in both McMurdo and Syowa data around August, while the temperature in the same region in the South Pole monotonically increases from the winter low toward austral summer, and 2) The South Pole has apparent warmer temperature during the transition periods between summer and winter (March–April and August–September) in the MLT region (70–100 km). To further quantify these differences between McMurdo and the South Pole, we subtract UISP-02 from MCM-15 and plot the absolute and the RMS differences in Figure 4.9. From Figure 4.9a, the RMS differences are less than or about 10 K

below 70 km and are larger than 10 K above it. From the Figure 4.9b, below 30 km the temperature structure at the two sites is similar except that McMurdo is warmer by as much as 16 K; this probably due to the earlier breakdown of the polar vortex around this time at McMurdo and the influx of warm air from lower latitudes [*Schoeberl and Hartmann*, 1991]. In the altitude range from 30 to 60 km, McMurdo is ~16 K warmer than the South Pole during wintertime, which might be explained by the gravity wave-induced stratospheric warming near polar vortex jet around mid-winter [*Duck et al.*, 1998]. With a few hundred hours of Rayleigh temperature retrieved at Eureka (80N, 86W), *Duck et al.* [1998, 2001] suggest that the strengthening of the polar vortex jet decreases critical-level filtering of gravity wave, and increased gravity wave momentum deposition above the jet maximum forced flow into the vortex core where it descended and warm adiabatically. The difference in between McMurdo and South Pole is probably because that McMurdo experiences stronger downward adiabatic heating and therefore has warmer temperature in the winter stratopause region [*Garcia and Boville*, 1994]. It is also noteworthy that *Kawahara et al.* [2004] attributed the warmer stratopause of Syowa than the South Pole during the same period to the direct solar heating. However, at McMurdo the stratopause is in 24-hour darkness from mid-May to mid-July (black bold curve in Figure 4.8b), which covers the period where the warmest temperature difference occur, and therefore direct solar heating is not the reason for the warmer winter stratopause at McMurdo.

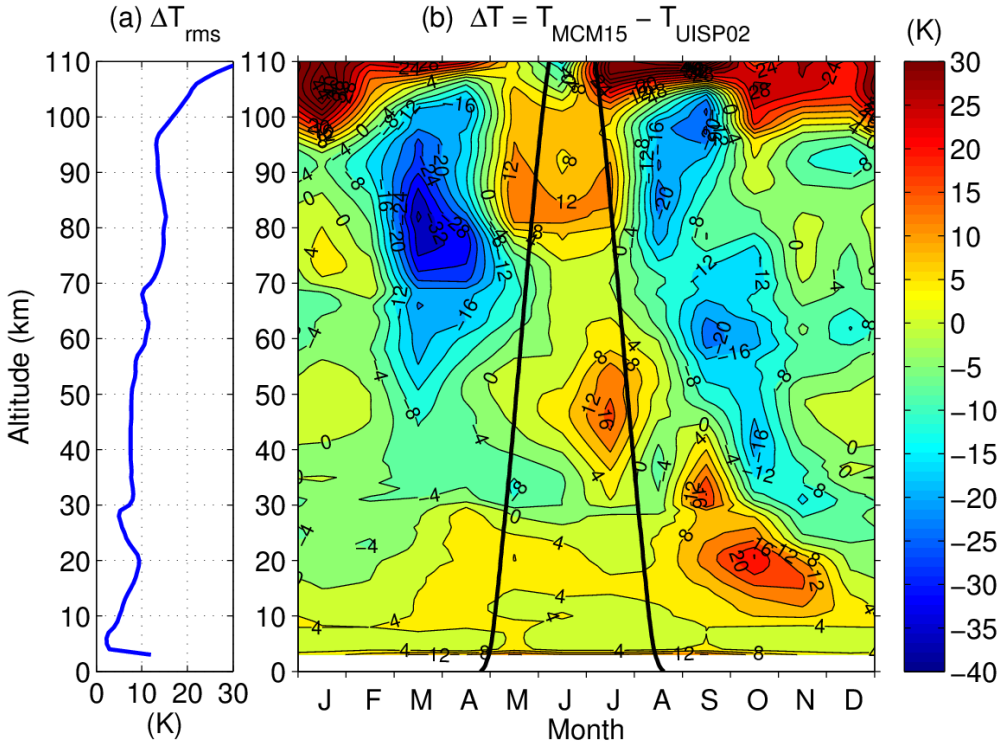

Figure 4.9. (a) RMS and (b) absolute temperature differences (MCM-15 minus UISP-02) between MCM-15 and the UISP-02 observational models. The vertical resolution is 1 km.

In the MLT region, similar to what had been observed in *Kawahara et al.* [2004], the South Pole temperature is colder during winter but is considerably warmer during fall and spring than those of McMurdo. The greatest temperature difference is over 35 K at ~80 km in the fall and about 25 K at 98 km in the spring, which indicates that the warming effects around spring and fall at McMurdo are less pronounced. During fall, the strong warming effect at the South Pole might indicate that the South Pole is affected more by the adiabatic cooling associated with upwelling over the polar cap in summer caused by the meridional circulation. When entering March, the weakening of the adiabatic cooling could not offset the solar UV absorption by ozone and atomic oxygen anymore, thus the mesopause is rapidly warmed up at the South Pole, while such effect is much milder at McMurdo.

The monthly stratopause and mesopause temperatures and altitudes of the three stations are summarized in Figure 4.10. Although there is a stratopause temperature dip in July at the

South Pole, an overall trend of increasing stratopause temperature can still be seen in Figure 4.10a from May to August for all three stations. This trend is consistent with the climatological study of the global stratopause temperatures using 7 years of MLS measurements reported by *France et al.* [2012]. *France et al.* [2012] show that the polar region stratopause in MLS data starts to warm up after midwinter because the cold polar vortex is interrupted by warming over the pole due to GW-driven subsidence from the mesosphere. It is not clear what causes the stratopause temperature dip in July at the South Pole seen in Figure 4.10 but year-to-year variability might contribute. Furthermore, a latitudinal dependence of the stratopause temperatures among three stations from May to August is apparent; that is, Syowa has the warmest winter stratopause temperature and the South Pole has the coldest, while McMurdo has a temperature between the two.

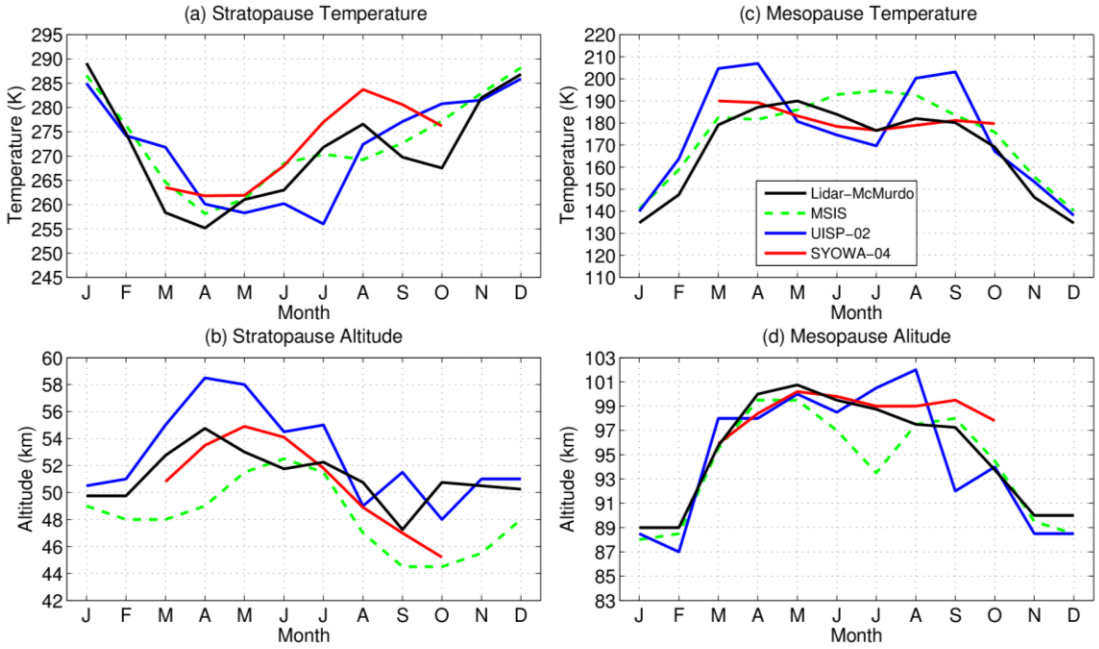

Figure 4.10. Seasonal variations of the (a) stratopause temperature, (b) stratopause altitude, (c) mesopause temperature, and (d) mesopause altitude versus month. MCM-15 (black), UISP-02 (blue), SYOWA-04 (red), and MSISE-00 (green dashed) are plotted. Monthly data of SYOWA-04 are taken from *Karahawa et al.* [2004].

As for the mesopause temperatures shown in Figure 4.10c, the South Pole has the largest mesopause temperature variations from March to October with the warmest temperature of 207 K in April and coldest temperature of 167.1 K in October. Syowa has the smallest variations from the same period with the warmest temperature of 190 K in March and coldest temperature of 176.7 K in July. McMurdo, again, has its variation of the mesopause temperature in between the other two stations with the warmest temperature of 190 K in May and coldest temperature of 169.1 K in October. Therefore, the amplitude of the mesopause temperature variation from March to October is latitudinal dependent. The huge amplitude of mesopause temperature variation occurs from March to October at the South Pole is because of the 24-hour darkness at the altitude of 100 km between mid-April and late-August, which decreases the direct solar heating in the mesopause region. Consequently, the adiabatic heating associated with the downwelling in winter could not offset the radiative cooling, and results in the decrease of mesopause temperature. McMurdo mesopause region is also in 24-hour darkness around mid-winter, but the period of darkness (one month) is much shorter than that of the South Pole, which results in less temperature changes from fall to winter and winter to spring. On the contrary, Syowa does not experience 24-hour darkness at the mesopause altitude in the winter, thus the temperature changes before and after winter are even milder than those of the South Pole and McMurdo. Interestingly, the stratopause and mesopause altitudes do not have apparent latitudinal dependence as shown in the temperatures.

We also compare the seasonal variations of the temperature structure between the three stations. The harmonic fitting results of UISP-02 are plotted in Figure 4.4 (cyan) and those of SYOWA-04 are referred to Figure 3 of *Kawahara et al.* [2004]. Both amplitudes and phases of the annual oscillations of MCM-15 and UISP-02 are in good agreement with each other as shown in Figures 4.4a and 4.4b, but the semi-annual amplitudes of the two are quite different.

Smaller semi-annual amplitudes of UISP-02 in the stratopause region (less than ~3 K) and much larger amplitude between 70 and 100 km (~25 K) are found than those of MCM-15 in Figure 4.4c. Since MCM-15 has an additional peak of warmer temperature in August at the stratopause region, it is expectable that the fitted semi-annual amplitude would be enhanced. Meanwhile, in between 70 and 100 km, as we discussed earlier, UISP-02 has rapid temperature changes during fall and spring, which also enhance the semi-annual amplitudes significantly. Since SYOWA-04 has a similar temperature structure to MCM-15, it is expected that both the annual and semi-annual amplitudes and phases are quite comparable to each other. The exception is that there is no obvious semi-annual amplitude peak for SYOWA-04 in the lower stratosphere as observed in MCM-15.

4.5.2 Temperature Profiles above 110 km

As mentioned earlier the Fe layer can sometimes extend to high altitudes [e.g., *Chu et al.*, 2011b]. Surprisingly, such events happen quite often during winter and were captured by the Fe lidar. When the Fe layer extends above 110 km, it allows us to push the lid altitude of temperature measurement higher than 110 km for winter months. Such thermospheric Fe layer events are not confined to winter months, but because of the low density nature of these thermospheric Fe layers, the lidar needs to have sufficient signal-to-noise ratio to derive robust temperature. This can be easily achieved during winter (solar background is ~0). Furthermore, with the configuration changed of lidar receiver during polar dark night, the receiver optical efficiency can increase by more than 3 times [*Chu et al.*, 2002], which also helps to detect these thermospheric Fe events.

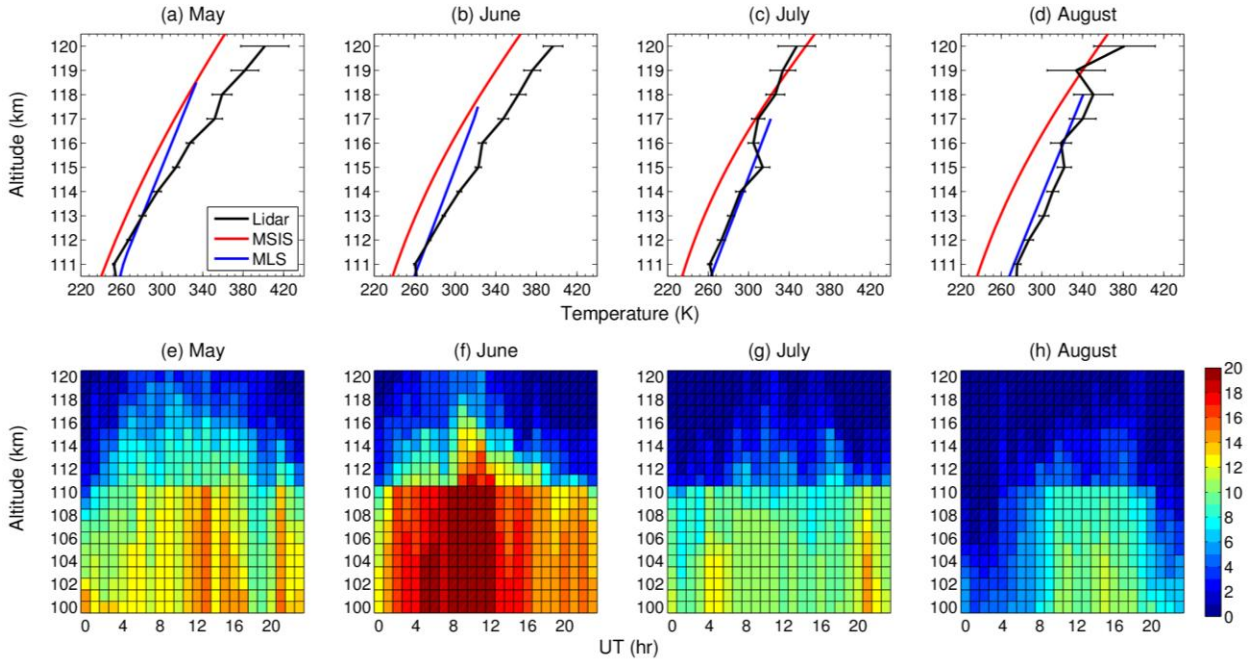

Figure 4.11. (a-d) Monthly mean McMurdo lidar temperatures (black), MSISE-00 (red), and MLS (blue) between 111 and 120 km from May to August, and (e-h) diurnal distribution of lidar hourly data samples from 100 to 120 km. The lidar and MLS data was from 2011–2014.

With careful inspection of the 4-year lidar winter temperature data and removal of the bad profiles, we derived the monthly mean temperature profiles from 111–120 km from May to August, which are shown in Figure 4.11a–d. Using a similar but slightly different method from establishing the composite days for each month and each year when processing the lidar temperature data below 110 km, the monthly composite day contour was computed using all 4 year of data at the same time due to fewer temperature profiles extending over 110 km. The mean temperature profiles between 111 and 120 km were then obtained by averaging the monthly composite day for each winter month. The temperature profiles plotted in Figure 4.11a–d have the same resolutions of 1 hr and 1 km as their lower altitude counterpart. In Figure 4.11e–h, we show the statistics of the monthly diurnal distribution of the hourly lidar data between 100 and 120 km. The reason to show statistics between 100 and 110 km is to emphasis the rapid decrease of the available data between 111 and 120 km, which also explains why we chose

deriving monthly composites using 4 years of data at the same time. As shown in Figure 4.11e-h, June and May have more data available above 110 km than July and August. The average numbers of profile per hour for both June and May are over 6.1 profiles from 111–115 km and at least 2.0 profiles above that; while only ~2.0 profiles from 111–115 km and 0.5 profiles above that are available for July and August.

Plotted along with the monthly mean lidar temperature profiles in Figure 4.11a–d are the MSIS-00 and MLS monthly mean temperature profiles. It should be noted that the MLS data with pressure less than 0.001 hPa could be inaccurate [*Schwartz et al.*, 2008]. Furthermore, there is no other temperature observation available within this altitude range at this time. The lidar temperatures are generally warmer than MSIS in May, June, July, and August between 111 and 120 km by 27.2, 32.2, 14.1, and 30.0 K in average, respectively. At a few altitude points above 115 km in July and August that lidar temperatures are close to or colder than MSIS-00 temperature, but these data could be biased because of the low number of temperature data points. It is noteworthy that MSIS-00 is an empirical model and it simulates atmospheric temperature based on historical data. Since the observational data coverage at this high southern latitude has always been sparse, especially in the altitude range of 110 and 120 km, the existence of a temperature bias is possible.

From the lidar side, in fact, two factors other than the number of profiles in the sample need to be considered that might possibly bias the temperatures above 110 km. Firstly, the available lidar data are relatively concentrated toward local midnight. Over half of the available temperature profiles locate between UT = 9 and UT = 17 hr as shown in Figure 4.11e–h, which correspond to local time (LT) = 20.1 and 28.1 hr, respectively. In other words, more than half of the data are centered within about ±4 hour of local midnight. This is not due to a local variation in the occurrence of elevated Fe layers but, rather, a reflection of the fact that the SNR of lidar

raw profiles were usually higher at this time due to the low solar background. Secondly, an enhanced of the neutral temperature was sometimes observed to occur simultaneously with the appearance of the thermospheric Fe events. In the thermospheric Fe layer events reported in *Chu et al.* [2011], one of the two events had Fe temperature warmer than MSISE-00 temperature by more than 50 K between 111 and 120 km. However, it should be noted that the cases reports in *Chu et al.* [2011] are the cases under strong geomagnetic disturbance, for which the aurora-enhanced heating could last for hours and thus the significant temperature increase in the neutral atmosphere can occur.

Nevertheless, these McMurdo lidar temperature profiles from 111–120 km are still valuable and could serve as reference for satellite measurements or atmospheric models. Currently, almost no satellite measurements can provide reliable neutral temperature measurements at this altitude range in the polar region, and no other ground-based measurements can provide range-resolved neutral temperature either. In the past, the only experimental method to retrieve temperature between 110 and 120 km was through in-situ rocket measurement, but which provides only the snapshots of temperature profile [e.g., *Best et al.*, 1947].

4.6 Conclusions

The McMurdo lidar campaign has provided valuable data of the polar middle and upper atmosphere. In company with the radiosonde, we characterize the seasonal variations of the temperature structure from the ground to the lower thermosphere at McMurdo using 4 years of observations. The dominant annual and semi-annual oscillations of the temperature structures have also been characterized. The temperature structures generally compare well with the SABER and MLS satellite measurements. The stratopause temperatures during winter and the

mesopause temperature variations from March to October show latitudinal dependence among the three stations (McMurdo, the South Pole, and Syowa) at three difference latitudes. The essence of the latitudinal dependence is the balance among solar heating, radiative cooling, and adiabatic cooling/heating associated with the upwelling/downwelling effect driven by the meridional circulation. We also demonstrate the potential for McMurdo lidar to push the altitude limit of the monthly mean temperature over 110 km during winter. This is a region where temperature measurements are extremely sparse. The temperature profiles above 110 km are about 14–30 K warmer than MSISE-00. Overall, the McMurdo lidar temperature measurements not only fill in the data gap between the South Pole and Antarctic Circle, but will also provide crucial information to the atmospheric models and other measurements.

4.7 Appendix 4A: Temperature Gap Filling with Backward Differentiation Formula Method

A 4-step BDF method was utilized in this study to predict the temperature where the lidar or radiosonde data were not available. BDF is one of the implicit methods for numerical integration of ordinary differential equation. The 4-step BDF equation can be written as [*Süli and Mayers*, 2003]:

$$T(z_n) = \frac{1}{25}\left[48T(z_{n-1}) - 36T(z_{n-2}) + 16T(z_{n-3}) - 3T(z_{n-4}) + 12\Delta z T'(z_n)\right], \qquad (4.7.1)$$

where $T(z_n)$ is the temperature at altitude z_n, $T'(z_n)$ is the temperature gradient at altitude z_n, and Δz is the altitude step size. In our case, $T(z_n)$ is the temperature to be calculated, $T(z_{n-1})$ to $T(z_{n-4})$ are the observation data from lidar and radiosonde, Δz is taken to be 1 km, and $T'(z_n)$ is the temperature gradient pre-calculated from the SABER and MLS satellite measurements, and also the MSISE-00 model output. For example, assuming that the data gap to be filled is from 70 to

80 km and the starting point is 70 km, equation (4.7.1) will be recursively computed for $T(z_n)$ moving from 70 km to 80 km with step size Δz equals 1 km, and $T(z_{n-1})$ to $T(z_{n-4})$ are always to be the known values from the observation data or the results of the previous calls of equation (4.7.1).

Figure 4.12 illustrates the temperature gradients derived from the monthly mean temperatures of the SABER, MLS, MSISE-00, and the mean of three. Before calculating the temperature gradients of each data set, a vertically running smoother with window width of 7 km was applied to the monthly mean profiles. The final temperature gradient profile used in equation (4.7.1) is the arithmetic mean of the three (blue curves). In general, as shown in Figure 4.12, the temperature gradients of the three data sets are in good agreement at those altitude ranges where this BDF method is mostly used (20–30 km and 70–80 km).

Furthermore, we calculate the data gaps to be filled from both directions and then take the average of the results from equation (4.7.1). In other words, if the data gaps are from 70 to 80 km, we then repeat the above procedures twice but with opposite directions and different starting points at 70 and 80 km. In some cases, if only one direction is available (e.g., altitude above 100 km in October, Figure 4.3), then the gaps will be filled with the result calculated from this direction.

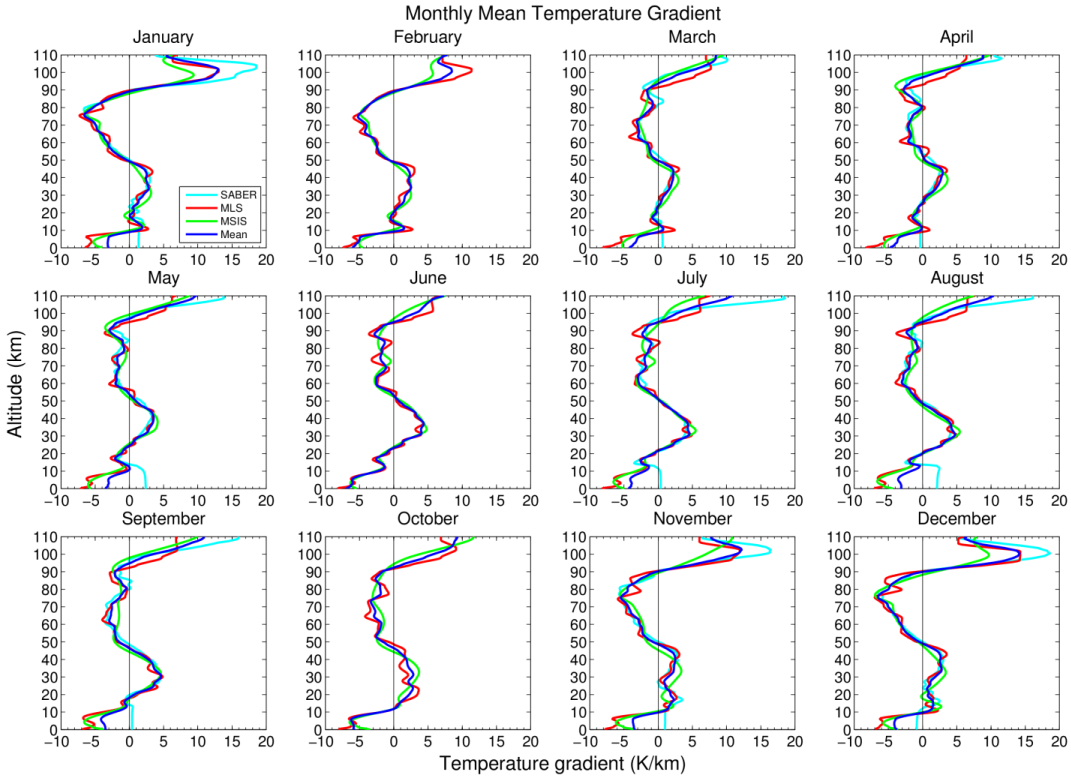

Figure 4.12. Monthly mean temperature gradient profiles of SABER (cyan), MLS (red), and MSISE-00 (green). The temperature gradient is derived from the vertically running smoothed monthly temperature profiles with window width of 7 km. The mean temperature gradient (blue) is the average of the temperature gradients of the three datasets.

CHAPTER 5

Doppler Lidars and Calibration

5.1 Introduction

Boltzmann and Doppler lidars are two types of the resonance fluorescence lidars which are capable of measuring temperatures and constituent densities simultaneously in the middle and upper atmosphere. Boltzmann lidar excites two states of the neutral metallic atom and calculates temperature from the population ratio of the two states based on the Maxwell-Boltzmann distribution law. Currently, this Boltzmann technique is only used in detecting Fe atom in the MLT region [e.g., *Chu et al.*, 2002]. On the other hand, Doppler lidar utilize the temperature dependence of Doppler broadening of electronic-dipole transition lines of the tracer gases. Nowadays, Na, Fe, and K are the three most popular tracer gases used by Doppler lidars for measuring temperature in the middle and upper atmosphere.

Boltzmann and Doppler lidars have their own advantages and disadvantages. For Boltzmann lidar, first of all, it can measure temperature precisely at where Fe layer density reaches over minimum criteria. Secondly, in detecting thermospheric layer events, Boltzmann system has high sensitivity; in the thermosphere region, the temperatures usually reach over 400 K, where the 374 and 372 nm populations are in the same order of magnitude, where the population ratio of the two states P_{374}/P_{372} is about 1/5.8 at 400 K and about 1/4.3 at 500 K. The population ratio roughly equals to the ratio of the lidar receiving signal strengths of the two channels if assuming the two channels have similar laser power. However, the disadvantages of Boltzmann lidar are: Firstly, it can only provide temperature measurement since the lidar is a

broadband system and is insensitive to radial wind. Secondly, in the polar summer, Boltzmann lidar could not provide good temperature measurements because of the low signal strength in the 374 nm channel due to the extreme cold mesopause temperature (P_{374}/P_{372} is ~1/130 at 130 K).

For Doppler lidars, the most appealing advantage is the capability of measuring radial wind along with the temperature and metallic layer density simultaneously. In order to advance our understandings of middle and upper atmosphere nowadays, neutral wind measurements are definitely needed. Secondly, the Doppler lidar can usually obtain higher signal strength than that of the Boltzmann system because that the nominal operating point of the system is at the optimal frequency (the absorption peak of the tracer gas) and the system is narrowband. However, there are also drawbacks for the Doppler systems. Firstly, the Doppler system demands much more "intensive" calibration than Boltzmann system, because that the temperature and radial wind measurements are sensitive to lidar pulse spectra and frequency tuning errors. Secondly, the sensitivity lowers down when temperature increase over 400 K, which becomes a disadvantage when measuring temperature in the lower thermosphere where temperature can easily reach over 400 K. Figure 5.1 shows an example of the comparison of the sensitivity between the Fe Boltzmann technique and the Na Doppler 3-frequency technique. The definition of the sensitivity is from equation (5.100) of *Chu and Papen* [2005]. From Figure 5.1, the Na Doppler lidar has in general smaller sensitivities than those of Fe Boltzmann by more than 2 times. And for temperature greater than 350 K, the sensitivity of the Na Doppler lidar is less than 0.25 %.

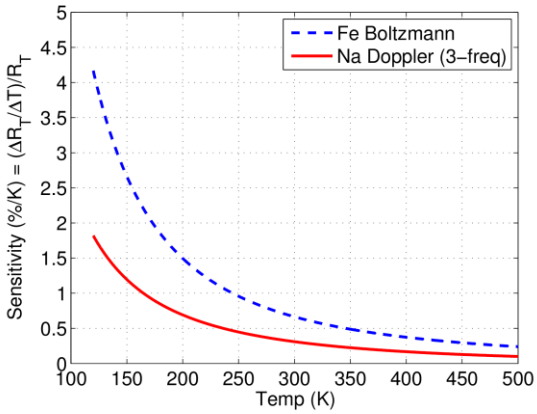

Figure 5.1. Comparison of sensitivity of the ratio R_T for the Fe Boltzmann technique and the Na Doppler technique (3-frequency).

In the summer of 2010, the "Student Training and Atmospheric Research" (STAR) lidar was built by the University of Colorado lidar group at Table Mountain lidar observatory at Boulder. This lidar is a narrowband 3-frequecy Na Doppler lidar, which is capable of probing the atmospheric temperature, radial wind, and Na density simultaneously of the MLT region. In the first year of the lidar operation, the receiving raw Na layer signals were approximately 20–30 counts per lidar pulse shot with the power-aperture product of ~60 mW·m^2 (450 mW laser power and 400 mm telescope). This receiving signal strength was much lower than the expected performance of ~200 counts per shot from the simulated lidar results. Several factors would affect the strength of the signal level such as laser power, laser beam divergence angle, receiver chain alignment, and etc. Since the lidar simulation takes the specifications of the transmitting laser pulse into account, we believed the discrepancy between the experiment and simulation results is mostly from the imperfection alignment of the lidar receiver. Therefore, later on, the lidar receiver design and implementation were revisited and every optical component including optical path was modeled precisely with the help of the ray-tracing software ZEMAX [*Smith and Chu*, 2015]. Consequently, the signal level had been improved significantly by at least of a factor of 10 and found to be consistent with the lidar simulations. The Na layer signal reached 2000

counts per shot when the peak abundance of Na layer occurred during winter with the power-aperture product of ~230 mW·m^2 (450 mW laser power and 810 mm telescope). Details of the receiver chain design and optimization can be found in *Smith and Chu* [2015].

With the largely improved signal strength, both temporal and spatial resolutions of the lidar profiles can be increased. These high-resolution observations open new doors for scientific research, such as vertical transport of heat and constituents by turbulent eddy mixing [*Smith and Chu*, 2015]. They also allow the investigation of high-frequency gravity waves in temperature and wind. Illustrated in Figure 5.2 is an example of the temperature and line of sight (LOS) wind (vertical wind in this case) observed by the STAR lidar at Table Mountain, Boulder, with temporal resolution of 5 minutes. From Figure 5.2, short period (< 1 hour) perturbation features can be easily found in the measurements. This is probably the first ground-based lidar in the world that can provide such fine probing of the MLT region with small power-aperture product.

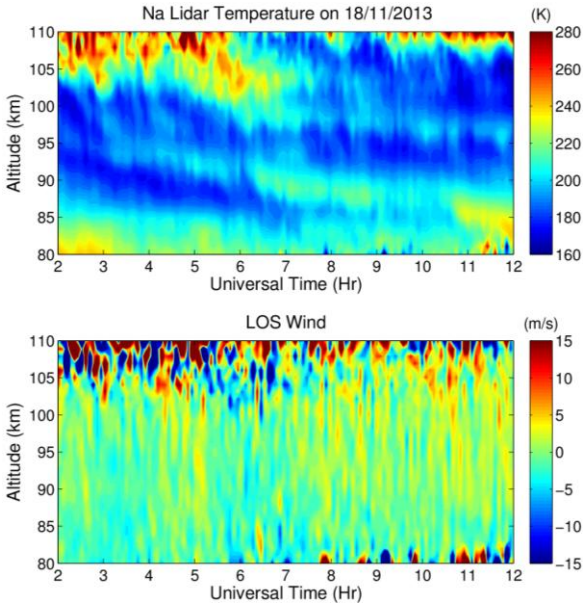

Figure 5.2. STAR lidar observations of temperature and LOS wind (vertical wind) at Table Mountain, Boulder, on November 18, 2013. The temporal resolution is 5 minutes. Short period "vertical stripe" pattern can be seen in both measurements. Data was provided by Wentao Huang.

Nevertheless, a concern is raised about the accuracies of the lidar measurements. In the past, the measurement accuracies stay well within the measurement precisions because of the poor signal strength. Now, the measurement precisions were improved after the signal strength was improved, and it makes the measurement accuracies become critical. To obtain good absolute temperature and wind measurements, both precise and accurate measurements are needed. As mentioned earlier, the Doppler lidar temperature and wind measurements are sensitive to lidar pulse spectra and required much more intensive calibrations than the Boltzmann lidar. In fact, the measurement accuracies of the Doppler lidar are found to be dominated by the two factors: the PMT non-linear response and the short-term variability lidar pulse spectra. Firstly, the huge increase of signal level pushes PMT into the saturation region, where the response of the PMT signal is not linearly proportional to the input signal anymore [*Smith et al.*, 2012]. Secondly, the short-term variability of the laser pulse spectrum, including linewidth and lineshape, also affects the temperature and wind derivation. When the receiving signal level was low in the past, these issues were not concerns, because the PMT output signal stayed well within the linear response region, and the low temporal and spatial resolutions averaged out the effects of the short-term variability of the laser spectrum. Enabling the access to the high-frequency wave structure from the high level of received signal also increases the demands of the knowledge of the characteristics of the instruments.

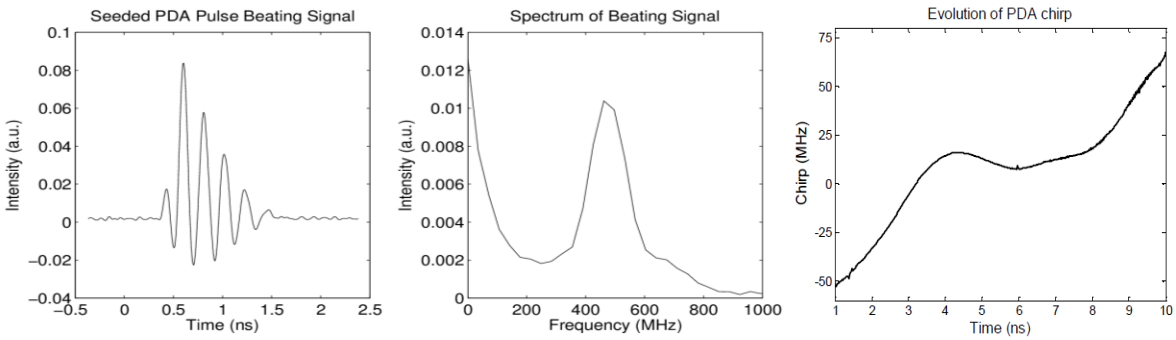

Figure 5.3. Optical heterodyne detection (OHD) of STAR lidar seeded PDA output pulse. (left) Beating signal of PDA output pulse (AOM shifting frequency is 480 MHz) and the ring dye laser, (middle) spectrum of the beating signal, the peak frequency in the center is at about 480 MHz, and (right) evolution of PDA chirp with time. Figures were provided by Drs. Xinzhao Chu and John Smith.

Figure 5.3 gives an example of the STAR lidar pulse spectrum through optical heterodyne detection (OHD) method. Details of this figure will be discussed later in this chapter. The point here is to show that the lidar pulse spectrum in reality is not a perfect Gaussian profile, but the perfect Gaussian profile is usually assumed for the lidar pulse spectrum when retrieving temperature and radial wind measurements from the raw data. Therefore, such assumption would affect the measurement accuracies.

In this chapter, we use STAR lidar as an example and utilize the forward model method to investigate how the PMT non-linear response and laser pulse spectrum affect the temperature and radial wind measurements. The brief review of the temperature and radial wind derivation of the 3-freqency Na Doppler is in section 2, and the forward model simulation is introduced in section 3.

5.2 Temperature and Radial Wind Derivation

For the 3-frequency Na Doppler lidars, the temperature and radial wind are usually derived simultaneously. In principle, from the Na Doppler lidar return signals, we can infer the

effective absorption cross-section of the Na atom in the MLT region with the known laser pulse spectrum (center frequency and lineshape) and some other parameters. The effective absorption cross-section is also determined by the MLT region temperature (Doppler broadening) and radial wind (Doppler shift). Therefore, with the three different frequencies of lidar pulses, we can infer the shape of the Na absorption spectrum and thus determine the temperature and radial wind. More detailed explanations can be found in many books or articles, for example, *Chu and Papen* [2005]. To derive temperature and radial wind simultaneously, usually either Newton's method or the calibration curve interpolation method is used. In this study, in order to make the forward model introduced later becomes more illustrative, we choose the calibration curve interpolation method for temperature and radial wind derivation. It is worth noting that both methods could reach the same results.

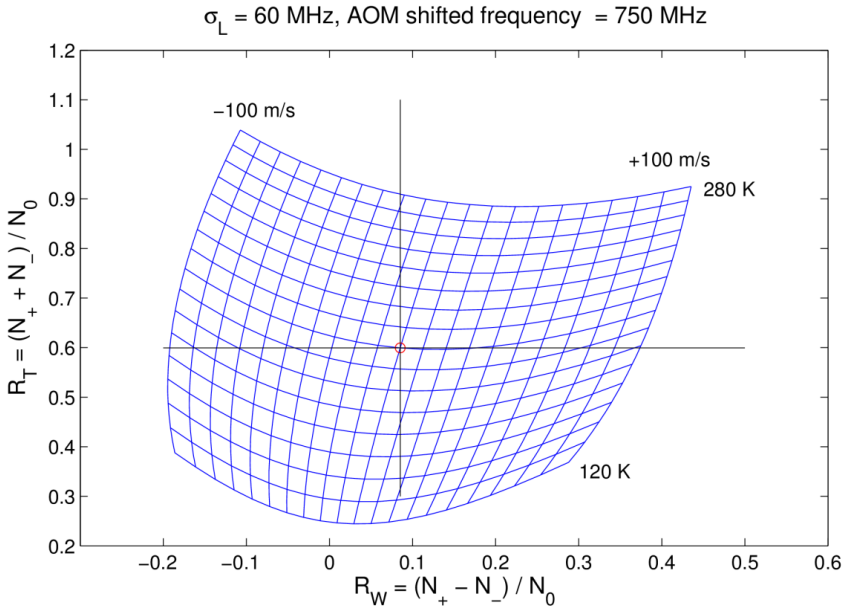

Figure 5.4. Na 3-frequency Doppler lidar calibration curve example. The temperature and radial wind correspond to the red circle are 200 K and 0 m/s, respectively, with R_W = 0.0852, and R_T = 0.5994. The laser RMS linewidth is 60 MHz, and AOM shifted frequency is 750 MHz. See text for details.

A lidar calibration curve example is shown in Figure 5.4. The N_0, N_+, and N_- correspond to the normalized photon counts for the three lidar pulse frequencies f_0, f_+, and f_-, respectively. Usually, the f_0 is locked to D_{2a} peak of the Na absorption spectrum, and f_+ and f_- are the up-shift and down-shift frequencies that deviate from f_0 by a few hundred MHz. f_+ and f_- are usually achieved by the acousto-optic modulators (AOMs) [*Chu and Papen*, 2005]. It can be shown that the R_W and R_T in Figure 5.4 are also equivalent to substituting N with the effective absorption cross-section σ of the corresponding frequencies. In other words, we can write:

$$R_W = \frac{\sigma_+ - \sigma_-}{\sigma_0} \tag{5.2.1}$$

$$R_T = \frac{\sigma_+ + \sigma_-}{\sigma_0}. \tag{5.2.2}$$

As mentioned earlier, the effective absorption cross-section is mainly determined by the laser pulse spectrum, temperature, and radial wind. Therefore, with the known laser pulse spectrum, R_W and R_T can be calculated as calibration curves with the presumed temperature and radial wind as shown in Figure 5.4. The function of the pre-calculated calibration curve is similar to a lookup table. While retrieving the real atmospheric temperature and radial wind, we compare the R_W and R_T, calculated from the normalized photon count N_0, N_+, and N_- (real lidar data), with the calibration curve (lookup table) and then find the corresponding temperature and wind values with the interpolation method from the nearest lattice.

5.3 Forward Model to Assess Temperature and Radial Wind Uncertainties

From the previous section, we know that the key for accurate temperature and radial wind retrieval is to have a "good" calibration curve pre-calculated. The calibration curve shown in Figure 5.4 is in fact the case we expect the STAR lidar should have ideally. However, in reality,

the non-linear response of PMT and imperfection of the lidar pulse spectrum will introduce discrepancies into the calibration curve. In this section, we will use a forward model to assess the temperature and radial wind uncertainties caused by these factors. The idea of this forward model test is to generate calibration curves under different assumptions of the situation of the PMT and lidar pulse, and then derive the temperature and radial wind discrepancies by comparing the calibration curves with the ideal case (Figure 5.4).

5.3.1 PMT Non-linear Response

Smith et al. [2012] demonstrated a test for the PMT non-linear response and derived a saturation correction function by polynomial fitting the PMT input-output curve. With this saturation correction function, the real receiving photon count can be calculated correctly from the PMT output photon count. However, according to the real lidar raw data, it appears that the PMT may have been over-saturated after the signal level had been improved significantly as introduced earlier. Here the over-saturated situation means that the real receiving photon count is too large to be calculated correctly even the saturation correction function is applied. Therefore, it is still desirable to use forward model to investigate whether unaccounted input photons still exist. Considering the nominal photon count levels of the three frequency channels, the f_0 channel usually possesses the greatest photon counts because it corresponds to the largest effective absorption cross-section of Na atom. f_+ and f_- roughly have the same photon counts. Thus, the f_0 channel is more likely to have input photon count that is not accounted for. We assume a coefficient a to scale the normalized photon count N_0. This coefficient a is smaller than 1 because N_0 is underestimated, and we rewrite R_W and R_T as the following:

$$R_W^{'} = \frac{N_+ - N_-}{a \cdot N_0} \tag{5.3.1}$$

$$R_T^{'} = \frac{N_+ + N_-}{a \cdot N_0} \tag{5.3.2}$$

Figure 5.5 illustrates the calibration curve with a = 0.9 in equations (5.3.1) and (5.3.2). The curve is shifted upward and expanded compared with the original curve, indicating that the temperature becomes warmer and the radial wind amplitude generally becomes greater than the values derived from the original curve. For example, the temperature isopleths of 200 K (red) correspond to warmer temperature isopleths (gray) in the original calibration curve. Similarly, we find greater radial wind amplitudes within the new calibration curve. In other words, to calculate the temperature and wind difference introduced from the PMT non-linear effect, we first select $R_W^{'}$ and $R_T^{'}$ with the known temperature T' and radial wind W' from the new calibration curve, and then find the corresponding T and W in the original calibration curve. The temperature and wind differences are calculated by simply subtracting T and W from T' and W', respectively.

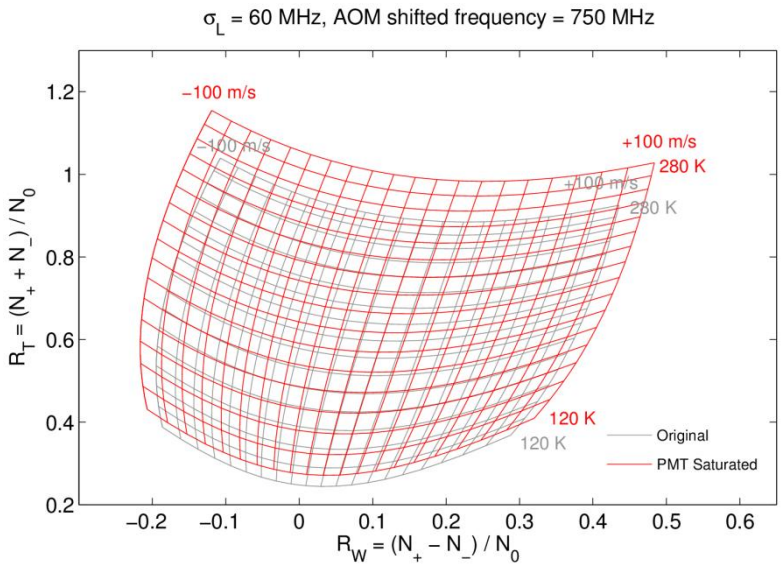

Figure 5.5. Calibration curves of PMT saturated condition (red) with coefficient a = 0.9 (equations (5.3.1) and (5.3.2)) and the original (gray, same as Figure 5.4).

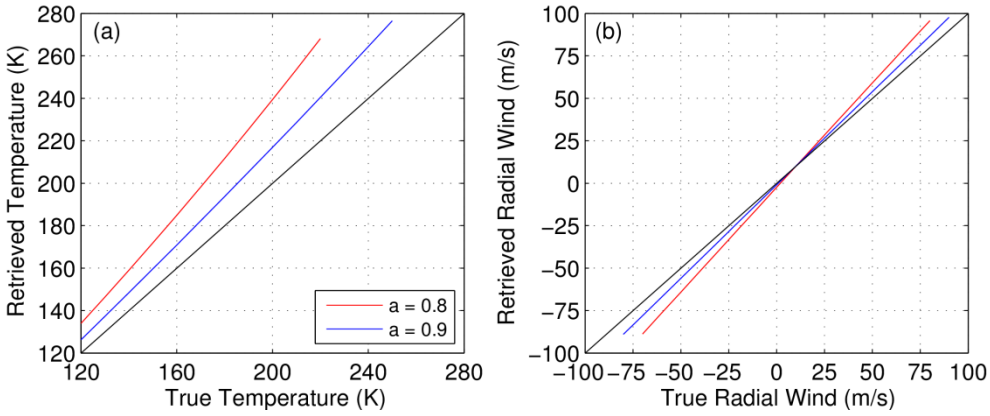

Figure 5.6. Temperature and radial wind values under different values of the coefficient *a*. The radial wind is fixed at 0 m/s in (a), and temperature is fixed at 200 K in (b).

Figure 5.6 shows the temperature and radial wind differences between true and retrieved values under different coefficient *a* with the fixed radial wind and temperature, respectively. It can be seen that the differences increase as the coefficient *a* decreases for both temperature and wind. The temperature changes about 1.6 K at T = 200 K and 1.1 K at T = 160 K per 0.01 change of coefficient *a*, and the wind changes about -0.12 m/s at W = 0 m/s per 0.01 change of coefficient *a*.

5.3.2 Lidar Pulse Linewidth

The STAR lidar pulse is generated from a seeded pulsed dye amplifier (PDA) pumped by frequency-doubled Nd:YAG (532 nm) pulsed laser. The spectrum of the lidar pulse is strongly influenced by the pulse shape of the Nd:YAG pulse [*Chu and Papen*, 2005]. The lidar pulse spectrum, as we discussed earlier, is also an important factor contributing to temperature and radial wind uncertainties in addition to the PMT saturation correction. The lidar pulse spectrum is characterized mainly by the linewidth and line shape. In this section, we first exam that how the different lidar pulse RMS linewidths would affect the temperature and the radial wind. To

simplify the situation, we assume that the lidar pulse is a single Gaussian profile but the RMS linewidth varies due to the seeding condition of the Nd:YAG laser. Ideally, the PDA output pulses from a stable injection-seeded Nd:YAG laser have RMS width approximately of 60 MHz [*Chu and Papen*, 2005]. On the contrary, the unseeded Nd:YAG laser would increase the RMS width of the PDA output pulse to about 130 MHz. Figure 5.7 shows the calibration curve (red) with wider RMS linewidth of 130 MHz plotted along with the original calibration curve with RMS width of 60 MHz. The curve is shifted upward comparing with the original one, indicating warmer temperatures than those derived from the original curve, but radial winds have relatively small changes.

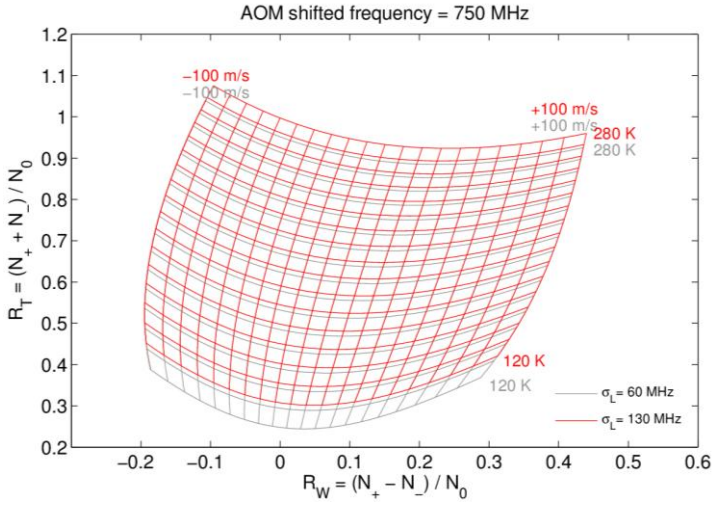

Figure 5.7. Calibration curves with different lidar pulse RMS linewidths of 130 MHz (red) and 60 MHz (gray, same as Figure 5.4).

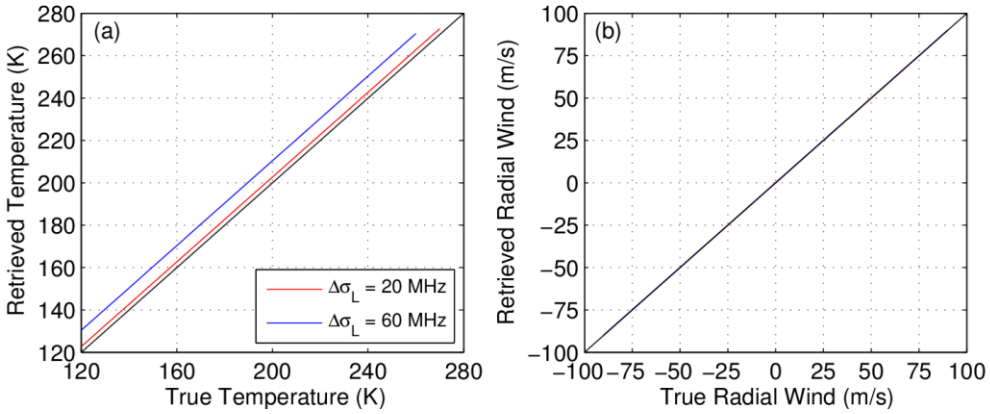

Figure 5.8. Temperature and radial wind values under different RMS linewidth σ_L, here $\Delta\sigma_L$ is the difference between the assumed RMS linewidth and the original RMS linewidth 60 MHz. Radial wind is fixed at 0 m/s in (a), and temperature is fixed at 200 K in (b).

Figure 5.8 shows the temperature and radial wind differences between true and retrieved values with the fixed radial wind and temperature, respectively, under different RMS linewidths. It can be seen that the differences increase as $\Delta\sigma_L$ increases for temperature. Interestingly, the changes of radial wind are almost negligible. The temperature changes by about 5.0 K per 20 MHz change of RMS linewidth and the wind changes by less than 0.01 m/s per 20 MHz change of RMS linewidth.

5.3.3 Lidar Pulse Shape

Following the discussion in the previous section, the unseeded or poorly seeded Nd:YAG pump laser may contain multiple modes in a pulse and therefore may cause the PDA output pulse spectrum to deviate from the single Gaussian profile [*Chu and Papan*, 2005]. We categorize the deformation of the PDA output pulse into two types: 1) PDA pulse spectrum is deformed but still symmetric and 2) PDA pulse spectrum is deformed and is asymmetric. For both cases, the similar approach or adding multiple Gaussian profiles with different RMS linewidths and different peak intensities together to simulate the PDA pulse spectrum is used. Each Gaussian

profile has its own corresponding effective absorption cross-section spectrum of Na atom depending on the RMS linewidth and center frequency. The final equivalent effective absorption cross-section spectrum is obtained by taking the weighted average of these spectra with the weighting determined by the peak intensities of the Gaussian profiles. Then the calibration curves can be calculated using the same R_W and R_T equation as shown in equations (5.2.1) and (5.2.2) except that the equivalent effective absorption cross-sections are used here.

For the first case, the PDA pulse spectrum is deformed but still symmetric and the assumption is made that the pulse spectrum can be decomposed into two Gaussian profiles. One Gaussian RMS width is 60 MHz, representing the original good PDA pulse spectrum, and the other has wide RMS width of 2000 MHz, representing the bad portion of the PDA pulse spectrum. Figure 5.9 shows the calibration curve (red) with the peak intensity ratio of RMS linewidth 60 MHz to 2000 MHz equals 0.9:0.1. The curve is shifted upward and shrunk comparing with the original one, indicating warmer temperatures and smaller radial wind amplitudes.

Figure 5.10 shows the temperature and radial wind differences between true and retrieved values with the fixed radial wind and temperature, respectively, under two different intensity ratios between the two Gaussian profiles with RMS linewidths 60 MHz and 2000 MHz. The two relative intensities are 4% and 8% of the 2000 MHz Gaussian profile, which correspond to 96% and 92% of the 60 MHz Gaussian profile, respectively. It can be seen that the temperature difference increases as the portion of the Gaussian profile with RMS linewidth 2000 MHz increases, and the changes of radial wind are relatively small. The temperature changes about 1.2 K at T = 200 K and about 1.1 K at T = 160 K per 1% change of mix intensity ratio, and the wind changes about -0.2 m/s at W = 0 m/s per 1% change of mix intensity ratio.

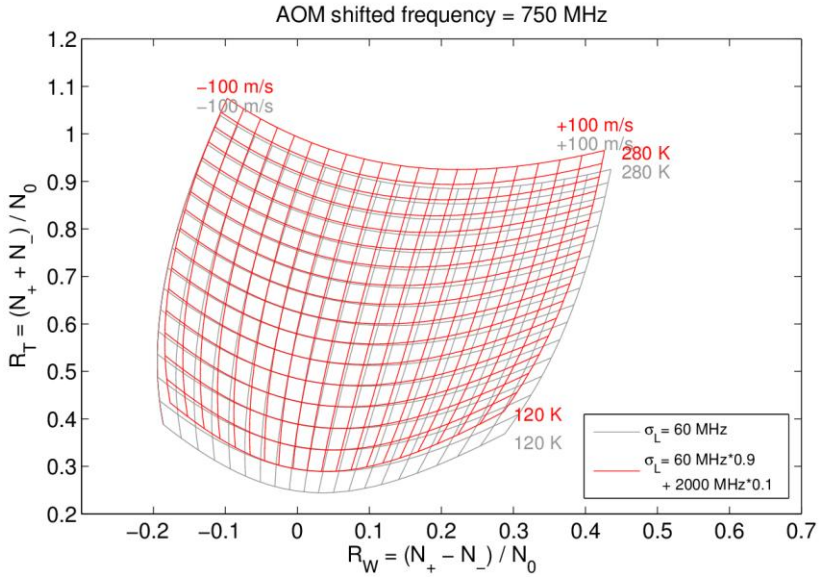

Figure 5.9. Calibration curves with mix of two Gaussian profiles with RMS linewidths of 60 MHz and 2000 MHz (red, the intensity ratio is 0.9:0.1) and the original (gray, same as Figure 5.4).

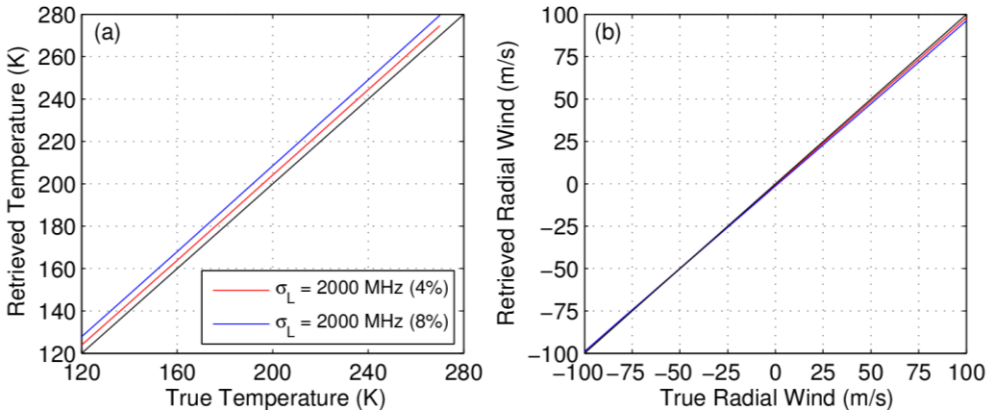

Figure 5.10. Temperature and radial wind values under two different intensity ratios of Gaussian profiles with RMS linewidth 60 MHz and 2000 MHz. 4% (8%) is the relative intensity of the Gaussian profile with RMS linewidth of 2000 MHz, which corresponds to the Gaussian profile with RMS linewidth of 60 MHz with relative intensity 96% (92%). The radial wind is fixed at 0 m/s in (a), and temperature is fixed at 200 K in (b).

In the second case, the PDA pulse spectrum is deformed and is asymmetric but we still assume that the pulse spectrum can be decomposed into two Gaussian profiles. Furthermore, we assume that the two Gaussian profiles have the same RMS linewidth of 60 MHz but with different center frequencies. Figure 5.11 shows the calibration curve (red) with the mix of the two profiles. One is the original Gaussian profile centered at the Na D_{2a} absorption peak and the other is shifted by -100 MHz relative to Na D_{2a} absorption peak; the peak intensity ratio of the former to latter Gaussian profile is 0.9:0.1. The curve is shifted toward the right comparing with the original one, indicating that the radial winds become more positive, and the temperatures seem do not have an obvious change.

Figure 5.12 shows the temperature and radial wind differences between the true and retrieved values with the fixed radial wind and temperature, respectively, under two different relative intensity ratios of the Gaussian profile centered at Na D_{2a} absorption peak and the Gaussian profile with center frequency shifted by -100 MHz. Both Gaussian profiles have the same RMS linewidth of 60 MHz. The two relative intensities are 4% and 8% of the frequency shifted Gaussian profiles, which correspond to Gaussian profiles centered at Na D_{2a} absorption peak with relative intensities equal to 96% and 92%, respectively. The radial wind difference increases as the portion of the shifted Gaussian profile increases, and the changes of temperature are relatively small. The temperature changes about 0.1 K per 1% change of the intensity ratio, and the wind changes about 0.6 m/s per 1% change of the intensity ratio.

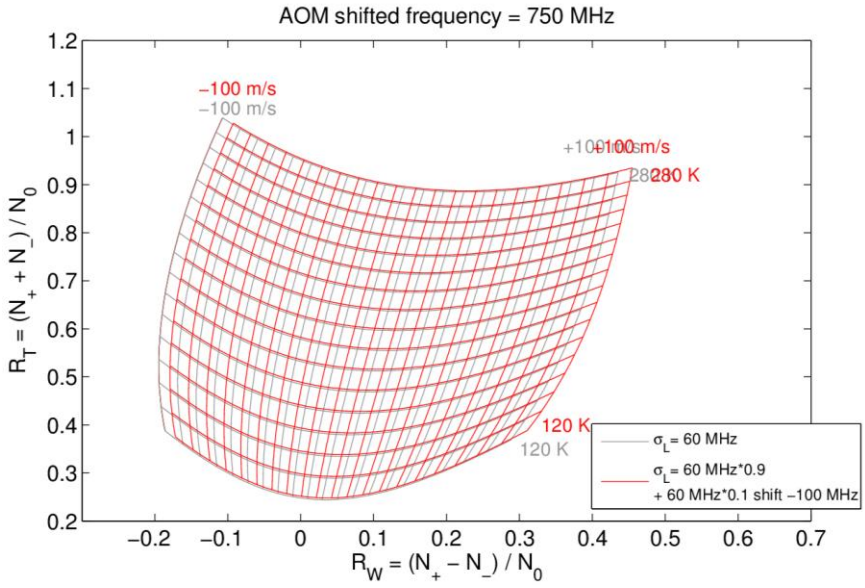

Figure 5.11. Calibration curves with mix of two Gaussian profiles with central frequencies that differ by 100 MHz (red, the intensity ratio is 0.9:0.1) and the original (gray, same as Figure 5.4). See text for details.

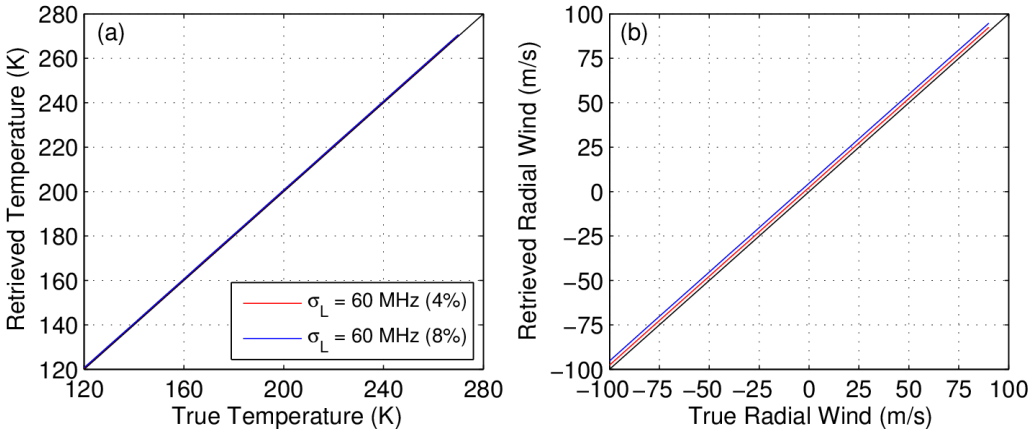

Figure 5.12. Temperature and radial wind values under two different intensity ratios of two Gaussian profiles (same RMS linewidth of 60 MHz) with one centered at Na D_{2a} absorption peak and one with center frequency shifted by -100 MHz. 4% (8%) in the legend is the relative intensity of the Gaussian profile with center frequency shifted by -100 MHz, which corresponds to the Gaussian profile centered at Na D_{2a} absorption peak with relative intensity 96% (92%). Radial wind is fixed at 0 m/s in (a), and temperature is fixed at 200 K in (b).

5.3.4 Combining PMT Non-linear and Lidar Pulse Spectra Effects

From section 5.3.1 to section 5.3.3, we examined the uncertainties of the temperature and radial wind caused by the PMT non-linear effect or the lidar pulse spectra individually. It is of interest to us to see how the uncertainties of the temperature and radial wind would be if the PMT non-linear effect and the lidar pulse spectra are considered at the same time. In this section, we exam three different scenarios with the PMT non-linear effect combining individually the three scenarios of lidar pulse spectra described in section 5.3.2 and section 5.3.3.

For the first scenario, we consider the PMT non-linear effect adds the wider lidar pulse RMS linewidth. Figure 5.13 shows the temperature and radial wind differences between the true and retrieved values with the fixed radial wind and temperature, respectively, under different RMS linewidths and PMT saturation coefficients. In Figure 5.13, the thin solid lines are different lidar pulse RMS linewidths without considering PMT saturation effect. In other words, the thin solid lines shown here are similar to the results shown in Figure 5.8 except that the values of $\Delta\sigma_L$ are different; as concluded from Figure 5.8, the temperature differences increase as $\Delta\sigma_L$ increases, and changes of radial wind are almost negligible. The dashed lines in Figure 5.13 are considering the PMT saturation effect with coefficient a = 0.9, where the coefficient a is defined in equations (5.3.1) and (5.3.2). By comparing Figure 5.13a with Figure 5.6a and Figure 5.8a, it can be seen that the dash lines in Figure 5.13a are basically the linear superposition of the PMT non-linear effect shown in Figure 5.6a and lidar pulse RMS linewidth effect shown in Figure 5.8a.

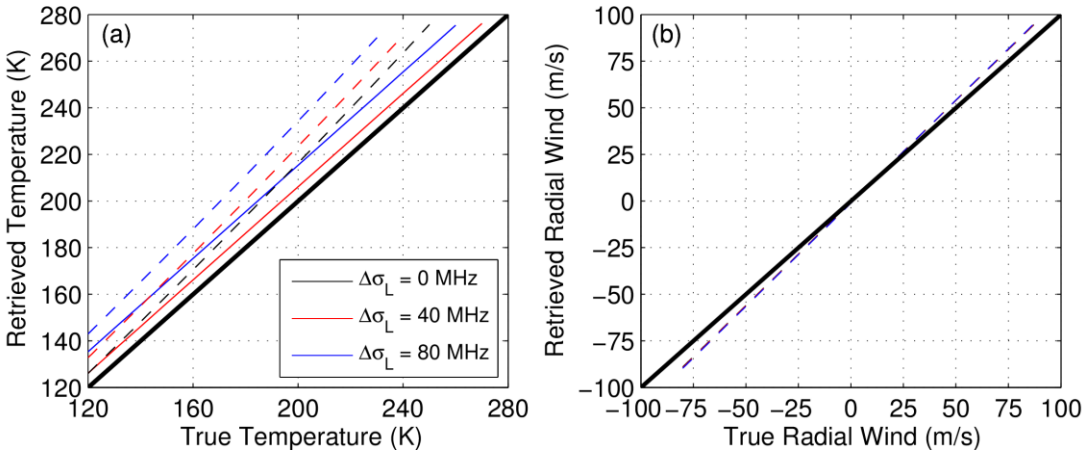

Figure 5.13. Temperature and radial wind values under different values of the PMT saturation coefficient a and lidar pulse RMS linewidths. The thin solid lines are different lidar pulse RMS linewidths without PMT saturation effect (a = 1). The dashed lines are with PMT saturation coefficient a = 0.9. Here $\Delta\sigma_L$ is the difference between the assumed RMS linewidth and the ideal RMS linewidth 60 MHz. The radial wind is fixed at 0 m/s in (a), and temperature is fixed at 200 K in (b).

For the second and the third scenario, we consider the PMT non-linear effect with the deformed but still symmetric lidar pulse shape and the PMT non-linear effect with the deformed and asymmetric lidar pulse shape, respectively. The parameters of the lidar pulse shape used in this section are exactly the same as described in section 5.3.3. Figure 5.14 and Figure 5.15 shows the results of the two scenarios, respectively. Similar to what we found in the first scenario, the temperature and radial wind measurement changes can be estimated as the linear superposition of the PMT non-linear effect shown in Figure 5.6 and the corresponding lidar pulse shape effects shown in Figure 5.10 and Figure 5.12. The temperature and radial wind changes from the three scenarios discussed in this section are calculated and summarized in Table 5.1. The results from section 5.3.1 to 5.3.3 are also listed in Table 5.1 for reference.

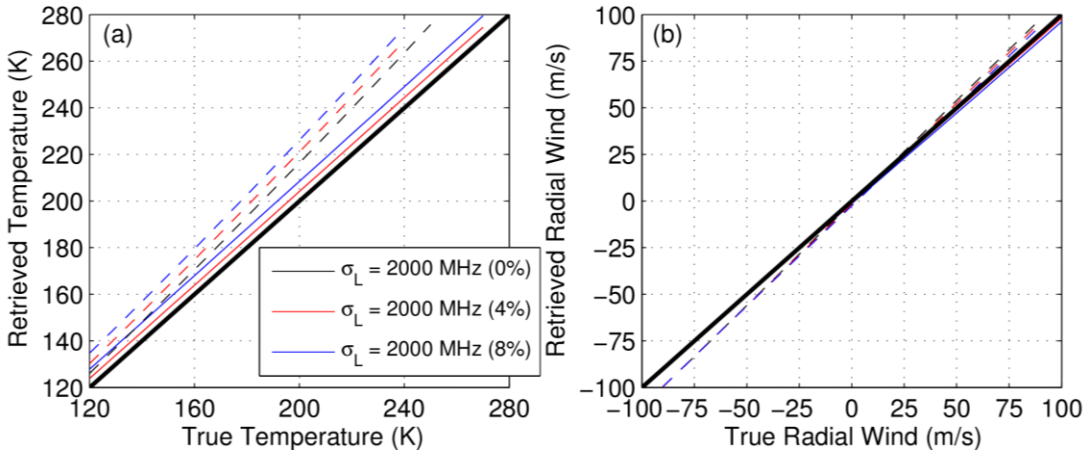

Figure 5.14. Temperature and radial wind values under different values of the PMT saturation coefficient *a* and different intensity ratios of Gaussian profiles with RMS linewidth 60 MHz and 2000 MHz. The thin solid lines are different lidar pulse RMS linewidths without PMT saturation effect (a = 1). The dashed lines are with PMT saturation coefficient a = 0.9. 4% (8%) is the relative intensity of the Gaussian profile with RMS linewidth of 2000 MHz, which corresponds to the Gaussian profile with RMS linewidth of 60 MHz with relative intensity 96% (92%). The radial wind is fixed at 0 m/s in (a), and temperature is fixed at 200 K in (b).

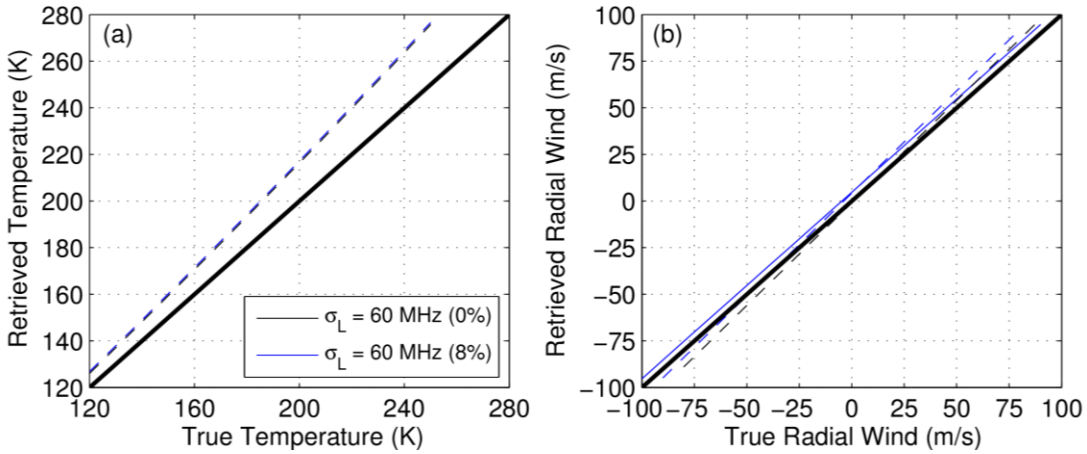

Figure 5.15. Temperature and radial wind values under different values of the PMT saturation coefficient *a* and different intensity ratios of two Gaussian profiles (same RMS linewidth of 60 MHz) with one centered at Na D_{2a} absorption peak and one with center frequency shifted by -100 MHz. 8% (0%) in the legend is the relative intensity of the Gaussian profile with center frequency shifted by -100 MHz, which corresponds to the Gaussian profile centered at Na D_{2a} absorption peak with relative intensity 92% (100%). Radial wind is fixed at 0 m/s in (a), and temperature is fixed at 200 K in (b).

Table 5.1. Summary of temperature and radial wind differences under different scenarios of PMT non-linear effect and lidar pulse spectra from section 5.3.1 to section 5.3.4.

Factors		add PMT saturation effect [a]
PMT saturation effect	ΔT = 1.6 K (T = 200 K) ΔT = 1.1 K (T = 160 K) ΔW = -0.12 m/s (W = 0 m/s) per 0.01 change of coefficient a (section 5.3.1)	/
Lidar pulse RMS linewidth	ΔT = 5.0 K (T = 200 K) ΔW = 0.01 m/s (W = 0 m/s) per 20 MHz change of RMS linewidth (section 5.3.2)	ΔT = 5.9 K (T = 200 K) ΔW = -0.06 m/s (W = 0 m/s) per 20 MHz change of RMS linewidth (section 5.3.4)
Lidar pulse lineshape is deformed but symmetric (60 MHz + 2000 MHz)	ΔT = 1.2 K (T = 200 K) ΔT = 1.1 K (T = 160 K) ΔW = -0.20 m/s (W=0 m/s) per 1% change of intensity ratio (section 5.3.3)	ΔT = 1.4 K (T = 200 K) ΔT = 1.3 K (T = 160 K) ΔW = -0.23 m/s (W=0 m/s) per 1% change of intensity ratio (section 5.3.4)
Lidar pulse lineshape is deformed and asymmetric (60 MHz centered at Na D_{2a} peak + 60 MHz shifted by -100 MHz)	ΔT = 0.08 K (T = 200 K) ΔW = 0.59 m/s (W = 0 m/s) per 1% change of intensity ratio (section 5.3.3)	ΔT = 0.10 K (T = 200 K) ΔW = 0.65 m/s (W = 0 m/s) per 1% change of intensity ratio (section 5.3.4)

[a] The PMT saturation coefficient a is assumed 0.9.

5.4 Discussion and Conclusions

We simulated different scenarios of PMT and lidar pulse spectra to assess the uncertainties introduced to the temperature and radial wind in this study. From the forward model results, both PMT non-linear effects and lidar pulse spectra can induce uncertainties into the temperature and radial wind measurements. From the previous discussion, the seeding condition of the Nd:YAG laser can largely influence the PDA output pulse spectrum. An unstable or poorly seeded Nd:YAG laser results in a pulse that is partially seeded and partially unseeded. Consequently, the PDA output pulse spectrum could contain a narrow Gaussian profile with a broad pedestal, which is similar to the first case of section 5.3.3; the case in which the PDA pulse spectrum is deformed and is comprised of two Gaussian profiles, one with a narrow RMS linewidth and one with a very large RMS linewidth. Figure 5.3 shows an example of the STAR lidar PDA output pulse measurements through optical heterodyne detection (OHD)

method. The details of OHD method could be found in many publications (e.g., *Chu and Papen* [2005]). As shown in the middle plot of Figure 5.3, the PDA pulse spectrum peak is centered at ~480 MHz and the spectrum shape obviously is not a single Gaussian profile. It contains both a narrow peak and a broad pedestal, for which the cause could be the imperfectly seeded Nd:YAG pulse.

Furthermore, in fact, when considering the PDA pulse spectrum in reality, there is an additional factor that needs to be taken into account: the PDA chirp. The definition of chirp is that a signal in which the frequency increases (up-chirp) or decreases (down-chirp) with time. For pulsed lasers such as PDA, the chirp sometimes can be a major issue leading to unpredictable frequency variations and offset, and it is challenging to measure the real frequency chirp due to the short pulse width in the time domain. The source of the PDA chirp is the time-dependent optical phase distortions predominantly caused by the time-dependent gain associated with the evolution of the pumping pulse irradiance [*Melikechi et al.*, 1994]. An example of the evolution of STAR lidar PDA chirp profile is also plotted in Figure 5.3 (right plot), which shows the up-chirp pattern of the pulse. Moreover, it could also be seen that the chirp profile is asymmetric and is biased to positive frequency (blue shift). This result implies that the PDA pulse spectrum is asymmetric and the spectrum peak deviates from the PDA seeding frequency. Such situation can be described by the second case in section 5.3.3; that is, the case in which the PDA pulse spectrum is deformed and asymmetric but can still be decomposed into two Gaussian profiles having the same RMS linewidth with different center frequencies.

At the beginning of this chapter, an example of temperature and radial wind observed by the STAR lidar is illustrated in Figure 5.2. From the forward modeling results, a concern is actually raised whether the short period structures shown in Figure 5.2 are real phenomena or the non-linear response and short-term variability of the instruments. We compared the time series of

temperature and vertical wind and found correlation between the two measurements. Plotted in Figure 5.16 is an example of the time series at the altitude of 91.6 km. A positive correlation is clearly seen; that is, both temperature and wind tend to bias toward the same direction simultaneously. The estimated short-term variability of temperature is ~2.5 K, and of radial wind is ~1.6 m/s in Figure 5.16. From the forward model results obtained in section 5.3, under certain scenarios, temperature and radial wind can fluctuate in the same direction, which can induce positive correlations between temperature and wind perturbations.

Overall, in this chapter, we used the forward model method to calculate the temperature and radial wind uncertainties induced by simplified cases of the PMT unaccounted non-linear response and distorted PDA output pulse spectrum. This forward model method has the capability to simulate most of the conditions of the PMT response and lidar pulse spectrum. The main goal here is to give a general idea of how temperature and radial wind depend on and vary with these parameters, and also provide a guideline when inspecting and calibrating the lidar instruments in the future. According to the results we obtained, for high-frequency wave and heat flux studies, measurement of the lidar pulse spectrum will be crucial in order to calibrate the temperature and radial wind, and we must consider the nonlinear effects of photon detection system when the signal levels are high.

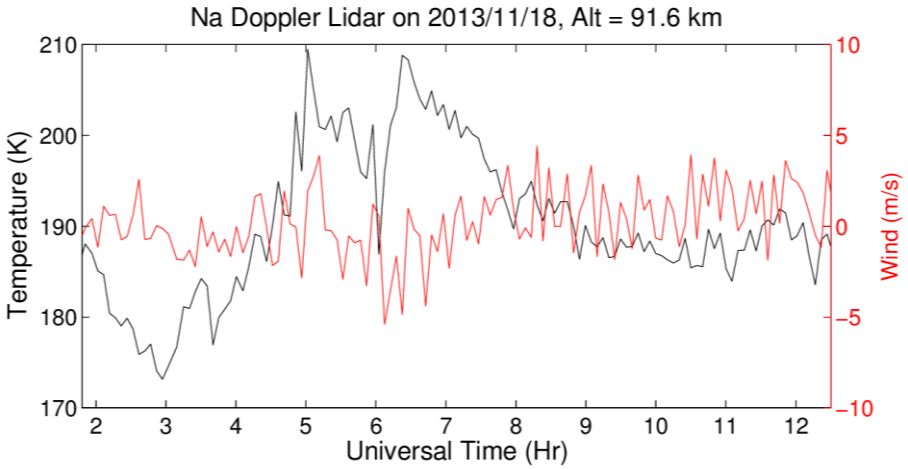

Figure 5.16. Time series of temperature and vertical wind measurements at 91.6 km from Figure 5.2.

CHAPTER 6

Conclusions and Future Outlook

6.1 Conclusions

The McMurdo lidar campaign has provided an invaluable data set and advanced our understandings of the polar middle and upper atmosphere, including the chemical processes and dynamics of the Fe layer and temperature structure. First is the discovery of the thermospheric neutral Fe layer [*Chu et al.*, 2011b], which opens a new avenue in thermospheric wave dynamics and chemistry processes studies, and also has triggered several observations of thermospheric events at other lidar stations. The paper by *Chen et al.* [2013] and *Lu et al.* [2013] present the observations of strong inertia gravity waves (IGW) in the MLT region and planetary waves (PW) in the stratopause region using this McMurdo lidar data. These two features are found to basically dominate the winter temperature variation at McMurdo. In this dissertation, we further provide the observation results of the winter temperature tides covering altitude range of 30 to 110 km. The winter temperature diurnal and semidiurnal tidal amplitude is small below 100 km (less than 3 K), but interestingly the amplitudes grow quickly with altitude above 100 km. Moreover, we also found that the larger growth rate of diurnal tidal amplitude above 100 km corresponding to larger Kp index.

The winter tides study has been extended to the lower thermosphere with the help of the CTIPe model. According the CTIPe model results, we suggest that the fast growth of the diurnal tidal amplitude in the lower thermospheric polar region is due to the adiabatic effect induced by the Hall ion drag. Since the Hall ion drag is in the direction of the electric field, it tends to

produce increased pressure where the electric field is convergent and decreased pressure where the field is divergent. In other words, the increase of pressure corresponds to an elevated temperature where electric field converges and vice versa. On the other hand, the Joule heating has minor distribution to the diurnal tides due to the counteraction by Joule-heating-induced adiabatic heating. The CTIPe model results also demonstrate the Kp dependence of the induced diurnal tidal amplitudes because of that the ion drag forcing becomes larger under more disturbed conditions due to the increased conductivities and electric field strengths.

Our McMurdo lidar campaign so far has covered wide range of wave spectrum in the winter middle and upper atmosphere. The understandings of theses waves then become a solid base for forming the first temperature climatology presented in this dissertation. With the knowledge of the wave activities, including IGW, PW, and tides above McMurdo gained from the previous studies, we have gained better ideas on the possible factors that may bias the background mean temperature. Also, with the extensive data set the McMurdo lidar campaign has been collected so far, we are confident with the first temperature climatology derived from over 4000 hours of lidar data. Comparing with lidar data collected in other Antarctica stations in the past few decades, the data set presented here is the most extensive one so far. The temperature climatology presented in this dissertation provides the ground truth for satellite observations, new critical data for improving empirical models such as MSISE-00, and also serves as the baseline for measurements decades from now to compare with in order to assess/monitor climate change.

The Boltzmann lidar is a relatively broadband system comparing with the Doppler lidar system. The broad linewidth of the lidar pulses prevent the system providing wind measurement in the MLT region, which is also an important parameter for the atmospheric dynamics. Therefore, we foresee that using the Doppler lidar systems would be the trend in the future for

middle and upper atmosphere observations. Despite the fact that the Doppler lidar systems have several advantages such as high signal to noise ratio and additional wind measurements, the calibration of the Doppler system is very crucial and complicated. In this dissertation, we simulate the effects on the temperature and wind measurements caused by the instabilities of lidar pulse spectrum and the non-linear effect of receiver detecting system. From the simulation results, we found that the Gaussian profile distortion of the lidar pulse spectrum causes significant short-term variability in the temperature and radial wind measurements. Under certain scenarios, temperature and radial wind can fluctuate in the same direction, which induces positive correlations between temperature and radial wind perturbations. Therefore, if lidar pulse spectrum is not as stable as we hoped, real-time monitoring of pulse spectra is necessary for calibrating the temperature and radial wind measurements. Further studies on this forward modeling are needed for the combined cases, e.g., PMT and discriminator saturation under asymmetric pulse shape.

6.2 Future Outlook

The modern Boltzmann and Doppler lidars are one of the best tools to explore the space-atmosphere interaction region and also provide high quality measurements to monitor climate change. In the near future, with the possible new Doppler lidar system at McMurdo, we might be able to explore the wave dynamics in the summer season and also extend the observations range to even higher altitudes. In combination with the newly-implemented high efficiency receiver design presented in *Smith and Chu* [2015], we can further study the high-frequency dynamics and heat flux at the polar region. Furthermore, if very large aperture receivers (like OASIS or VLAHP) can be used with these modern Doppler lidars, such as the Fe and Na Doppler lidars,

temperature and wind measurement ranges can be largely extended, especially into the region between 110 and 200 km, for which is one of the least understood regions of the Earth's atmosphere and is now one of the most desired regions to explore of the atmosphere and geospace community.

With the improved lidar signal levels, it is possible to routinely measure neutral metal densities, temperature and wind up to 150 km or higher. New features or processes may be discovered with such new capabilities, especially if the lidar observations are combined with complementary measurements of ionosphere and magnetosphere. The observation of thermospheric Fe layers extending to ~170 km by the McMurdo lidar campaign was an exciting example for the new discovery [*Chu et al.*, 2011b]. The discovery has radically changed the view on the extension range of the neutral atoms and hint at their source [*Friedman et al.*, 2013], and it further leads to the development of a thermospheric Fe/Fe^+ model for the polar regions [*Yu and Chu*, 2015].

Lastly, regarding temperature climatology, it is crucial to understand how various processes could affect the mean temperatures. So far, from the lidar observations, we have gained knowledge of the IGW, PW, and tides above McMurdo, however, for examples, the effects of inter-hemispheric coupling and the effects of geomagnetic activities above 100 km still remain unclear. Above 100 km, this is the region that contains the largest sources and sinks of radiative and magnetospheric energy in the ionosphere-thermosphere system. During geomagnetic storms, direct auroral particle heating and Joule heating can deposit considerable amount of energy into the lower thermosphere and heat up the neutral atmosphere, which could be critical factors when calculating the temperature climatology in the polar region. Therefore, by advancing the knowledge of these unknown issues, we can get better handles on the climate change and trend studies in the future.

Bibliography

Aikin, A. C., M. L. Chanin, J. Nash, and D. J. Kendig (1991), Temperature trends in the lower mesosphere, *Geophys. Res. Lett.*, *18*, 461–419.

Akmaev, R. A., and V. I. Fomichev (1998), Cooling of the mesosphere and lower thermosphere due to doubling of CO2, *Ann. Geophys.*, *16*, 1501–1512.

Akmaev, R. A., and V. I. Fomichev (2000), A model estimate of cooling in the mesosphere and lower thermosphere due to the CO_2 increase over the last 3–4 decades, *Geophys. Res. Lett.*, *27*, 2113–2116.

Akmaev, R. A. (2011), Whole atmosphere modeling: Connecting terrestrial and space weather, *Rev. Geophys.*, *49*, RG4004, doi:10.1029/2011RG000364.

Akmaev, R. A., T. J. Fuller-Rowell, F. Wu, J. M. Forbes, X. Zhang, A. F. Anghel, M. D. Iredell, S. Moorthi, and H.-M. Juang (2008), Tidal variability in the lower thermosphere: Comparison of Whole Atmosphere Model (WAM) simulations with observations from TIMED, *Geophys. Res. Lett.*, *35*, L03810, doi:10.1029/2007GL032584.

Alexander, S. P., and M. G. Shepherd (2010), Planetary wave activity in the polar lower stratosphere, Atmos. Chem. Phys., 10, 707-718, doi:10.5194/acp-10-707-2010.

Andrews, D. G., J. R. Holton, and C. B. Leovy (1987), Middle Atmosphere Dynamics, Academic Press, San Diego.

Angelats i Coll, M., and J. M. Forbes (2002), Nonlinear interactions in the upper atmosphere: The s = 1 and s = 3 nonmigrating semidiurnal tides, *J. Geophys. Res.*, *101*(A7), 10.1029/2001JA900179.

Angell, J. K. (1991), Stratospheric temperature change as a function of height and sunspot number during 1972-89 based on rocketsonde and radiosonde data. *J. Clim.*, *4*, 1170–1180.

Arnold, K. S., and C. Y. She (2003), Metal fluorescence lidar (light detection and ranging) and the middle atmosphere, *Contemp. Phys.*, *44*(1), 35–49.

Avery, S. K., R. A. Vincent, A. Phillips, A. H. Manson, and G. J. Fraser (1989), High-latitude tidal behavior in the mesosphere and lower thermosphere, *J. Atmos. Terr. Phys.*, *51*, 595–608, doi:10.1016/0021-9169(89)90057-3.

Azeem, S. M. I., and G. G. Sivjee (2009), Multiyear observations of tidal oscillations in OH M(3,1) rotational temperatures at South Pole, Antarctica, *J. Geophys. Res.*, *114*, A06312, doi:10.1029/2008JA013976.

Bailey, G. J. (1983), The effect of a meridional E x B drift on the thermal plasma at L = 1.4, *Planet. Space Sci.*, *31*, 389–409, doi:10.1016/0032-0633(83)90154-X.

Baumgaertner, A. J. G., A. J. McDonald, G. J. Fraser, and G. E. Plank (2005), Long-term observations of mean winds and tides in the upper mesosphere and lower thermosphere above Scott Base, Antarctica, *J. Atmos. Sol. Terr. Phys.*, *67*, 1480–1496, doi:10.1016/j.jastp.2005.07.018.

Baumgaertner, A. J. G., M. J. Jarvis, A. J. McDonald, and G. J. Fraser (2006), Observations of the wavenumber 1 and 2 components of the semi-diurnal tide over Antarctica, *J. Atmos. Sol. Terr. Phys.*, 68, 1195–1214.

Best, N., R. Havens, and H. LaGow (1947), Pressure and temperature of the atmosphere to 120 km, *Phys. Rev.*, *71*(12), 915.

Burns, G. B., W. J. R. French, P. A. Greet, F. A. Philips, P. F. B. Williams, K. Finlayson, and G. Klich (2002), Seasonal variations and inter-year trends in 7 years of hydroxyl airglow rotational temperatures at Davis Station (69S, 78E), Antarctica, *J. Atmos. Sol. Terr. Phys.*, *64*, 1167–1174.

Burns, G. B., T. D. Kawahara, W. J. R. French, A. Nomura, and A. R. Klekociuk (2003), A comparison of hydroxyl rotational temperatures from Davis (69°S, 78°E) with sodium lidar temperatures from Syowa (69°S, 39°E), *Geophys. Res. Lett.*, *30*(1), 1025, doi:10.1029/2002GL016413.

Bills, R. E., and C. S. Gardner (1990), Lidar observations of mesospheric Fe and sporadic Fe layers at Urbana, Illinois, *Geophys. Res. Lett.*, *17*, 143–146.

Bowman, M. R., A. J. Gibson, and M. C. W. Sandford (1969), Atmospheric sodium measured by a tuned laser radar, *Nature*, *221*, 456–457.

CEDAR: The New Dimension, Strategic Vision for the NSF Program on Coupling, Energetics and Dynamics of Atmospheric Regions, May 2011.

Chapman, S., and R. S. Lindzen (1970), *Atmospheric Tides: Thermal and Gravitational*, 200 pp., Gordon and Breach, New York.

Chen, C., X. Chu, A. J. McDonald, S. L. Vadas, Z. Yu, W. Fong and X. Lu (2013), Inertia-gravity waves in Antarctica: A case study using simultaneous lidar and radar measurements at McMurdo/Scott Base (77.8°S, 166.7°E), *J. Geophys. Res. Atmos.*, *118*, 2794–2808, doi:10.1002/jgrd.50318.

Chu, X., W. Pan, G. Papen, C. S. Gardner, G. Swenson, and P. Jenniskens (2000), Characteristics of Fe ablation trails observed during the 1998 Leonid meteor shower, *Geophys. Res. Lett.*, *27*, 1807–1810.

Chu, X., G. Papen, W. Pan, C. S. Gardner, and J. Gelbwachs (2002), Fe Boltzmann temperature lidar: Design, error analysis, and first results from the North and South poles, *Appl. Opt.*, *41*, 4400–4410.

Chu, X., C. S. Gardner, and R. G. Roble (2003), Lidar studies of interannual, seasonal and diurnal variations of polar mesospheric clouds at the South Pole, *J. Geophys. Res.*, *108*(D8), 8447, doi: 10.1029/2002JD002524.

Chu, X., G. J. Nott, P. J. Espy, C. S. Gardner, J. C. Diettrich, M. A. Clilverd, and M. J. Jarvis (2004), Lidar observations of polar mesospheric clouds at Rothera, Antarctica (67.5°S, 68.0°W), *Geophys. Res. Lett.*, *31*, L02114, doi:10.1029/2003GL018638.

Chu, X., and G. Papen (2005), Resonance fluorescence lidar for measurements of the middle and upper atmosphere, in *Laser Remote Sensing*, edited by T. Fujii and T. Fukuchi, pp. 179–432, CRC Press, Boca Raton, Fla.

Chu, X., P. J. Espy, G. J. Nott, J. C. Diettrich, and C. S. Gardner (2006), Polar mesospheric clouds observed by an iron Boltzmann lidar at Rothera (67.5°S, 68.0°W), Antarctica from 2002 to 2005: Properties and implications, *J. Geophys. Res.*, *111*, D20213, doi:10.1029/2006JD007086.

Chu, X. and W. Huang (2010), Fe Doppler-Free Spectroscopy and Optical Heterodyne Detection for Accurate Frequency Control of Fe-Resonance Doppler Lidar, Proceeding of the 25th International Laser Radar Conference, pp. 969–972, St. Petersburg, Russia, 4–9 July 2010.

Chu, X., W. Huang, J. P. Thayer, Z. Wang, and J. A. Smith (2010), Progress in MRI Fe-resonance/Rayleigh/Mie Doppler lidar, Proceeding of the 25th International Laser Radar Conference, St. Petersburg, Russia, 4–9 July 2010.

Chu, X., W. Huang, W. Fong, Z. Yu, Z. Wang, J. A. Smith, and C. S. Gardner (2011a), First lidar observations of polar mesospheric clouds and Fe temperatures at McMurdo (77.8°S, 166.7°E), Antarctica, *Geophys. Res. Lett.*, *38*, L16810, doi:10.1029/2011GL048373.

Chu, X., Z. Yu, C. S. Gardner, C. Chen, and W. Fong (2011b), Lidar observations of neutral Fe layers and fast gravity waves in the thermosphere (110–155 km) at McMurdo (77.8°S, 166.7°E), Antarctica, *Geophys. Res. Lett.*, *38*, L23807, doi:10.1029/2011GL050016.

Codrescu, M. V., T. J. Fuller-Rowell, V. Munteanu, C. F. Minter, and G. H. Millward (2008), Validation of the Coupled Thermosphere Ionosphere Plasmasphere Electrodynamics model: CTIPE-Mass Spectrometer Incoherent Scatter temperature comparison, *Space Weather*, *6*, S09005, doi:10.1029/2007SW000364.

Collins, R. L., K. P. Bowman, and C. S. Gardner (1993), Polar stratospheric clouds at the South Pole in 1990: Lidar observations and analysis, *J. Geophys. Res.*, *98*, 1001–1010.

Collins, R. L., J. Li, and C. M. Martus(2015), First lidar observation of themesospheric nickel layer, *Geophys. Res.Lett.*, *42*, 665– 671, doi:10.1002/2014GL062716.

Day, K. A., R. E. Hibbins, and N. J. Mitchell (2011), Aura MLS observations of the westward-propagating s = 1, 16-day planetary wave in the stratosphere, mesosphere and lower thermosphere, *Atmos. Chem. Phys.*, *11*, 4149–4161, doi:10.5194/acp-11-4149-2011.

DeLand, M. T., E. T. Shettle, G. E. Thomas, and J. J. Olivero (2006), Aquarter-century of satellite polar mesospheric cloud observations, *J. Atmos.Sol. Terr. Phys.*, *68*(1), 9–29.

Di Donfrancesco, G., A. Adriani, G. P. Gobbi, and F. Congeduti (1996), Lidar observations of stratospheric temperature above McMurdo Station, Antarctica, *J. Atmos. Terr. Phys.*, *58*, 1391– 1399.

Di Liberto, L., F. Cairo, F. Fierli, G. Di Donfrancesco, M. Viterbini, T. Deshler, and M. Snels (2014), Observation of polar stratospheric clouds over McMurdo (77.85°S, 166.67°E) (2006–2010), *J. Geophys. Res. Atmos.*, *119*, 5528–5541, doi:10.1002/2013JD019892.

Duck, T. J., J. A. Whiteway, and A. I. Carswell (1998), Lidar observations of gravity wave activity and Arctic stratospheric vortex core warming, *Geophys. Res. Lett.*, *25*, 2813– 2816.

Duck, T. J., J. A. Whiteway, and A. I. Carswell (2001), The gravity wave-Arctic stratospheric vortex interaction, *J. Atmos. Sci*., *58*, 3581–3596.

Ekanayake, E. M. P., T. Aso, and S. Miyahara (1997), Background wind effect on propagation of nonmigrating diurnal tides in the middle atmosphere, *J. Atmos. Terr. Phys.*, *59*, 401–429.

Eyring, V., et al. (2013), Long-term ozone changes and associated climate impacts in CMIP5 simulations, *J. Geophys. Res. Atmos.*, *118*, 5029–5060, doi:10.1002/jgrd.50316.

Espy, P. J., G. O. L. Jones, G. R. Swenson, J. Tang, and M. J. Taylor (2004), Seasonal variations of the gravity wave momentum flux in the Antarctic mesosphere and lower thermosphere, *J. Geophys. Res.*, *109*, D23109, doi:10.1029/2003JD004446.

Felix, F.,W. Keenliside, G. Kent, and M. C. W. Sandford (1973), Laser radar observations of atmospheric potassium, *Nature*, *246*, 345–346.

Fesen, C. G., R. G. Roble, E. C. Ridley (1991), Thermospheric tides at equinox: Simulations with coupled composition and auroral forcings, 1, Diurnal component, *J. Geophys. Res.*, *96*, 3647–3661.

Fesen, C. G., A. D. Richmond, and R. G. Roble (1993), Theoretical effects of geomagnetic activity on thermospheric tides, *J. Geophys. Res.*, *98*(A9), 15599–15612, doi:10.1029/93JA01188.

Fesen, C. G. (1997), Geomagnetic activity effects on thermospheric tides: A compendium of theoretical predictions, *J. Atmos. Sol. Terr. Phys*., *59*, 785–803.

Fong, W., X. Lu, X. Chu, T. J. Fuller-Rowell, Z. Yu, B. R. Roberts, C. Chen, C. S. Gardner, and A. J. McDonald (2014), Winter temperature tides from 30 to 110 km at McMurdo (77.8°S, 166.7°E), Antarctica: Lidar observations and comparisons with WAM, *J. Geophys. Res. Atmos.*, *119*, doi:10.1002/2013JD020784.

Fong, W., X. Chu, X. Lu, C. Chen, T. J. Fuller-Rowell, M. Codrescu, and A. D. Richmond (2015), Lidar and CTIPe model studies of the fast amplitude growth of the diurnal temperature ‘tides’ in the Antarctic winter lower thermosphere and relationship with the aurora, *Geophys. Res. Lett.*, *42*, doi: 10.1002/2014GL062784.

Forbes, J. M., and M. E. Hagan (1979), Tides in the joint presence of friction and rotation: An f plane approximation, *J. Geophys. Res.*, *84*(A3), 803–810.

Forbes, J. M. (1982a), Atmospheric tides: 1. Model description and results for the solar diurnal component, *J. Geophys. Res.*, *87*(A7), 5222–5240.

Forbes, J. M. (1982b), Atmospheric tides: 2. The solar and lunar semidiurnal components, *J. Geophys. Res.*, *87*(A7), 5241–5252.

Forbes, J. M., and H. B. Garrett (1979), Theoretical studies of atmospheric tides, *Rev. Geophys. Space Phys.*, *17*, 1951–1981.

Forbes, J. M. (1995), Tidal and Planetary Waves, *Geophys. Monograph.*, *87*, 67–87.

Forbes, J. M., N. A. Makarov, and Y. I. Portnyagin (1995), First results from meteor radar at South Pole: A large 12–hour oscillation with zonal wavenumber one, *Geophys. Res. Lett.*, *22*, 3247–3250, doi:10.1029/95GL03370.

Forbes, J. M., S. E. Palo, and X. Zhang (2000), Variability of the ionosphere, *J. Atmos. Sol. Terr. Phys*., *62*, 685–693.

Forbes, J. M., and D. Wu (2006), Solar tides as revealed by measurements of mesosphere temperature by the MLS experiment on UARS, *J. Atmos. Sci*., 63, 1776–1797.

Forbes, J. M., X. Zhang, S. Palo, J. Russell, C. J. Mertens, and M. Mlynczak (2008), Tidal variability in the ionospheric dynamo region, *J. Geophys. Res., 113*, A02310, doi:10.1029/2007JA012737.

France, J. A., V. L. Harvey, C. E. Randall, M. H. Hitchman, and M. J. Schwartz (2012), A climatology of stratopause temperature and height in the polar vortex and anticyclones, *J. Geophys. Res.*, *117*, D06116, doi:10.1029/2011JD016893.

Fricke, K. H., and U. von Zahn (1985), Mesopause temperatures derived from probing the hyperfine structure of the D_2 resonance line of sodium by lidar, *J. Atmos. Terr. Phys.*, *47*, 499–512.

Fritts, D. C., and R. A. Vincent (1987), Mesospheric momentum flux studies at Adelaide, Australia-Observations and a gravity wave-tidal interaction model, *J. Atmos. Sci.*, *44*, 605–619.

Fuller-Rowell, T. J., and D. Rees (1980), A three dimensional time-dependant global model of the thermosphere, *J. Atmos. Sci.*, *37*, 2545–2567.

Fuller-Rowell, T. J., D. Rees, H. F. Parish (1991), Lower thermosphere coupling study: Comparison of observations with predictions of the University College London-Sheffield thermosphere-ionosphere model, *J. Geophys. Res*., *96*, 1181–1202, doi:10.1029/90JA02315.

Fuller-Rowell, T. J., G. H. Millward, A. D. Richmond, and M. V. Codrescu (2002), Storm-time changes in the upper atmosphere at low latitudes, *J. Atmos. Sol. Terr. Phys.*, *64*, 1383–1391, doi:10.1016/ S1364-6826(02)00101-3.

Fuller-Rowell, T. J., et al. (2008), Impact of terrestrial weather on the upper atmosphere, *Geophys. Res. Lett.*, *35*, L09808, doi:10.1029/2007GL032911.

Fuller-Rowell, T., F. Wu, R. Akmaev, T.-W. Fang, *and* E. Araujo-Pradere (2010), A whole atmosphere model simulation of the impact of a sudden stratospheric warming on thermosphere dynamics and electrodynamics, *J. Geophys. Res.*, *115*, A00G08, doi:10.1029/2010JA015524.

Fuller-Rowell, T., H. Wang, R. Akmaev, F. Wu, T.-W. Fang, M. Iredell, and A. Richmond (2011), Forecasting the dynamic and electrodynamic response to the January 2009 sudden stratospheric warming, *Geophys. Res. Lett.*, *38*, L13102, doi:10.1029/2011GL047732.

Garcia, R. R., and B. A. Boville (1994), "Downward control" of the mean meridional circulation and temperature distribution of the polar winter stratosphere, *J. Atmos. Sci.*, *51*, 2238–2245.

Gardner, C. S. (1989), Sodium resonance fluorescence lidar applications in atmospheric science and astronomy, *Proc. IEEE*, *77*, 408–418.

Gardner, C. S., G. C. Papen, X. Chu, and W. Pan (2001), First lidar observations of middle atmosphere temperatures, Fe densities, and polar mesospheric clouds over the North and South Poles, *Geophys. Res. Lett.*, *28*, 1199–1202.

Gardner, C. S., J. M. C. Plane, W. Pan, T. Vondrak, B. J. Murray, and X. Chu (2005), Seasonal variations of the Na and Fe layers at the South Pole and their implications for the chemistry and general circulation of the polar mesosphere, *J. Geophys. Res.*, *110*, D10302, doi: 10.1029/2004JD005670.

Gardner, C. S., X. Chu, P. J. Espy, J. M. C. Plane, D. R. Marsh, and D. Janches (2011), Seasonal variations of mesospheric Fe layers at Rothera, Antarctica (67.5°S, 68.0°W), *J. Geophys. Res.*, *116*, D02304, doi:10.1029/2010JD014655.

Gelbwachs, J. A. (1994), Iron Boltzmann factor LIDAR: proposed new remote-sensing technique for mesospheric temperature, *Appl. Opt.*, *33*, 7151–7156.

Gibson, A. J., L. Thomas, and S. K. Bhattachacharyya (1979), Laser observations of the ground-state hyperfine structure of sodium and of temperatures in the upper atmosphere, *Nature*, *281*, 131–132.

Gille, J. C., and F. B. House (1971), On the inversion of limb radiance measurements I: Temperature and thickness, *J. Atmos. Sci.*, *28*, 1427–1442.

Greet, P. A., J. Innis, and P. L. Dyson (1994), High-resolution Fabry-Perot observations of mesospheric OH (6-2) emissions, *Geophys. Res. Lett.*, *21*, 1153–1156.

Golitsyn, G. S., A. I. Semenov, N. N. Shefov, L. M. Fishkova, E. V. Lysenko, and S. P. Perov (1996), Long-term temperature trends in the middle and upper atmosphere, *Geophys. Res. Lett.*, *23*, 1741–1744.

Hagan, M. E., J. M. Forbes, and F. Vial, A numerical investigation of the propagation of the quasi 2-day wave into the lower thermosphere (1993), *J. Geophys. Res.*, *98*, 23,193– 23,205.

Hagan, M. E., J. M. Forbes, and F. Vial (1995), On modeling migrating solar tides, *Geophys. Res. Lett.*, *22*, 893–896, doi:10.1029/95GL00783.

Hagan, M. E., M. D. Burrage, J. M. Forbes, J. Hackney, W. J. Randel, and X. Zhang (1999), GSWM-98: Results for migrating solar tides, *J. Geophys. Res.*, *104*, 6813–6828, doi:10.1029/1998JA900125.

Hagan, M. E., and R. G. Roble (2001), Modeling diurnal tidal variability with the National Center for Atmospheric Research thermosphere-ionosphere-mesosphere-electrodynamics general circulation model, *J. Geophys. Res.*, *106*(A11), 24,869–24,882.

Hagan, M. E., and J. M. Forbes (2002), Migrating and nonmigrating tides in the middle and upper atmosphere excited by tropospheric latent heat release, *J. Geophys. Res.*, *107*(D24), 4754, doi:10.1029/2001JD001236.

Hagan, M. E., and J. M. Forbes (2003), Migrating and nonmigrating semidiurnal tides in the middle and upper atmosphere excited by tropospheric latent heat release, *J. Geophys. Res.*, 108(A2), 1062, doi:10.1029/2002JA009466.

Hauchecorne, A. and M. Chanin (1980), Density and temperature profiles obtained by lidar between 35 and 70 km, *Geophys. Res. Lett.*, *7*(8), 565–568, doi:10.1029/GL007i008p00565.

Hecht, J. H., R. L. Walterscheid, D. C. Firtts, J. R. Isler, D. C. Senft, C. S. Gardner, and S. J. Franke (1997), Wave breaking signatures in OH airglow and sodium densities and temperature 1. Airglow imaging, Na lidar, and MF radar observations, *J. Geophys. Res.*, *102*, 6655–6668.

Hernandez, G. (2003), Climatology of the upper mesosphere temperature above South Pole (90°S): Mesospheric cooling during 2002, *Geophys. Res. Lett.*, *30*(10), 1535, doi:10.1029/2003GL016887.

Hernandez, G., R. W. Smith, and J. F. Conner (1992), Neutral wind and temperature in the upper atmosphere above South Pole, Antarctica, *Geophys. Res. Lett.*, *19*, 53–56.

Hernandez, G., G. J. Fraser, and R. W. Smith (1993), Mesospheric 12-hour oscillation near South Pole, Antarctica, *Geophys. Res. Lett.*, *20*, 1787–1790.

Hibbins, R. E., O. J. Marsh, A. J. McDonald, and M. J. Jarvis (2010), Interannual variability of the S = 1 and S = 2 components of the semidiurnal tide in the Antarctic MLT, *J. Atmos. Sol. Terr. Phys.*, *72*, 794–800, doi:10.1016/j.jastp.2010.03.026.

Hitchman, M. H., J. C. Gille, C. D. Rodgers, and G. Brasseur (1989), The Separated Polar Winter Stratopause: A Gravity Wave Driven Climatological Feature, *J. Atmos. Sci.*, *46*(3), 410–422.

Höffner, J, and J. Lautenbach (2009), Daylight measurements of mesopause temperature and vertical wind with the mobile scanning iron lidar, *Opt. Lett.*, *34*, 1351–1353.

Holtan, J. R. (1975), *The Dynamic Meteorology of the Stratosphere and Mesosphere*, Meteor. Monog. 15(37), Amer. Met. Soc., MA.

Huang, W., X. Chu, C. S. Gardner, Z. Wang, W. Fong, J. A. Smith, and B. R. Roberts (2013), Simultaneous, common-volume lidar observations and theoretical studies of correlations among Fe/Na layers and temperatures in the mesosphere and lower thermosphere at Boulder Table Mountain (40°N, 105°W), Colorado, *J. Geophys. Res. Atmos.*, *118*, 8748–8759, doi:10.1002/jgrd.50670.

Immel, T. J., E. Sagawa, S. L. England, S. B. Henderson, M. E. Hagan, S. B. Mende, H. U. Frey, C. M. Swenson, and L. J. Paxton (2006), Control of equatorial ionospheric morphology by atmospheric tides, *Geophys. Res. Lett.*, *33*, L15108, doi:10.1029/2006GL026161.

IPCC – Intergovernmental Panel on Climate Change, Third Assessment Report – Climate Change 2001: The Scientific Basis, J. T. Houghton, Y. Ding, D. J. Griggs, M. Noguer, P. J. van der Linden, X. Dai.

Jegou, J.-P., M.-L. Chanin, G. Megie, and J. E. Blamont (1980), Lidar measurements of atmospheric lithium, *Geophys. Res. Lett.*, *7*, 995–998.

Kanzawa, H. (1989), Warm stratopause in the Antarctic winter, *J. Atmos. Sci.*, *46*, 435–438.

Kato, S., T. Tsuda, and F. Wanatabe (1982), Thermal excitation of nonmigrating tides, *J. Atmos. Terr. Phys.*, *44*, 131–146.

Kawahara, T. D., T. Kitahara, F. Kobayashi, Y. Saito, A. Nomura, C.-Y. She, and D. A. Krueger (2002), Wintertime mesopause temperatures observed by lidar measurements over Syowa Station (69°S, 39°E), Antarctica, *Geophys. Res. Lett.*, *29*(15), 1709, doi:10.1029/2002GL015244.

Kawahara, T. D., C. S. Gardner, and A. Nomura (2004), Observed temperature structure of the atmosphere above Syowa Station, Antarctica (69°S, 39°E), J. Geophys. Res., 109, D12103, doi:10.1029/2003JD003918.

Killeen, T. L., Q. Wu, S. C. Solomon, D. A. Ortland, W. R. Skinner, R. J. Niciejewski, and D. A. Gell (2006), TIMED Doppler Interferometer: Overview and recent results, *J. Geophys. Res.*, *111*, A10S01, doi:10.1029/2005JA011484.

Klekociuk, A. R., M. M. Lambert, R. A. Vincent, and A. J. Dowdy (2003), First year of Rayleigh lidar measurements of middle atmosphere temperatures above Davis, Antarctica, *Adv. Space Res.*, *32*, 771– 776.

Kwak, Y.-S., and A. D. Richmond (2007), An analysis of the momentum forcing in the high-latitude lower thermosphere, *J. Geophys. Res.*, *112*, A01306, doi:10.1029/2006JA011910.

Kwak, Y.-S., and A. D. Richmond (2014), Dependence of the high-latitude lower thermospheric wind vertical vorticity and horizontal divergence on the interplanetary magnetic field, *J. Geophys. Res. Space Physics*, *119*, 1356–1368, doi:10.1002/2013JA019589.

Lautenbach, J., and J. Höffner (2004), Scanning iron temperature lidar for mesopause temperature observation, *Appl. Opt.*, *43*, 4559–4563.

Lieberman, R. S., and C. B. Leovy (1995), A numerical model of nonmigrating diurnal tides between the surface and 65 km, *J. Atmos. Sci.*, *52*, 389–409.

Lindzen, R. S. (1970), Internal gravity waves in atmospheres with realistic dissipation and temperature I, Mathematical development and propagation of waves into the thermosphere, *Geophys Fluid Dyn.*, *1*, 303.

Lindzen, R. S. (1971), Atmospheric Tides, in *Mathematical Problems in the Geophysical Sciences: Inverse Problems, Dynamo Theory, and Tides, Lectures in Applied Mathematics*, vol. 14, W. H. Reid, AMS.

Liu, A. Z., R. G. Roble, J. H. Hecht, M. F. Larsen, and C. S. Gardner (2004), Unstable layers in the mesopause region observed with Na lidar during the Turbulent Oxygen Mixing Experiment (TOMEX) campaign, *J. Geophys. Res.*, *109*, D02S02, doi:10.1029/2002JD003056.

Liu, A. Z., X. Lu, and S. J. Franke (2013), Diurnal variation of gravity wave momentum flux and its forcing on the diurnal tide, *J. Geophys. Res. Atmos.*, *118*, doi:10.1029/2012JD018653.

Lowe, D., and A. R. MacKenzie (2008), Polar stratospheric cloud microphysics and chemistry, *J. Atmos. Sol. Terr. Phys.*, *70*, 13–40, doi:10.1016/j.jastp.2007.09.011.

Lu, X., A. Z. Liu, G. R. Swenson, T. Li, T. Leblanc, and I. S. McDermid (2009), Gravity wave propagation and dissipation from the stratosphere to the lower thermosphere, *J. Geophys. Res.*, *114*, D11101.

Lu, X., A. Z. Liu, J. Oberheide, Q. Wu, T. Li, Z. Li, G. R. Swenson, and S. J. Franke (2011), Seasonal variability of the diurnal tide in the mesosphere and lower thermosphere over Maui, Hawaii (20.7°N, 156.3°W), *J. Geophys. Res.*, *116*, D17103, doi:10.1029/2011JD015599.

Lu, X., X. Chu, T. Fuller-Rowell, L. Chang, W. Fong, and Z. Yu (2013), Eastward propagating planetary waves with periods of 1–5 days in the winter Antarctic stratosphere as revealed by MERRA and lidar, *J. Geophys. Res. Atmos.*, *118*, doi:10.1002/jgrd.50717.

Lübken, F.-J., and U. von Zahn (1991), Thermal structure of the mesopause region at polar latitudes, *J. Geophys. Res.*, *96*, 20841–20857, doi:10.1029/91JD02018.

Lübken, F.-J., M. J. Jarvis, and G. O. L. Jones (1999), First in situ temperature measurements at the Antarctic summer mesopause, *Geophys. Res. Lett.*, *26*, 3581–3584.

Lübken, F. J. (2000), Nearly zero temperature trend in the polar summer mesosphere, *Geophys. Res. Lett.*, *27*, 3603–3606.

Lübken, F. J. (2001), No long term change of the thermal structure in the mesosphere at high latitudes during summer, *Adv. Space. Res.*, *28*(7), 947–953.

Lübken, F.-J., A. Müllemann, and M. J. Jarvis (2004), Temperatures and horizontal winds in the Antarctic summer mesosphere, *J. Geophys. Res.*, *109*, D24112, doi:10.1029/2004JD005133.

Lübken, F.-J., J. Höffner, T. P. Viehl, B. Kaifler, and R. J. Morris (2011), First measurements of thermal tides in the summer mesopause region at Antarctic latitudes, *Geophys. Res. Lett.*, *38*, L24806, doi:10.1029/2011GL050045.

Lübken, F.-J., J. Höffner, T. P. Viehl, B. Kaifler, and R. J. Morris (2014), Winter/summer mesopause temperature transition at Davis (69°S) in 2011/2012, *Geophys. Res. Lett.*, *41*, 5233–5238, doi:10.1002/2014GL060777.

Maruyama, N., et al. (2007), Modeling storm-time electrodynamics of the low-latitude ionosphere–thermosphere system: Can long lasting disturbance electric fields be accounted for?, *J. Atmos. Sol. Terr. Phys.*, *69*, 1182–1199.

Matson, P. A., et al. (2010), *Advancing the Science of Climate Change*, National Academies Press, Washington, DC.

McDonald, A. J., R. E. Hibbins, and M. J. Jarvis (2011), Properties of the quasi 16 day wave derived from EOS MLS observations, *J. Geophys. Res.*, *116*, D06112, doi:10.1029/2010JD014719.

Melikechi, N., S. Gangopadhyay, and E. E. Eyler (1994), Phase dynamics in nanosecond pulsed dye laser amplification, *J. Opt. Soc. Am. B*, *11*(12), 2402–2411.

Mertens, C. J., et al. (2004), SABER observations of mesospheric temperatures and comparisons with falling sphere measurements taken during the 2002 summer MaCWAVE campaign, *Geophys. Res. Lett.*, *31*, L03105, doi:10.1029/2003GL018605.

Millward, G. H. (1993), A global model of the Earth's thermosphere, ionosphere and plasmasphere: Theoretical studies of the response to enhanced high-latitude convection, Ph.D. thesis, Univ. of Sheffield, England.

Millward, G. H., R. J. Moffett, S. Quegan, and T. J. Fuller-Rowell (1996), A coupled thermosphere ionosphere plasmasphere Model (CTIP), in *STEP Handbook on Ionospheric Models*, edited by R. W. Schunk, pp. 239–279, Utah State Univ., Logan.

Millward, G. H., I. C. F. Müller-Wodarg, A. D. Aylward, T. J. Fuller-Rowell, A. D. Richmond, and R. J. Moffett (2001), An investigation into the influence of tidal forcing on F region equatorial vertical ion drift using a global ionosphere-thermosphere model with coupled electrodynamics, *J. Geophys. Res.*, *106*(A11), 24733–24744, doi:10.1029/2000JA000342.

Mlynczak, M. G., and S. Solomon (1993), A detailed evaluation of the heating efficiency in the middle atmosphere, *J. Geophys. Res.*, *98*, 10,517−10,541.

Müller-Wodarg, I. C. F., A. D. Aylward, and T. J. Fuller-Rowell (2001), Tidal oscillations in the thermosphere: A theoretical investigation of their sources, *J. Atmos. Sol.-Terr. Phys.*, *63*, 899–914.

Murata, H. (1972), Atmospheric tidal oscillations in a viscid atmosphere, *J. Geomag. Geoelec.*, *25*, 387.

Murphy, D. J., M. Tsutsumi, D. M. Riggin, G. O. L. Jones, R. A. Vincent, M. E. Hagan, and S. K. Avery (2003), Observations of a nonmigrating component of the semidiurnal tide over Antarctica, *J. Geophys. Res.*, *108*, 4241, doi:10.1029/2002JD003077, D8.

Murphy, D. J., et al. (2006), A climatology of tides in the Antarctic mesosphere and lower thermosphere, *J. Geophys. Res.*, *111*, D23104, doi:10.1029/2005JD006803.

Murphy, D. J., T. Aso, D. C. Fritts, R. E. Hibbins, A. J. McDonald, D. M. Riggin, M. Tsutsumi, and R. A. Vincent (2009), Source regions for Antarctic MLT non-migrating semidiurnal tides, *Geophys. Res. Lett.*, *36*, L09805, doi:10.1029/2008GL037064.

National Decadal Survey: National Research Council (2013). *Solar and Space Physics: A Science for a Technological Society*. Washington, DC: The National Academies Press.

Negrea, C., M. V. Codrescu, and T. J. Fuller-Rowell (2012), On the validation effort of the Coupled Thermosphere Ionosphere Plasmasphere Electrodynamics model, *Space Weather*, *10*, S08010, doi:10.1029/2012SW000818.

Nielsen, K., M. J. Taylor, P. D. Pautet, D. C. Fritts, N. Mitchell, C. Beldon, W. Singer, F. J. Schmidlin, and R. A. Goldberg (2006), Propagation of short-period gravity waves at high-latitudes during the MaCWAVE winter campaign, *Ann. Geophys.*, *24*, 1–17.

Nielsen, K., M. J. Taylor, R. E. Hibbins, M. J. Jarvis, and J. M. Russell (2012), On the nature of short-period mesospheric gravity wave propagation over Halley, Antarctica, *J. Geophys. Res.*, *117*(D5), D05124, doi:10.1029/2011JD016261.

Oberheide, J., Q. Wu, T. L. Killeen, M. E. Hagan, and R. G. Roble (2006), Diurnal nonmigrating tides from TIMED Doppler Interferometer wind data: Monthly climatologies and seasonal variations, *J. Geophys. Res.*, *111*, A10S03, doi:10.1029/2005JA011491.

Pan, W., C. S. Gardner, and R. G. Roble (2002), The temperature structure of the winter atmosphere at South Pole, *Geophys. Res. Lett.*, *29*(16), 1802, doi:10.1029/2002GL015288.

Pan, W., and C. S. Gardner (2003), Seasonal variations of the atmospheric temperature structure at South Pole, *J. Geophys. Res.*, *108*(D18), 4564, doi:10.1029/2002JD003217.

Picone, J. M., A. E. Hedin, D. P. Drob, and A. C. Aikin (2002), NRLMSISE-00 empirical model of the atmosphere: Statistical comparisons and scientific issues, *J. Geophys. Res.*, *107*(A12), 1468, doi:10.1029/2002JA009430.

Plane, J. M. C. (2003), Atmospheric chemistry of meteoric metals, *Chem. Rev.*, *103*(12), 4963–4984, doi:10.1021/cr0205309.

Plane, J. M. C., W. Feng, and E. C. Dawkins (2015), The mesosphere and metals: chemistry and changes, *Chem. Rev.*, doi:10.1021/cr500501m.

Portnyagin, Y., Forbes, J., Merzlyakov, E., Makarov, N., Palo, S., (1998), The summertime 12-h wind oscillation with zonal wave number s = 1 in the lower thermosphere over the South Pole, *Ann. Geophys.*, *16*, 828–837.

Qian, J., and C. S. Gardner (1995), Simultaneous lidar measurements of mesospheric Ca, Na, and temperature profiles at Urbana, Illinois, *J. Geophys. Res.*, *100*(D4), 7453–7461.

Quegan, S., G. J. Bailey, R. J. Moffett, R. A. Heelis, T. J. Fuller-Rowell, D. Rees, and R. W. Spiro (1982), A theoretical study of the distribution of ionization in the high-latitude ionosphere and the plasmasphere: First results on the mid-latitude trough and the light-ion trough, *J. Atmos. Terr. Phys.*, *44*, 619-640, doi:10.1016/0021-9169(82)90073-3.

Randel, W. J. (1988), The seasonal evolution of planetary waves in the southern hemisphere stratosphere and troposphere, Q. J. R. Meteorol. Soc., 114,1385−1409, doi:10.1002/qj.49711448403.

Randel, W. J., et al. (2009), An update of observed stratospheric temperature trends, *J. Geophys. Res.*, *114*, D02107,doi:10.1029/2008JD010421.

Rees, D., T. J. Fuller-Rowell, and R. W. Smith (1980), Measurements of high latitude thermospheric winds by rocket and ground-based techniques and their interpretation using a three-dimensional, time-dependent dynamical model, *Planet. Space Sci.*, *28*(9), 919–932, doi:10.1016/0032-0633(80)90064-1.

Richmond, A.D., and R. G. Roble (1987), Electrodynamic effects of thermospheric winds from the NCAR thermospheric general circulation model, *J. Geophys. Res.*, *92*, 12365.

Richmond, A. D. (1995), Ionospheric electrodynamics, in *Handbook of Atmospheric Electrodynamics*, vol . II, edited by H. Volland, pp. 249–290, CRC Press, Boca Raton, Fla.

Rishbeth, H. and O.K. Garriott (1969), Introduction to Ionospheric Physics, Academic Press, New York.

Roble, R.G., R.E. Dickinson, and E.C. Ridley (1982), Global circulation and temperature structure of thermosphere with high-latitude plasma convection, *J. Geophys. Res.*, 1599-1614.

Russell, J. M., M. G. Mlynczak, L. L. Gordley, J. J. Tansock, and R. W. Esplin (1999), Overview of the SABER experiment and preliminary calibration results, *Proc. SPIE Int. Soc. Opt. Eng.*, 3756, 277–288, doi:10.1117/12.366382.

Schoeberl, M. R., and D. L. Hartmann (1991), The dynamics of the stratospheric polar vortex and its relation to springtime ozone depletions, *Science*, *251*, 46– 52.

Schwartz, M. J., et al. (2008), Validation of the Aura Microwave Limb Sounder temperature and geopotential height measurements, *J. Geophys. Res.*, *113*, D15S11, doi:10.1029/2007JD008783.

Siskind, D. E., C. A. Barth, and R. G. Roble (1989), The response of thermospheric nitric oxide to an auroral storm: 1. Low and middle latitudes, *J. Geophys. Res.*, *94*(A12), 16885–16898, doi:10.1029/JA094iA12p16885.

Solomon, S., P. J. Crutzen, and R. G. Roble (1982), Photochemical coupling between the thermosphere and the lower atmosphere: 1. Odd nitrogen from 50 to 120 km, *J. Geophys. Res.*, *87*(C9), 7206–7220, doi:10.1029/JC087iC09p07206.

Smith, A. K., D. R. Marsh, and A. C. Szymczak (2003), Interaction of chemical heating and the diurnal tide in the mesosphere, *J. Geophys. Res.*, *108*(D5), 4164, doi:10.1029/2002JD002664.

Smith, A. K., Physics and chemistry of the mesopause region (2004), *J. Atmos. Sol.-Terr. Phys.*, *66*, 839−857.

Smith, A. K., D. V. Pancheva, N. J. Mitchell, D. R. Marsh, J. M. Russell III, and M. G. Mlynczak (2007), A link between variability of the semidiurnal tide and planetary waves in the opposite hemisphere, *Geophys. Res. Lett.*, *34*, L07809, doi:10.1029/2006GL028929.

Smith, J. A., X. Chu, W. Huang, J. Wiig, and A. T. Brown (2008), LabVIEW-based laser frequency stabilization system with phase sensitive detection servo loop for Doppler lidar application, *Opt. Eng.*, *47*(11), 114201.

Smith, J., X. Chu, W. Huang, and B. Tan (2009), Applications of spectral analysis and filter design in laser frequency locking system for Na Doppler lidars, *Opt. Eng.*, *48*(10), 104301.

Smith, J. A., W. Fong, B. Roberts, W. Huang, and X. Chu (2012), Very high-resolution Na Doppler LIDAR at Boulder, Colorado, *Proceeding of the 26th International Laser Radar Conference*, pp. 151–154, Porto Heli, Greece, 25–29 June 2012.

Smith, J. A., and X. Chu (2015), High-efficiency receiver architecture for resonance-fluorescence and Doppler lidars, *Appl. Opt.*, *54*, 3173–3184, doi: 10.1364/AO.54.003173.

Süli, E., and D. Mayers (2003), *An Introduction to Numerical Analysis*, Cambridge University Press, UK.

Taylor, K. E., R. J. Stouffer, and G. A. Meehl (2012), An overview of Cmip5 and the experiment design, *B. Am. Meteorol. Soc.*, *93*(4), 485–498.

Taylor, R. John (1997), *An Introduction to Error Analysis*, 2nd ed., University Science Books, Sausalito, Calif.

Thomas, G. E. (1991), Mesospheric clouds and the physics of the mesopause region, *Rev. Geophys.*, *29*, 553–575.

Thomas, G. E. (1996a), Is the polar mesosphere the miner's canary of global change? *Adv. Space Res.*, *18*, 149–158.

Thomas, G. E. (1996b), Global change in the mesosphere-lower thermosphere region: Has it already arrived? *J. Atmos. Sol. Terr. Phys.*, *58*, 1629–1656.

Thompson, D. W. J., S. Solomon, P. J. Kushner, M. H. England, K. M. Grise, and D. J. Karoly (2011), Signatures of the Antarctic ozone hole in Southern Hemisphere surface climate change, *Nat. Geosci.*, *4*(11), 741–749.

Turner, J. et al. (2014), Antarctic climate change and the environment: an update, *Polar Record*, *50*, 237–259, doi:10.1017/S0032247413000296.

Vial, F., and J. M. Forbes (1989), Recent progress in tidal modeling, *J. Atmos. Terr. Phys.*, 51, 663–671.

Walterscheid, R. L. (1981), Inertio-gravity wave induced accelerations of mean flow having an imposed periodic component: implications for tidal oscillations in the meteor region, *J. Geophys. Res.*, *86*, 9698.

Wang, H., T. J. Fuller-Rowell, R. A. Akmaev, M. Hu, D. T. Kleist, and M. D. Iredell (2011), First simulations with a whole atmosphere data assimilation and forecast system: The January 2009 major sudden stratospheric warming, *J. Geophys. Res.*, *116*, A12321, doi:10.1029/2011JA017081.

Wang, Z., X. Chu, W. Huang, W. Fong, J. A. Smith, and B. Roberts (2012), Refurbishment and upgrade of Fe Boltzmann/Rayleigh temperature lidar at Boulder for a McMurdo lidar campaign in Antarctica, *Proceedings of the 26th International Laser Radar Conference*, pp. 207-210, Porto Heli, Greece, 25–29 June 2012.

Waters, J. W., et al. (2006), The Earth Observing System Microwave Limb Sounder (EOS MLS) on the Aura satellite, *IEEE Trans. Geosci. Remote Sens.*, *44*, 1075–1092.

Weimer, D. R. (1995), Models of high-latitude electric potentials derived with a least error Dt of spherical harmonic coefficients, *J. Geophys. Res.*, *100*, 19,595–19,607, doi:10.1029/95JA01755.

Weimer, D. R. (2005), Improved ionospheric electrodynamic models and application to calculating Joule heating rates, *J. Geophys. Res.*, *110*, A05306, doi:10.1029/2004JA010884.

World Meteorological Organization (1957), Meteorology—A three-dimensional science: Second session of the commission for aerology, *WMO Bull.*, *6*, 134–138.

Yamashita, K., S. Miyahara, Y. Miyoshi, K. Kawano, and J. Ninomiya (2002), Seasonal variation of non-migrating semidiurnal tide in the polar MLT region in a general circulation model, *J. Atmos. Sol. Terr. Phys.*, *64*, 1083–1094.

Yu, Z., and X. Chu, Thermospheric Fe layer modeling at McMurdo, Antarctica, in preparation for J. Geophys. Res., 2015.

Zängl, G., and K. P. Hoinka (2001), The tropopause in the polar regions, *J. Clim.*, *14*, 3117–3139.

Zhang, X., J. M. Forbes, and M. E. Hagan (2010a), Longitudinal variation of tides in the MLT region: 1. Tides driven by tropospheric net radiative heating, *J. Geophys. Res.*, *115*, A06316, doi:10.1029/2009JA014897.

Zhang, X., J. M. Forbes, and M. E. Hagan (2010b), Longitudinal variation of tides in the MLT region: 2. Relative effects of solar radiative and latent heating, *J. Geophys. Res.*, *115*, A06317, doi:10.1029/2009JA014898.

Zhu, X., Talaat, E. R., Baker, J. B. H., and Yee, J.-H. (2005), A self-consistent derivation of ion drag and Joule heating for atmospheric dynamics in the thermosphere, *Ann. Geophys.*, *23*, 3313-3322, doi:10.5194/angeo-23-3313-2005.